

Micromechanisms governing plastic instability in Al–Li based alloys

Vom Promotionsausschuss der
Technischen Universität Hamburg–Harburg
zur Erlangung des akademischen Grades
Doktor–Ingenieur (Dr.–Ing)
genehmigte Dissertation

von

Henry Ovri

aus

Olomoro, Nigeria

2015

Gutachtern der Dissertation:

Prof. Dr. Erica Lilleodden

*Department Head, Experimental Materials Mechanics
Institute of Materials Research, Materials Mechanics
Helmholtz Zentrum Geesthacht
21502 Geesthacht, Germany.*

Prof. Bill Curtin

*Head, Institute of Mechanical Engineering
Ecole Polytechnique Fédérale de Lausanne, EPFL
Lausanne, Switzerland.*

Vorsitzender des Prüfungsausschusses:

Prof. Dr.-Ing. Stefan Heinrich

*Head, Institute of Solids Process Engineering and Particle Technology
Technical University of Hamburg–Harburg
21073 Hamburg, Germany.*

Tag der mündlichen Prüfung:

11th November 2015

Micromechanisms governing plastic instability in Al–Li based alloys

Vom Promotionsausschuss der
Technischen Universität Hamburg–Harburg
zur Erlangung des akademischen Grades
Doktor–Ingenieur (Dr.–Ing)
genehmigte Dissertation

von

Henry Ovri

aus

Olomoro, Nigeria

2015

Acknowledgement

Firstly, I want to sincerely thank my PhD advisor, Prof. Dr. Erica Lilleodden, for the immense support, encouragement, guidance and training she offered me during the course of this work. I could not have wished for a better advisor. Her commitment to the success of this work was never in doubt and this is deeply appreciated. I am also indebted to her for the opportunity she gave me to carry out part of this work in the National Centre for Electron Microscopy, NCEM, in Berkeley, USA. I also want to thank Prof. Bill Curtin, Head, Institute of Mechanical Engineering, Ecole Polytechnique Fédérale de Lausanne, EPFL, Lausanne, Switzerland for very insightful discussions and Prof. Dr.-Ing Norbert Huber, Head of the Institute of Materials Research, for his fatherly role and support during the course of this work.

My sincere thanks also to Dr. Eric Jäggle of the Dept. of Microstructure Physics and Alloy design, Max Planck Institut für Eisenforschung GmbH, Düsseldorf, for helping out with the atom probe experiments and Dr. Andreas Stark of the Institute of Materials Physics, HZG, for his contribution in high energy x-ray diffraction experiments. Prof. Andy Minor, Dr. Josh Kasher and Dr. Qian Yu are acknowledged for their support during my stay at NCEM.

I would like to thank staff members of WME for their warmth and encouragement. It has been such a great pleasure working in such a friendly environment.

Special thanks also to my dear wife, Mercy and our two little angels, Annie and Domero and other members of my family for their love, encouragement and prayers.

Lastly but most importantly, I express my profound thanks to the fountain of my strength and source of my hope, God Almighty. I am who I am by HIS grace.

Abstract

The investigation of the underlying microscopic mechanisms that govern plastic instability in solution strengthened and precipitation strengthened Al alloys has been the subject of several studies. These studies are largely motivated by the need to devise strategies to mitigate the undesirable effects, such as reduction in ductility and formation of surface striations, which occur in alloys that exhibit this phenomenon. While the microscopic origin of plastic instability in solution strengthened alloys Al alloys is fairly well established, there is yet no convincing model that is consistent with experimental observations and gives a clear mechanistic description of the origin of the phenomenon in precipitation strengthened Al alloys.

In this work, detailed experimental investigations of several tempers of a multi-component Al–Li based alloy, AA2198, have been carried out. Both mechanical and microstructural characterization techniques were employed in order to correlate microstructural characteristics to global and local mechanical behaviour. Specifically, high resolution nanoindentation and micro–tensile testing were used for mechanical testing, while transmission electron microscopy based methods – including *in situ* TEM tensile straining, along with high energy x–ray diffraction and atom probe tomography were used to investigate the relevant microstructural characteristics.

The experimental results clearly showed that dynamic strain aging of temporarily trapped mobile dislocations by Li atoms, widely accepted as the underlying mechanism for plastic instability in Al–Li based alloys, cannot sufficiently account for the occurrence of plastic instability in AA2198. Moreover, theoretical analyses of strengthening mechanisms in the investigated tempers showed that only the overaged temper, which is also the only temper that displayed plastic instability, is governed by order hardening.

In light of the wealth of experimental results, a mechanistic model describing the microscopic mechanisms underlying plastic instability in precipitation strengthened Al–Li based alloy systems was developed. It is proposed that the phenomenon is governed by an altogether different mechanism than what has so far been considered, namely a diffusion–controlled pseudo–locking mechanism that accompanies order hardening at low strain rates. The applicability of the model to other Al–Li alloy based systems was also examined. It was demonstrated, by critical examination of the instability behaviour of a number of binary and multi–component Al–Li based alloy systems reported in literature, that plastic instability only occurs in these alloy systems when strength is governed by order hardening.

Zusammenfassung

Die Erforschung der zugrundeliegenden mikroskopischen Mechanismen, die plastische Instabilität in mischkristall- und ausscheidungsverfestigten Aluminium-Legierungen bestimmen, ist Gegenstand verschiedener Untersuchungen gewesen. Diese Studien sind weitgehend motiviert durch die Notwendigkeit, Strategien zur Abschwächung unerwünschter Effekte wie Duktilitätsminderung und Ausbildung von Oberflächenriefen, welche in eben solchen Legierungen auftreten, zu entwerfen. Während der mikroskopische Ursprung von plastischer Instabilität in mischkristallverfestigten Al-Legierungen ziemlich gut bekannt ist, gibt es immer noch kein überzeugendes Modell welches eine klare mechanistische Beschreibung im Einklang mit experimentellen Beobachtungen für plastische Instabilität in ausscheidungsverfestigten Al-Legierungen anbietet.

In der vorliegenden Arbeit wurden detaillierte experimentelle Untersuchungen unterschiedlicher Härtestufen der Mehrkomponenten-Aluminium-Lithium (Al-Li) Legierung AA2198 durchgeführt. Sowohl mechanische als auch mikrostrukturelle Charakterisierungstechniken wurden verwendet, um mikrostrukturelle Eigenschaften globalem und lokalem mechanischem Verhalten zuzuordnen. Insbesondere wurden hochauflösende Nanoindentations- und Mikrozugverfahren zur mechanischen Untersuchung verwendet; die relevanten mikrostrukturellen Eigenschaften dagegen wurden mit Methoden basierend auf Transmissionselektronenmikroskopie (TEM) untersucht, einschließlich in-situ TEM Zugbelastung zusammen mit Hochenergie-Röntgenbeugung und Atomsonden-Tomographie.

Die experimentellen Ergebnisse zeigten eindeutig, dass das Auftreten von plastischer Instabilität in AA2198 nicht ausreichend erklärt werden kann durch dynamische Reckalterung von temporär durch Li Atome blockierte mobile Versetzungen, welches der weitgehend akzeptierte zugrundeliegende Mechanismus in Al-Li basierten Legierungen ist. Darüber hinaus zeigten theoretische Analysen von Verfestigungsmechanismen in den untersuchten Wärmebehandlungszuständen, dass die Verformung nur im überalterten Zustand durch Ordnungshärtung bestimmt ist – auch plastische Instabilität tritt lediglich in diesem Wärmebehandlungszustand auf.

Mit Hilfe der Fülle der experimentell erzielten Resultate wurde ein mechanistisches Modell entwickelt, welches die der plastischen Instabilität zugrundeliegenden mikroskopischen Mechanismen in ausscheidungsverfestigten Al-Li basierten Legierungen beschreibt. In diesem wird beschrieben wie, entgegen bisheriger Annahmen, plastischen Instabilität durch einen diffusionskontrollierten Pseudo-Sperrmechanismus bestimmt wird, welcher die Ordnungshärtung bei niedrigen Verformungsraten begleitet. Die Anwendbarkeit des Modells auf andere Al-Li basierte Legierungssysteme wurde untersucht. Durch kritische Untersuchung des Instabilitätsverhaltens einer Anzahl von in der Literatur beschriebenen binären und mehrkomponentigen Al-Li basierten Legierungen wurde demonstriert, dass

plastische Instabilität nur dann in diesen Systemen auftritt wenn die Festigkeit durch Ordnungshärtung bestimmt wird.

Table of Contents

Acknowledgement	v
Abstract	vi
1 Introduction	xii
1.1 Motivation	1
1.2 Approach	3
2 Fundamentals of strengthening mechanisms and plastic instability	4
2.1 Strengthening mechanisms	4
2.1.1 Solution strengthening	5
2.1.2 Grain boundary strengthening	7
2.1.3 Strain hardening	8
2.1.4 Precipitation strengthening	9
2.2 Plastic instability	14
2.2.1 Basic principles	14
2.2.2 Plastic instability in solution strengthened Al–Mg based alloys: current understanding	16
2.2.3 Plastic instability in precipitation strengthened Al–Li based alloys: current understanding	20
3 Experimental material and methods	23
3.1 Microstructure and precipitation in Al–Cu–Li–Mg–Zr based alloys	23
3.2 Thermal processing	24
3.3 Microtensile testing	25
3.4 Nanoindentation	26
3.5 Electron microscopy	29
3.5.1 Scanning Electron microscope and Focused Ion Beam Milling	29
3.5.2 Transmission electron microscopy	31
3.5.3 <i>In situ</i> TEM straining	35
3.6 High resolution x–ray diffraction	35
3.7 Atom probe tomography	36
4 Mechanical and microstructural characterization	41
4.1 Mechanical response	41
4.1.1 Microtensile tensile	41

4.1.2	Nanoindentation testing	44
4.2	Microstructural constituents.....	50
4.2.1	Peak aged (PA) temper.....	51
4.2.2	Naturally aged (NA) temper	51
4.2.3	Overaged temper	52
4.3	High energy x-ray diffraction (HEXRD).....	57
4.4	<i>In situ</i> tensile straining in the TEM.....	60
4.5	Atom probe tomography of the PA, NA and OA tempers.....	64
5	Microstructural influences on strengthening mechanisms in AA2198	71
5.1	Strengthening mechanisms in the peak aged temper	71
5.2	Strengthening mechanisms in the naturally aged temper.....	72
5.3	Strengthening mechanisms in the overaged temper	74
6	Mechanism of plastic instability in Al–Li based alloys	77
6.1	Dynamic strain aging	77
6.2	Precipitate shearing	79
6.3	Pseudo-locking: a new mechanism for plastic instability	80
6.4	Application of the proposed model to Al–Li based alloy systems	86
7	Concluding remarks	89
	Appendix	92
	References	93
	Curriculum vitae	102

Table of Figures

Fig. 2.1: Schematic illustration of the shape of the stress vs. strain curves corresponding to the three different types of spatio-temporal arrangements of deformation bands associated with plastic instability.....	16
Fig. 3.1: Schematic of the microtensile sample showing markers placed 1 mm apart. The basic working principle of the laser scanner is also illustrated.....	25
Fig. 3.2: Schematic illustration of an elasto-plastic material under the influence of a conical indenter.....	27
Fig. 3.3: Schematic illustration of the Nanoindenter XP (Taken from [88]).....	28
Fig. 3.4: Micrographs showing the main steps in TEM sample preparation with FIB. (a) Platinum (Pt) layer on sample surface. (b) Staircase-like trenches with lamella at the middle. (c) A lamella partially cut-free from the bulk sample. The region where the lamella is attached to the Omniprobe is also indicated. (d) Three fingers of a Cu grid, an Omniprobe containing a lamella and a section of the Pt deposition gun are shown in this micrograph. (e) A lamella being attached to one of the fingers of the Cu grid. (f) An electron transparent lamella attached to the Cu grid.....	33
Fig. 3.5: Micrographs showing the main steps in APT sample preparation with FIB. (a) Lamella with one edge already cut free. (b) A wedge being attached to the top of a micro-tip post. (c) A wedge sitting on top of a post. (d) A finished APT tip after low kV cleaning.....	34
Fig. 3.6: Schematic illustration of the diffraction patterns observed in a typical Al-Li-Cu-Mg-Ag alloy after artificial aging. (a) $\langle 112 \rangle_{\alpha}$ (b) $\langle 100 \rangle_{\alpha}$ zone axes respectively. ...	34
Fig. 3.7: Set up for the <i>in situ</i> TEM straining experiments. (a) The single tilt tensile holder. (b) Schematic of the shape and dimensions of the foil.....	36
Fig. 3.8: Schematic of the working principle of an atom probe. The different coloured spheres represent different atomic species.....	38
Fig. 4.1: True stress -true strain response of AA2198 for the various tempers considered: peak aged (PA) in purple, near-peak aged (N-PA) in green, naturally aged (NA) in blue, underaged (UA) in pink, and overaged (OA) in red. Plastic instabilities are only found in the overaged temper.....	42
Fig. 4.2: (a) The local (in pink) and global (in brown) strain responses of the OA temper plotted as a function of time. The corresponding stress response is also shown in the plot. (b) The local strain response of all the five investigated tempers plotted as a function of time. Colour codes are as previously defined.....	43
Fig. 4.3: Work hardening rates ($d\sigma_t/d\varepsilon_t$) of each temper plotted as a function of true plastic strain. Colour codes are as previously defined.....	45

Fig. 4.4: Load–displacement curves of PA, NA and OA tempers. Colour codes are as previously defined.	45
Fig. 4.5: A section of the load vs. displacement response from the strain rate jump tests. The associated imposed strain rate (black line) is included in the plot. The broken line is a guide for the eyes.	47
Fig. 4.6: Hardness vs. displacement response of the PA, NA and OA tempers. The imposed strain rate is also included in the plot. The broken lines as before are a guide for the eye. Colour codes are as previously defined.....	48
Fig. 4.7: Strain rate sensitivity, m , as a function of the change in strain rate.	49
Fig. 4.8: Size distribution of δ' phase in the overaged (OA) and naturally aged (NA) tempers.....	50
Fig. 4.9: Selected area diffraction patterns (SADP) of the PA temper taken along (a) $\langle 100 \rangle_{\alpha}$ zone axis and (b) $\langle 112 \rangle_{\alpha}$ zone axis. Schematics of these SADPs and the phases represented by the spots and streaks are shown in Fig. 3.6. A dark field image showing one variant of T_1 phase and δ'/β' is shown in (c). The micrograph in (d) is a two beam bright field image (2BBF) image showing two variants of the T_1 phase...	54
Fig. 4.10: TEM micrographs from the naturally aged (NA) temper. (a) $\langle 100 \rangle_{\alpha}$ zone axis SADP showing superlattice spots from δ'/β' precipitates. (b) A dark field (DF) image showing the δ'/β' composite phase. The donut morphology of these precipitates is indicative of the precipitation of δ' on the β' phase. (c) Another dark field image of the δ'/β' phase made from a superlattice spot but with the matrix diffraction spots tilted to a two beam condition. (d) Typical dislocation structure in this temper.....	55
Fig. 4.11: TEM micrographs from the overaged (OA) temper. (a) $\langle 112 \rangle_{\alpha}$ zone axis SAD pattern, showing no evidence of S' , T_1 or Ω phases. Spots arising from δ'/β' and T_B phase are present. (b) A bright field image clearly shows the T_B and T_2 precipitates, as indicated by the arrows.(c) A dark field image shows δ'/β' precipitates. (d) A typical dislocation structure in this temper.	56
Fig. 4.12: HEXRD spectra for the three tempers. (a) The full spectra, including the 2θ positions of the experimental and simulated phases. (b) An enlarged section of the spectra showing some of the weak peaks. A 2θ position of δ' phase that did not coincide with the Al peak positions is shown by an arrow in the figure (c) Two prominent experimental Al peaks showing slight shift of the Al peak associated with the NA.....	59
Fig. 4.13: Series of still images taken from video frames recorded during <i>in situ</i> TEM tensile straining of the overaged sample. The black arrows show dislocations that glide concurrently. The red arrow shows the glide direction of the trailing dislocation in pair 1.	62

- Fig. 4.14: TEM micrographs of the OA temper showing, (a) a BF image of the equilibrium precipitates in an undeformed sample (b) BF image of equilibrium precipitates after *in situ* TEM straining of a lamella. (c) Corresponding DF image of (b). The pre- and post-deformation images were not taken from the same sample. 63
- Fig. 4.15: TEM micrograph taken with the straining holder after the *in situ* TEM tensile straining test of (a) The overaged temper (OA). Slip is mostly planar after deformation, as was the case in the pre-deformed sample. (b) The Naturally aged temper (NA). 63
- Fig. 4.16: Three dimensional atom probe tomography maps of Li (pink), Cu (orange), and Mg (blue) atoms in the (a) peak aged (PA), (b) naturally aged (NA) and (c) overaged (OA) tempers. With the exception of a Cu-rich phase at the tip of the NA temper, no precipitate was visible in all the measurements. More so, all the atoms in the NA and OA tempers appear to be homogeneously distributed, with no indication of clustering. 67
- Fig. 4.17: A proxigram created using the interface of the Cu-rich precipitate at the top of the NA specimen. Concentration profiles of the Al (in teal), Cu (in orange) and Li (in pink) atoms are shown. 68
- Fig. 4.18: Frequency histograms of 5th nearest neighbour distances (5NN) between atoms of the naturally aged, NA, (straight lines) and overaged, OA, (broken lines) temper. The distribution of the main atomic species, Li-Li (pink), Cu-Cu (orange), Mg-Mg (blue), Cu-Mg (green) and their respective randomised distribution (black) are presented. 69
- Fig. 4.19: The experimental size distribution of the (a) Cu-Cu clusters in the naturally aged temper, NA, (orange line), and the overaged temper, OA, (broken orange line). (b) Li-Li clusters in the NA temper (pink line). The respective randomized distribution for the NA temper (black line) and the OA temper (broken black line) is also included in the plot. 70
- Fig. 5.1: High angle annular dark field – scanning transmission electron microscope (HAADF-STEM) image of a sheared T₁ phase in a 2% plastically deformed AA2198 sample. (Taken from [115]) 72
- Fig. 6.1: Critical configuration of a dislocation pair cutting through a group of ordered coherent δ' precipitates. The shaded spheres represent precipitates with perfect APBs while the open spheres represent ordered precipitates. Spheres with both open and shaded areas represent precipitates with partial APBs. d_i is the average length of the dislocation, D_i lying in a precipitate, l_i is the mean distance between the precipitates sampled by D_i and A is the average distance between D_1 and D_2 82
- Fig. 6.2: Simplified illustration of (a) an edge-on view of the mechanism proposed here-in. At high strain rates the passage of the of leading dislocation, D_1 , through the δ' phase leaves an anti-phase boundary (APB) in its wake (i.e., ii), while the passage of

the trailing dislocation, D_2 , recovers the perfect ordering of the precipitate (i.e., iii). At slow strain rates, a diffusion-controlled re-ordering of the APB between steps (ii) and (iii) leads to a higher critical stress for the second dislocation to pass through the precipitate. (b) an in-plane view of the slip plane through the δ' phase, showing the perfectly ordered state (i), the full APB (ii), the (relaxed) APB after a time, t , prior to the passage of D_2 (iii), the partially re-ordered slip plane formed after the passage of D_2 (iv) and the perfectly re-ordered slip plane..... 85

1 Introduction

1.1 Motivation

A number of technologically important alloys including steels, magnesium (Mg)-, copper (Cu)- and aluminium (Al)- based alloys are known to exhibit repetitive yielding during plastic deformation at critically low strain rates and over a range of temperatures. This repetitive yielding, which is more commonly referred to as serrated flow, appears as stress drops in the plastic region of stress-strain curves. This phenomenon, which is also known as plastic instability or Portevin-Le-Chaterlier (PLC) effect, has attracted continuous interest among experimentalists and modelling experts [1-9]; the primary motivation being the need to unravel the underlying microscopic mechanisms that govern the phenomenon. Such understanding is critical to the design of alloys and process routes that mitigate undesirable effects such as reduction in ductility and formation of surface striations associated with the phenomenon [1,9]. This has implications for metal sheet forming applications, particularly in the automotive and aerospace industries where Mg- and Al-based alloys, driven by their excellent strength-to-weight ratios, are becoming increasingly important.

A number of models, both phenomenological and theoretical, have been proposed to explain the origin of plastic instability in solution strengthened Al-based alloys [10-16]. Most of these models associate PLC-type plastic instability with dynamic strain aging (DSA), which refers to the solute aging of mobile dislocations that have been temporarily trapped at localized obstacles such as forest dislocations during deformation. It has been proposed that the increase in strength arising from the DSA process leads to negative strain rate sensitivity (nSRS), which is an anomalous behaviour that manifest macroscopically as serrations (stress drops) in stress-strain curves [17] . However, recent modelling

efforts have shown that DSA cannot independently lead to nSRS [18–20]. In view of this, Soare and Curtin [20] proposed a rate-dependent constitutive model for DSA in solution strengthened Al–Mg alloys that is not only predictive but appears to capture the physical mechanism associated with DSA. They showed in their model that solute aging of mobile and forest dislocations through cross-core diffusion must take place concurrently for nSRS to manifest.

These recent theoretical models [18–20] question the view accepted by several workers that it is DSA by Li atoms that leads to the nSRS that exclusively governs plastic instability in precipitation strengthened Al–Li based alloys [21–25]. Some other workers attribute the presence of instabilities in these alloys to the shearing of δ' (Al_3Li) precipitates [26–29]. The second view is largely predicated on the fact that these precipitates are shearable and are often present in Al–Li based alloys that exhibit plastic instabilities. However, there has been so far no model based on precipitate shearing, as far as we know, that gives a clear mechanistic description of the origin of plastic instability and additionally accounts for the nSRS that accompanies the instability in these alloy systems.

Understanding the underlying microscopic mechanism(s) that govern plastic instability in these alloys requires detailed experimental investigations of the relationships between plastic instability and local microstructural constituents, including dislocations, solute atoms and precipitates. Such an approach has been largely ignored in the studies of plastic instability. As such, most of the available models, both phenomenological and theoretical, are based on descriptions of mesoscopic observations and global responses observed in stress–strain curves. In general, the present work aims to bridge the perceived gap in understanding between the microscopic origins and macroscopic manifestations of plastic instability by employing state-of-the-art characterization techniques such as nanoindentation, microtensile testing, transmission electron microscopy (TEM), *in situ* tensile straining in the TEM, atom probe tomography (APT) and high energy x-ray diffraction (HEXRD). More specifically, the goal is to examine the influence of precipitates in mitigating or enhancing plastic instability and to identify the microscopic mechanism(s) that govern the phenomenon in an Al–Li based alloy, AA2198. It is hoped that such understanding will form the basis for the development of mechanistically accurate theoretical models with excellent predictive capabilities for plastic instability in Al–Li based alloys.

1.2 Approach

The first step in this work involved the heat treatment of the test alloy to produce a variety of samples with varying solute content and precipitates; five different tempering treatments were carried out.

Mechanical characterization of the different tempers was accomplished with nanoindentation and microtensile testing. The high resolution load and displacement capabilities of the nanoindentation test in particular make it useful for the study of the local microscopic responses that are encountered in plastic instability.

Next, detailed microstructural characterization of three representative tempers was carried out using transmission electron microscopy (TEM) methods, high energy x-ray diffraction (HEXRD) and atom probe tomography (APT). The main focus of the microstructural characterization was to establish the influence of the local microstructural content especially Li matrix content, δ' phase and dislocations on the occurrence of plastic instability. *In situ* TEM tensile straining experiments were also carried out in order to gain better insight into the dislocation–precipitation interactions.

Finally, a critical analysis of the results obtained from the various experiments was accomplished. The analysis formed the basis for establishing the influence of precipitation on plastic instability in addition to the development of a mechanistic model that accurately describes the microscopic origin of plastic instability in Al–Li based alloys.

2 Fundamentals of strengthening mechanisms and plastic instability

Since metallic materials primarily deform by dislocation glide, the introduction of obstacles that impede the glide of the dislocations leads to an increase in the strength of the materials. The energy required by the dislocations to overcome the barriers posed by obstacles lying in their glide paths determines the strength of the material and consequently its susceptibility to plastic instability. Typical obstacles that are effective in impeding dislocation motion are solute atoms, grain boundaries, other dislocations and precipitates. Although more than one of these obstacles is usually present in technological alloys, it is usually the case that most of the strengthening is largely governed by only one of the obstacles. A review of the microscopic mechanisms that govern strengthening in the presence of these obstacles is given in sections 2.1. In section 2.2, the phenomenon of plastic instability is discussed. The emphasis is on the micromechanisms leading to plastic instability in solution strengthened aluminium–magnesium (Al–Mg) alloys, which are the most susceptible Al alloys to plastic instability, and precipitation strengthened aluminium–lithium (Al–Li) based alloys, which are the main focus of this study.

2.1 Strengthening mechanisms

In general, metallic materials are strengthened by four main mechanisms. These include solution strengthening, grain size strengthening, strain hardening and precipitation hardening. A brief description of the main features of each of these mechanisms and the theoretical models proposed to estimate the shear stress derived from them is presented in this section.

2.1.1 Solution strengthening

Solute atoms dissolved in the matrix of a metal increase the yield strength of the metal. Solute atoms form either substitutional or interstitial solid solutions. The former occurs when the size difference between the solute and matrix atoms is less than 15%. In this case, the solute atoms occupy lattice sites normally occupied by matrix atoms. Interstitial solid solutions, on the other hand, are formed when the solute atoms are much smaller than the matrix atoms. Under such circumstances, the atoms occupy interstitial positions [30].

A number of mechanisms have been proposed to estimate the strengthening from the addition of solute atoms. These include: elastic-, modulus-, stacking fault-, electrostatic-, short range order- and long range order- interaction mechanisms [30,31]. The mechanisms that govern strengthening in substitutional solid solutions of aluminium are however mainly due to elastic and modulus interactions [32].

Elastic interaction arises from the mutual interaction between the local stress fields around a solute atom in a host matrix and the stress fields around mobile dislocations. The energy of the interaction will be negative and the dislocation will be attracted to the solute atom if the solute atom is smaller than the host atom and it lies above the dislocation core or if the solute atom is larger than the host atom and it lies below the dislocation core. In either case, an increase in flow stress results since additional energy is required to liberate the dislocation from the solute atom. Although it is expected that the solute atoms will produce as many attractive centres as repulsive centres, the overall interaction energy in the crystal is negative since the dislocations mostly lie in regions of negative interaction energy [33]. Strengthening is thus always achieved by the addition of solute atoms to a matrix. The critical resolved shear stress, CRSS, due to elastic interactions, $\Delta\tau^{\text{EI}}$, is given as [34]:

$$\Delta\tau^{\text{EI}} = 1.26G (0.1\varepsilon_a)^{4/3} c^{2/3}, \quad (2.1)$$

where G is the shear modulus of the alloy, c is the atomic concentration of the solute and ε_a is the size mismatch parameter. ε_a is proportional to the difference in the lattice parameter, a , of the matrix per unit concentration of the solute, c :

$$\varepsilon_a = \frac{3}{a} \left(\frac{da}{dc} \right). \quad (2.2)$$

Modulus interaction occurs when there is a difference between the shear modulus of the matrix and that of the solute atoms. The shear modulus of an individual solute atom is assumed to be the same as that of a volume, b^3 , of the solute atoms [31]. The dislocation–solute atom interaction arising from the difference in shear modulus is such that the energy of the strain field of the dislocation is reduced, i.e. it is negative, if the shear modulus of the solute atom is smaller than that of the matrix. The dislocation is attracted to the solute atom under this condition and an increase in shear stress results since additional energy will be required to liberate the dislocation from the solute atom [30]. The strengthening from the modulus interaction is estimated to be [34]:

$$\Delta\tau^{MI} = 1.26G \left[\frac{1}{32\pi^2} \varepsilon_G \left(1 + \frac{\varepsilon_G}{2} \right)^{-1} \right]^{4/3} c^{2/3}, \quad (2.3)$$

where the modulus misfit parameter, ε_G , accounts for the variation of shear modulus with alloying:

$$\varepsilon_G = \frac{1}{G} \left(\frac{dG}{dc} \right). \quad (2.4)$$

Although these models are widely accepted, it is often the case that estimates of solution strengthening $\Delta\tau^{SS}$, are made from simple expressions of the form [35][36]:

$$\Delta\tau^{SS} = \sum k_j \cdot c_j^n, \quad (2.5)$$

where k is a scaling factor for individual elements expressed as an increase in yield strength per wt.% of the added element, c is the concentration of the alloy element and n is a constant in the range of 0.5 – 0.75.

Solution strengthening results in only moderate increases in the strength of commercial alloys, due to the typically low solubility of solute atoms that can significantly increase strength in such alloys.

2.1.2 Grain boundary strengthening

It is well known that an effective way to increase the strength of a polycrystalline material is to reduce the average size of its grains. A convenient estimate of the strength derived from grain boundaries, σ_y^{GB} , is given by the Hall–Petch relationship, which expresses yield strength as an inverse function of the square root of the average grain size, d , [37]:

$$\sigma_y^{GB} = k_y d^{-1/2}, \quad (2.6)$$

where k_y is the stress intensity for plastic yielding across polycrystalline grain boundaries, usually between 0.3 – 0.6.

Two types of mechanisms, the dislocation pile up model and the grain boundary source model, are often invoked to explain the Hall–Petch relationship.

In the dislocation pile up model, the grain size dependence of yield strength is attributed to dislocation pile-ups at grain boundaries. The model assumes that if the stress concentration resulting from the pile-up of dislocations at a particular grain boundary is sufficiently large, the dislocations will activate a source in the neighbouring grain. Since the number of dislocations in a pile-up is proportional to the grain size, large grains will require lower applied stress to initiate plastic deformation in comparison to small grains [37].

On the other hand, the grain boundary source model attributes the dependence of grain size on yield strength to the influence of dislocation density. In this model, the grain boundary may itself act as a dislocation source; the capacity to emit the dislocations being dependent on the character of the grain boundary. The yield stress in this case is given in terms of the dislocation density by [30,37]:

$$\sigma_y^{GB} = \alpha G b \rho^{1/2}, \quad (2.7)$$

where α is a constant between 0.3 – 0.6 and ρ is the dislocation density. The dislocation density, ρ , is inversely proportional to the grain size, i.e., $\rho \propto 1/d$, which leads to the same dependence on grain size as given by equation (2.6). The increasing evidence that grain

boundaries are effective dislocation sources makes this model more plausible than the dislocation pile up model [30].

2.1.3 Strain hardening

Strain hardening refers to the increase in strength that occurs when dislocations glide, interact and change their distribution and density during plastic deformation. The significant increase in dislocation density that typically accompanies plastic deformation and the corresponding increase in dislocation glide resistance form the basis for strain hardening. Dislocation multiplication can arise from a number of sources such as Frank–Reed sources, multiple cross slip mechanisms, and from condensation of vacancies. Dislocation glide resistance, on the other hand, can be due to the interaction between stress fields of dislocations and dislocation reactions that produce sessile locks and dislocations jogs [37,38].

In general, the theoretical relationship between CRSS and dislocation–dislocation interactions, $\Delta\tau^{SH}$, is given as:

$$\Delta\tau^{SH} = \alpha G b \rho^{1/2}, \quad (2.8)$$

where G , b and ρ are as previously defined. α is a constant of the order of 0.1. Further analysis of equation (2.8) leads to a parabolic relationship between shear stress and strain, ε , of the form [38]:

$$\Delta\tau^{SH} = \alpha G \left(\frac{b}{x}\right)^{1/2} \varepsilon^n, \quad (2.9)$$

where x is the distance a dislocation glides through before being stopped by a network of other dislocations.

Equation (2.9) holds for most polycrystalline materials regardless of the arrangement of dislocations as long as the flow stress is mainly governed by dislocation–dislocation interactions in multiple slip planes. This is however not always the case for single crystals; their stress–strain curves are not parabolic but rather exhibit different stage behaviours that depend on crystal structure, crystal orientation, testing temperature and

purity. Another drawback of equation (2.9) is that dislocations do not move as individual defects as assumed by the model but rather they move as groups of dislocations creating slip bands [38,39]. The modern approach therefore is to examine the different stages of hardening in a material and then attempt to explain the mechanism that is likely to give rise to the different stages. Comprehensive treatments of the theory of strain hardening in FCC metals including the various stages of hardening can be found in literature [38–41].

2.1.4 Precipitation strengthening

The presence of precipitates in the matrix of an alloy gives rise to changes in both the mechanical and physical properties of the alloy. These changes can be very significant depending on the size, shape and volume fraction of the precipitates, in addition to the nature of the precipitate/matrix interface, i.e., whether the precipitates are coherent or incoherent with the matrix. The significant improvement in mechanical properties associated with the presence of precipitates, particularly in strength, typically arises from the interaction between the precipitates and dislocations. In general, a gliding dislocation must either cut through the precipitates lying along its glide plane or bypass them by bowing around them. The dislocation usually adopts the mechanism offering the lowest resistance [38,39]. The specific mechanism by which a dislocation overcomes the resistance posed by a precipitate is however complicated and varied. Typically, mechanisms associated with precipitate shearing include: stacking fault–, modulus–, coherency–, and order– hardening, while the mechanism associated with precipitate bypass is Orowan hardening. In the following paragraphs, the main features of these mechanisms, in addition to the theoretical relationships that estimate the magnitude of the strength arising from them, are highlighted. Detailed treatment of these mechanisms can be found in the literature [42,43].

Stacking fault hardening

In alloys with low stacking fault energy, a perfect dislocation normally dissociates into two partial dislocations because it is more energetically favourable for the dislocation to glide as partials than as a single perfect dislocation. Considerable strengthening can be achieved in such an alloy system if its stacking fault energy is different from that of coherent precipitates imbedded in its matrix. The difference between the separation distance of the partial dislocations in the matrix and the coherent precipitates leads to significant changes in the line tension of the dislocation that ultimately govern the strength of the al-

loy. The increase in the CRSS of underaged alloys due to stacking fault hardening, τ^{SF} , is given as [42]:

$$\Delta\tau^{SF} = \Delta\gamma^{3/2} \left(\frac{3\pi^2 fr}{32\Gamma b^2} \right)^{1/2}, \quad (2.10)$$

where $\Delta\gamma$, the change in stacking fault energy, is the magnitude of the difference between the stacking fault energies of the matrix, γ_{sfm} and the precipitates, γ_{sfp} ; Γ is the line tension of the dislocation; f and r are the volume fraction and average radius of the precipitates respectively. Equation (2.10) is satisfied as long as the width of the stacking fault in the matrix, w_m , is greater than 2 times the average planar radius of the precipitates, r_s , where r_s is given as $\pi r/4$. Different approximations apply outside the underaged regime. Specifically, for strong large particles, the CRSS is given as:

$$\Delta\tau^{SF} \approx \left[\frac{Kf}{\gamma_{sf}} \right]^{1/2} \frac{\Delta\gamma}{b} r^{-1/2}, \quad (2.11)$$

where K is the force of interaction between two partial dislocations of Burgers vector, b_p , and γ_{sf} is the average stacking fault energy. K and γ_{sf} are expressed as:

$$K = \frac{Gb_p^2}{8\pi(1-\nu)} (2 - 3\nu + 4\nu \sin^2 \xi), \quad (2.12)$$

$$\gamma_{sf} = \frac{\gamma_{sfp} + \gamma_{sfm}}{2}, \quad (2.13)$$

respectively, where ν is the Poisson's ratio of the matrix and ξ is the angle between the dislocation line and its Burgers vector. ξ is equal to 0 for initially pure screw dislocations and is equal to $\pi/2$ for initially pure edge dislocations.

Modulus hardening

Modulus hardening refers to strengthening that is due to a difference in shear modulus between a precipitate and the surrounding matrix. A dislocation gliding through an alloy with such difference in modulus experiences a resistance arising from its interaction with the associated stress fields. Although this interaction occurs outside the precipitate, it is strongest when the dislocation actually penetrates into the precipitate. It has also been shown that the interaction of screw dislocations with precipitates in such alloys is more than a factor of three stronger than with an edge dislocation. Thus, only the interaction of screw dislocations that have penetrated the precipitates are considered in modulus hardening models [42,43]. The increase in CRSS for undissociated, i.e., perfect dislocations in the underaged regime arising from modulus hardening, τ^{MH} , is given as [43]:

$$\Delta\tau^{MH} = 0.044G\epsilon_G^{3/2}f^{1/2}\frac{(F(r/b))^{3/2}}{(r/b)}, \quad (2.14)$$

where $F(r/b)^{3/2}/(r/b)$ is a function which governs the underaged regime where the behaviour holds. Estimates of this function can be found in the literature [43]. ϵ_G , the modulus misfit parameter, is given as $(G_p - G)/G$, where G_p and G are the shear moduli of the precipitate and the matrix respectively. Equation (2.14) is scaled down by a factor of 0.125 when the dislocations are dissociated, this is partly because the burger vector of a partial screw dislocation is only half that of the full dislocation.

Coherency hardening

Coherent precipitates with the same crystal structure as the matrix but with slightly different lattice parameter give rise to stress fields that can offer significant resistance to the glide of dislocations. The increase in strength, $\Delta\tau^{CH}$, arising from the interaction of undissociated dislocations with the stress fields of spherical coherent precipitates with an effective size misfit parameter, ϵ_s , is given as [43]:

$$\Delta\tau^{CH} = 4.02G\left(\frac{\epsilon_s^3 fr}{b}\right)^{1/2}, \quad (2.15)$$

where ϵ_s , is given as:

$$\epsilon_s = |\delta| / \left(\frac{2G(1 - 2\nu_p)}{G_p(1 + \nu_p)} \right). \quad (2.16)$$

ν_p is the Poisson's ratio of the precipitate and δ is related to the difference in lattice parameters of the precipitate, a_p , and the matrix, a , and is given by $\delta = (a_p - a)$. As in the case of modulus hardening, modifications to equation (2.16) are necessary when the dislocations are dissociated. Implementation of such modifications leads to:

$$\Delta\tau^{CH} = 0.44Gf^{1/2}\epsilon_s^{3/2} \left(\frac{r}{b} \right). \quad (2.17)$$

Order hardening

Order hardening is a strengthening mechanism usually associated with alloys containing coherent-ordered precipitates. An antiphase boundary (APB) is created on the slip plane of an ordered precipitate upon shearing by matrix dislocation. The energy of the APB per unit area, γ_{APB} , represents the resistance that must be overcome by the matrix dislocations for slip to occur. A major characteristic of alloys strengthened by order hardening such as Ni-Al and Al-Li alloys is that the dislocations tend to pair up at characteristic distances, where the second dislocation of the pair moving in concert with the leading dislocation restores order in the precipitates [42–49]. According to Argon [43], the CRSS, τ^{OH} , derived from the glide of pairs of loosely coupled dislocations in the underaged regime of a ordered strengthened alloy is given as:

$$\tau^{OH} = \frac{\gamma_{APB} * f^{\frac{1}{2}}}{2b} + \left[1.731 \left(\frac{\pi r \gamma_{APB}}{4Gb^2} \right)^{\frac{1}{2}} - f^{\frac{1}{2}} \right]. \quad (2.18)$$

The term “loosely coupled” indicates that the mean spacing between the dislocation pairs is significantly larger than the average diameter of the precipitates. A modified form of equation (2.18) applies near the peak aged regime when the precipitates become relative large and strong, and the mean spacing between the pairs decreases. This is given as [44]:

$$\tau^{OH} = 0.81 \frac{\gamma_{APB}}{2b} \left[\left(\frac{3\pi f}{8} \right)^{\frac{1}{2}} - f \right]. \quad (2.19)$$

Orowan hardening

The Orowan hardening model predicts resistance to dislocation glide provided by nonshearable precipitates or impenetrable particles. In other words, since the precipitates do not deform with the matrix, the CRSS derives from the shear resistance necessary to extrude the dislocations through a field of precipitates by bowing the dislocations around the precipitates. A dislocation extruding through a field of precipitates usually reaches a semi-circular configuration where the opposing arms of the dislocation wrap around the precipitate. Treatment of the contributions from both edge and screw dislocations as if they are separate mechanisms and applying the Pythagoras additive rule results in [43]:

$$\Delta\tau^{DH} = 0.132G\psi(f)\frac{\ln(r/b)}{(r/b)}, \quad (2.20)$$

where $\Delta\tau^{DH}$ is the increase in CRSS due to Orowan (dispersion) hardening. The function $\psi(f)$ is given as:

$$\psi(f) = \frac{f^{1/2}}{(1 - 1.085f^{1/2})}. \quad (2.21)$$

This mechanism is usually dominant in overaged alloys when the precipitates become nonshearable as a result of their large sizes or loss of coherency. Although the contribution to strength from this mechanism is usually less than obtained in other strengthening mechanisms, the dislocation loops, dipoles and other debris left around the precipitates during the bypass of the dislocations leads to a high rate of work hardening in dispersion strengthened alloys [39].

2.2 Plastic instability

2.2.1 Basic principles

As mentioned earlier in the introductory chapter, the term plastic instability refers to repetitive yielding that occurs in certain alloys during plastic deformation at critically low strain rates and over a range of temperatures, typically above room temperature. This phenomenon is also commonly called Portevin–Le Chaterlier (PLC) effect after the French scientists, Albert Portevin and François Le Chaterlier, who were among the first to report the phenomenon [17]. The repetitive yielding, which is often referred to as “jerky” or “serrated” flow represents a material instability that results in severe strain localization, reduction in ductility and formation of striations on the surfaces of sheet metals during forming processes. The combination of these deleterious effects with the environmentally induced embrittlement that may occur during service further accelerates the failure of the materials susceptible to PLC–type plastic instability [9].

The term, plastic instability, as used in this work is different from other kinds of material instabilities, such as the yield point and the necking phenomena, which are also sometimes referred to as plastic instability. Yield point phenomenon occurs only at the onset of yielding and it is marked by an abrupt drop in yield strength, which in most cases, is followed by a region of almost constant stress. The material afterward shows a typical strain hardening behaviour. Within the constant stress region, localized bands of plastic deformation, also known as Lüders bands, nucleate and spread out over the entire length of the sample [50]. These Lüders bands, like PLC–type plastic instability, degrade the surface quality of the deformed part. The yield point phenomenon is induced by the rapid multiplication of dislocations or the unpinning of dislocations initially locked by solute atoms at the upper yield point. The increase in the density of dislocations however leads to a lowering of the flow stress and subsequent strain hardening. The phenomenon, unlike the PLC type plastic instability, is not repetitive as the time scale for the diffusion of the solute atoms is much larger than the duration of the test [51]. The necking phenomenon, on the other hand, refers to a material instability behaviour that begins at maximum load during tensile deformation of a material that strain hardens. The strain become localized and the materials “necks” when the increase in stress due to a decrease in the cross sectional of the specimen becomes greater than the increase in the load–bearing capacity of

the material due to strain hardening [30]. Although the necking phenomenon leads to strain localization, it is not repetitive like the PLC-type plastic instability; it only occurs when the maximum tensile strength of the material is reached.

A number of factors, both extrinsic and intrinsic, have been shown to influence plastic instability. Common extrinsic factors include: the surface quality of the samples [2], loading mode of the test machine, i.e., load controlled versus displacement controlled [17], strain rate [11,57] and temperature [1]. However, strain rate and temperature have by far the most significant influence on plastic instability. The realisation of this has led to the construction of PLC domain maps which are diagrams that essentially show the range of temperatures and strain rates where plastic instability occurs for specific materials [1,9,20]. In general, very low strain rates and moderate temperatures are known to favour the occurrence of plastic instability. Typical intrinsic properties that can significantly influence plastic instability are alloy composition [5,22,58], concentration of the solute aging species [59] and precipitation [22,58,60]. For instance, solute species such as Mg and Zn are known to be potent strain aging agents in substitutional solid solution alloys such as Al alloys; their effect being more pronounced with increase in concentration. Grain boundaries [61] and anisotropy [62], although to a lesser extent, have also been shown to influence this phenomenon.

Plastic instability is known to lead to the formation of localized deformation bands, which are static or propagating, within the sample [17]. Three distinct types of deformation bands induced by the phenomenon have been identified with the aid of local strain monitoring techniques such as digital image correlation (DIC), acoustic emissions (AE), dynamic digital speckle pattern interferometry (DSPI) and laser scanning extensometry (LSE) [9,54]. The main distinction between these bands, which are known as type A-, B- and C-bands is the manner in which the deformation bands are spatio-temporally arranged in the gauge length of the sample. The spatio-temporal arrangement is a function of the strain rate and corresponds to well-defined serrations in the stress-strain curve [55,56]. Type A bands occur at high strain rates and are associated with continuous band propagation along the gauge length of the sample and quasi-periodic serrations that correspond to the nucleation of new bands. Type B bands occur at moderate strain rates and are associated with intermittent band propagation, resulting in serrations which are additional-

ly superimposed on the serrations typical of type A. Type C bands occur at very low strain rates and are randomly nucleated non-propagating deformation bands. The stress-strain curve is heavily serrated in this case; the serrations corresponding to random nucleation and release of bands of dislocations [9,17,54–56]. A systematic illustration of the shape of the stress-strain curve associated with the different types of deformation bands is shown in Fig. 2.1.

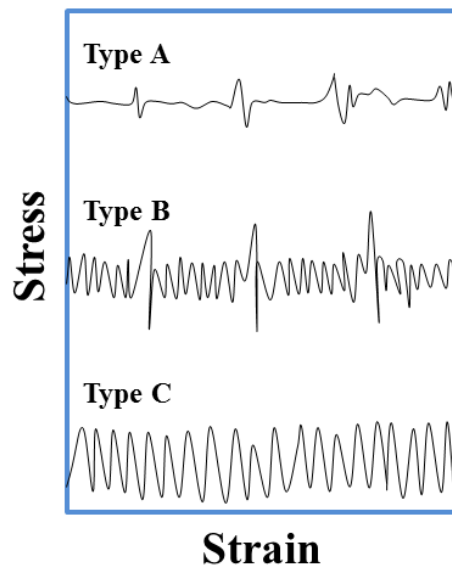


Fig. 2.1: Schematic illustration of the shape of the stress vs. strain curves corresponding to the three different types of spatio-temporal arrangements of deformation bands associated with plastic instability.

2.2.2 Plastic instability in solution strengthened Al–Mg based alloys: current understanding

Al–Mg based alloys are the most important solution strengthened Al alloys that exhibit plastic instability. These alloys are by far the most studied with regard to plastic instability [63] and as such provide a good foundation for understanding the mechanisms that govern plastic instability in other Al based alloy systems. These studies are mainly motivated by the need to improve formability, a material property that is severely degraded by plastic instability. Al–Mg based alloys are used extensively for light weight structural applications in the automobile and beverage packing industries where good formability is an important requirement [1].

The microscopic mechanism leading to plastic instability in Al–Mg alloys has been explained by a number of models. The most widely accepted model is based on dynamic strain aging (DSA), i.e, the interaction between temporarily trapped clustered mobile dislocations and forest dislocations. It is argued that the diffusion of solutes with sufficient mobility, Mg atoms in this case, to mobile dislocations during their arrest time at the forest dislocations leads to an increase in the strength required to liberate the mobile dislocations from the forest dislocation junctions. Under these conditions, the material exhibits inverse strain rate sensitivity, more commonly known as negative strain rate sensitivity (nSRS), which ultimately manifests macroscopically as serrations in the stress–strain curves [17]. The nSRS arises because the stresses required to liberate the clustered mobile dislocations from the forest dislocation are higher than those required to keep the mobile dislocations in motion upon their release. The amount of solute that diffuses to the trapped mobile dislocations, and by extension, the ‘break–free’ stress, is a function of the waiting time at the junction between the trapped mobile dislocations and the dislocation forest. This in turn depends on the strain rate and the average dislocation density. The lower the strain rate, the longer the waiting time and the higher the flow stress. At higher strain rates, the waiting time is short and as such the amount of solutes that cluster on the trapped mobile dislocations is small and insufficient to produce an effective enhancement of the flow stress [1,10].

Although, DSA was assumed to be the microscopic mechanism that gives rise to nSRS, the underlying mechanism of DSA itself, particularly in terms of the governing diffusion mechanism is still been debated. It was initially envisioned that clustering of the solute atoms on the temporarily trapped dislocations occurred by vacancy–assisted bulk diffusion, i.e. the diffusion of the solute atoms to the trapped dislocations from the region near the forest dislocation. It was however shown that the diffusion coefficients associated with this diffusion mechanism are too low to permit DSA to occur [52–53]. Pipe diffusion mechanism, i.e., the diffusion of solute atoms from solute clustered forest dislocations to temporarily trapped but unclustered mobile dislocations along the core of the mobile dislocations, has also been proposed as the governing diffusion mechanism for DSA [12]. However, recent atomistic simulations of the pipe diffusion of Mg atoms along the dislocation core in Al suggest that pipe diffusion is also too sluggish to produce sufficient aging and by extension strengthening of the trapped mobile dislocations in the temperature range

of plastic instability [52]. A more current understanding of the underlying diffusion mechanism for DSA is the ‘cross core’ diffusion mechanism proposed by Curtin and co-workers [53]. This mechanism involves the single-atomic jump of solute atoms from the compression to the tension side of a dislocation core. The model, supported by kinetic Monte Carlo simulations, shows that the driving force for the atomic jump is the large enthalpy difference between solutes on either sides of the dislocation core in addition to a reduced diffusion activation enthalpy in the core relative to the regions outside of the core.

As just described, atomistic simulations [52] and theoretical modelling [18–20] have shown that DSA, regardless of the governing diffusion mechanism, cannot independently lead to plastic instability. This has led to the development of alternate models to describe the origin of plastic instability in solution strengthened alloys.

Hähner [18,66] proposed that the combined action of DSA and long range dislocation interactions is necessary for nSRS and thus serrated flow to occur. Their model is based on a treatment of dynamically interacting dislocations as an effective fluctuating medium. It was argued that the primary consequence of DSA is to lower the SRS. This in turn leads to an enforced coupling of dislocations and consequently a narrowing of the aging time distribution. In other words, DSA makes the otherwise disordered mobile dislocations susceptible to collective glide. It was further argued that once the dislocations become condensed into a macroscopically collective mode of slip, the SRS may also become negative and plastic instability will occur. Although this model attempts to explain the relationship between DSA and the deformation bands observed macroscopically in the gauge length of test samples during deformation, the physical basis of the coupling of dislocations and the synchronization of the aging time aided by DSA is open to debate. For instance, collective glide of dislocations is reported even for pure metals where DSA is not expected [64,65], an indication that DSA is not a requirement for coupling dislocations as suggested in the model. More so, the model does not account for nSRS.

A model proposed by Picu [10] is entirely based on the strength variation of dislocation junctions due to the presence of solute clusters on forest dislocations. This model circumvents the DSA model and rather envisions that the solute clusters form on forest dislocations rather than on mobile dislocations since the resident time of forest dislocations is

much longer than the latter. In other words, solute diffusion does not need to occur very quickly for the aging process to take place. It was argued that the strength of a junction between a mobile dislocation and a clustered forest dislocation is a function of the cluster size, which in turn is a function of the imposed strain rate and the rate of forest production. Analogous to the DSA model, deformation at very low strain rates imply longer aging time and therefore higher strengths in comparison to deformation at high strain rates, a condition that leads to nSRS. Although this model qualitatively reproduces a number of key features observed macroscopically in alloys susceptible to plastic instability, the model is regarded as only a proof of concept partly because of simplifications made in the procedure of averaging over the population of dislocation junctions. More so, the model is restricted to only the Lomer–Cottrell type of dislocation lock.

A recently proposed rate–dependent constitutive model by Soare and Curtin [20] appears to give a more realistic picture of the microscopic origin of plastic instability. The main idea of the model is that solute aging of both temporarily trapped mobile dislocations, i.e. DSA, and solute aging of forest dislocations formed during plastic deformation must take place concurrently for plastic instability to occur. The aging of both dislocation types is governed by the cross–core diffusion mechanism. It was argued that DSA controls the overall rate dependence and assists in achieving nSRS by reducing the SRS to nearly zero. DSA was shown to account for the transients that accompany a sudden change in strain rate. The backstress exerted by the aged forest dislocations on the mobile dislocations produces the nSRS that gives rise to plastic instability. They showed that the forest dislocations are able to produce nSRS because the strength of the forests increases with increase in aging time. The aging time of the forests, on the other hand, is inversely proportional to the applied strain rate. Although it was shown that the model accurately predicts the strain rate (both steady state and transient), temperature and concentration dependence of plastic instability in a number of Al–Mg alloys both qualitatively and quantitatively, the authors suggested that the plastic instability should not occur in precipitation strengthened alloys such as Al–Li alloys since forest hardening is negligible in such alloys. There is however ample evidence that plastic instability occurs in precipitation strengthened alloys [63], an indication that a mechanism different from that proposed by Soare and Curtin [20] for Al–Mg alloys may be responsible for plastic instability in Al–Li based alloys.

2.2.3 Plastic instability in precipitation strengthened Al–Li based alloys: current understanding

Plastic instability has been observed in several binary and multi-component Al–Li alloys [63]. However, there are inconsistencies in the reported behaviour of these alloys, particularly in terms of the influence of temper state on the appearance and disappearance of plastic instability. For example, Deschamps and collaborators [58] observed serrated flow in an AA2196 alloy with 2.1wt% Li in solution treated (ST), naturally aged (NA) and underaged (UA) states. However in an AA8090 alloy with 2.38 wt% Li, serrations observed in the ST temper disappeared completely upon natural aging [22]. Furthermore, Chmelik and collaborators [25] observed that serrations occurred in a binary Al–Li alloy with 2.35 wt% Li in the early stages of aging but were absent in the PA state, yet the serrations re-appeared in the overaged state (OA). Another group [67] reported that serrations occurred in all but the OA state in a quaternary Al–Li based alloy with 2.9 wt% Li. The apparent lack of trend in the reported behaviour of these alloy systems with respect to the occurrence of plastic instability has led to debates about the origin of the instability in Al–Li based alloys. Some of the models that have been proposed to explain the origin of plastic instability in Al–Li based alloy systems are presented in the following.

A number of groups [21–25] attribute the occurrence of plastic instability in Al–Li based alloys to strain aging of temporarily trapped mobile dislocations by Li atoms, i.e., DSA. Proponents of this view associate the disappearance of the serrations to the depletion of Li atoms from the matrix as a result of the precipitation of δ' (Al_3Li) precipitates. One major setback of this view is the recent conclusion that DSA cannot exclusively lead to plastic instability [18–20,52]. Yet, forest aging which is proposed as the additional mechanism that has to occur concurrently with DSA for plastic instability to occur is considered negligible in precipitation strengthened alloys. Furthermore, there is strong indication in the literature [68] that dislocation pinning by Li atoms is unlikely in Al–Li alloys because of the weak binding energy of Li to dislocation cores.

In another mechanism proposed by Pink [26], it was argued that the large stresses that arise from dislocations that pile up at the interfaces of δ' precipitates in Al–Li based alloys, will lead to a shear of the precipitates and subsequently cause a large number of dislocations to collectively glide through the active slip plane within the precipitates. This,

they argue, will give rise to the stress drops observed in plastic instability. Although this mechanism seems plausible, it does not account for nSRS which is well known to be associated with plastic instability.

Brechet and Estrin [29] proposed a so-called pseudo-PLC model. The model was motivated by observations that the strengthening provided by precipitates can be reduced by repeated shearing of the precipitates by dislocations. Based on their theoretical model, they proposed that under certain conditions, the shearing of precipitates accompanied by their dissolution and subsequent rapid re-precipitation during deformation can independently lead to nSRS. The time and temperature requirements for the complete dissolution and re-precipitation of δ' after shearing however precludes the operation of such a mechanism at ambient temperatures [25,26].

Lastly, the model proposed by Behnood and Evans [27] considered the locking of dislocations within the δ' precipitates while shearing the precipitates as the origin of plastic instability in Al-Li based alloys. They noted that since dislocations involved in the shearing of δ' precipitates glide in pairs, one of the dislocations belonging to a pair may be positioned in a such way that part of it will lie in the matrix while the other part lies within the precipitate. It was argued that under such conditions a Li atom may jump from within the precipitate to the part of the dislocation lying in the matrix, such that the dislocation will be locked while in the process of gliding through the precipitate. Higher stresses will thus be required to continue deformation. It can be argued that this model is unlikely to lead to nSRS since it largely relies on dislocation pinning by Li atoms. As mentioned earlier in this section, the binding energy of Li atoms to dislocations is very weak and so do not generate significant locking [68]. More so, it is not clear what the driving force for the jump of the Li across the α/δ' interface is. The plausibility of the model is thus open to debate.

The preceding discussion of the current understanding of plastic instability in Al-Li based alloys demonstrates that the origin of the mechanism(s) governing plastic instability in precipitation strengthened Al-Li based alloys is not yet established. To this end, as already stated in section 1.1, the present work is aimed at examining the influence of precip-

itation on plastic instability and more importantly, identifying the microscopic origin of plastic instability in these alloys.

3 Experimental material and methods

This chapter begins with a review of the microstructural constituents of Al–Cu–Li–Mg–Zr based alloys; the emphasis is on the key precipitate phases that occur in these alloys. Next, an overview of the techniques employed in this work to critically examine the influence of the precipitates on plastic instability is presented. These techniques include those that allow for a characterization of the mechanical response of the test alloy such as nanoindentation and micro–tensile testing, and those that facilitate a characterization of its microstructural constituents such as transmission electron microscopy (TEM), *in situ* TEM tensile straining, high energy x–ray diffraction (HEXRD) and atom probe tomography (APT).

3.1 Microstructure and precipitation in Al–Cu–Li–Mg–Zr based alloys

The new generation of Al–Cu–Li–Mg–Zr based alloys exhibit an excellent combination of low density, high elastic modulus and high specific strength. The significant improvements in these properties in comparison to the conventional 2XXX alloys make them candidate structural materials for next generation aerospace applications [69–72]. The attractive properties of these alloys are associated with the presence of Li which enables the formation of several strengthening precipitates including δ' (Al_3Li), δ (AlLi), T_1 (Al_2CuLi), T_2 (Al_5CuLi_3) and T_B ($\text{Al}_7\text{Cu}_4\text{Li}$). Other precipitates that have been reported in these alloys include GP zones, θ (Al_2Cu), θ' (Al_2Cu), Ω (Al_2Cu), S' (Al_2CuMg), β' (Al_3Zr) [71,77]. The chemical composition and thermomechanical treatment given to a particular alloy dictates which of these precipitates forms in the alloy.

Of the various precipitates that can form in these alloys, GP zones, T_1 , δ' , θ' and S' phases have been shown to govern most of the precipitation strengthening [71,73]. De-

pending on the alloying constituents, the peak aged temper can consist of a complex combination of these four phases. The T_1 phase in particular contributes the bulk of the strengthening and additionally reduces the tendency for strain localization, which is a major problem in these alloys [58,69,78,79]. In contrast, the δ' phase, which is a metastable, coherent, ordered phase with a Cu_3Au ($L1_2$) crystal structure and spherical morphology [72,74,78,79] is known to provide strengthening, but also to cause severe strain localization, decrease ductility and increase susceptibility to intergranular fracture [58,80]. The naturally aged temper can contain one or more of GPB zones, δ' and β' , depending on the starting composition [81,82]. The presence of Cu-rich clusters in the naturally aged temper has also been reported [58,83]. Overaging these alloys leads to the dissolution of most of the metastable phases mentioned above and/or their transformation into more equilibrium phases such as θ , δ , T_2 and T_B phases [76,84].

3.2 Thermal processing

The alloy used in the present study is an Al–Cu–Li–Mg–Zr alloy (AA2198) developed by ALCAN and supplied in the form of 3.2 mm thick plates. The composition range of the constituent elements of the alloy is given in Table 3.1. The alloy had been solution treated, water quenched, stretched to a strain of 2% and naturally aged for several months to produce the T351 temper, hereafter referred to as NA. The plates were received in the NA condition. Artificial aging treatments aimed at achieving different tempers and combinations of different precipitates within reasonable times was established on the basis of the time–temperature–precipitation diagrams proposed by Chen and Bhat [84] for a similar alloy, AA2195. Five different artificial aging treatments, using the NA temper as starting material, were carried out. The heat treatments were carried out in a laboratory tempering furnace with maximum operating temperature of 650°C. The aging schedule including the adopted nomenclature used to identify them in this work is given in Table 3.2. The heating rate for each aging treatment was 5°C/min. The samples were cooled in air after the treatments.

Table 3.1: Composition range of the major constituents of AA2198 given in at.%.

Element	Li	Cu	Mg	Ag	Zr	Si	Fe	Mn	Zn	Cr	Al
Conc.	3.11–	1.23–	0.29–	0.03–	0.01–	0.08	0.05	0.25	0.14	0.03	rest
(at.%)	4.27	1.48	0.80	0.12	0.05						

Table 3.2: Heat treatment schedule and reference ID.

Temper	Temper ID	Aging temperature (°C)	Holding time (mins)
Naturally aged	NA	25	–
Peak aged	PA	155	840
Underaged	UA	204	10
Near peak aged	N-PA	260	60
Overaged	OA	370	600

3.3 Microtensile testing

Microtensile dog-bone shaped samples with dimensions of 27 mm x 3 mm x 0.6 mm and gauge length of 11 mm were produced by wire-cut electro-discharge machining (W-EDM) from the short-transverse (S-T) direction of the heat treated samples. Characterization of the mechanical response of the heat treated samples was carried out in a Zwick universal testing station equipped with a non-contact multi-zone laser extensometer. The laser extensometer has a resolution of 1 μm and a scanning rate of 200 Hz. It thus facilitates the probing of the local strain distribution during straining in addition to the global strain response. A major requirement for measuring strains with this method is that contrasting markers must be placed along the axis of the sample. The position of each marker at the beginning of the test along with subsequent displacements in the respective positions is then recorded as the laser continuously scans along the axis of the sample. In this work, the local and global strains were calculated from the displacements between markers placed 1 mm and 10 mm apart respectively as shown in Fig. 3.1. Tests were conducted at constant strain rates in the range of $10^{-3} - 10^{-5} \text{ s}^{-1}$.

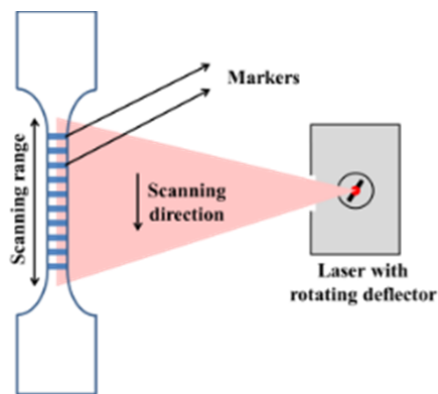


Fig. 3.1: Schematic of the microtensile sample showing markers placed 1 mm apart. The basic working principle of the laser scanner is also illustrated.

3.4 Nanoindentation

Mechanical properties such as hardness and modulus can be accurately estimated at the sub-micron scales with relative ease using nanoindentation testing. The hardness, H , and elastic modulus, E , of the material are calculated from the maximum load, P_{\max} , contact stiffness, S , and projected contact area at P_{\max} , A , using the following fundamental relationships [85]:

$$H = \frac{P_{\max}}{A}, \quad (3.1)$$

$$E_r = \frac{\sqrt{\pi} S}{2\beta \sqrt{A}}, \quad (3.2)$$

where β is a constant dependent on the geometry of the indenter used and E_r is the reduced modulus, defined as:

$$\frac{1}{E_r} = \frac{1 - \nu^2}{E} + \frac{1 - \nu_i^2}{E_i}, \quad (3.3)$$

where ν and E and ν_i and E_i are the Poisson's ratio and elastic modulus of the sample and indenter respectively.

With the assumption that the diameter of the indent does not recover during unloading, Oliver and Pharr [86] showed in their landmark publication that the contact stiffness can be estimated from the unloading curve of indents made with a Berkovich indenter. They showed that the unloading curve is best described by:

$$P = \alpha A(h - h_f)^m, \quad (3.4)$$

where P is the indenter load, h is the displacement of the indenter, m is a constant and h_f is the final displacement after unloading. α , m and h_f are all determined by least squares fitting procedure. The contact stiffness, S , is determined by differentiating equation (3.4) at the maximum depth, h_{\max} . The projected contact area is a function of the contact depth and is derived from an area function, $F(h_c)$, that describes the cross sectional area of the in-

denter at a distance, h_c back from the indenter tip. A general form of the area function and the relationship used to derive the contact depth are given in equations (3.5) and (3.6) respectively.

$$A = F(h_c) = C_1 h_c^2 + C_2 h_c + C_3 h_c^{1/2} + \dots + C_8 h_c^{1/128}, \quad (3.5)$$

$$h_c = h_{max} - \varepsilon \frac{P_{max}}{S}. \quad (3.6)$$

The parameter $\varepsilon P_{max}/S$ in equation (3.6) accounts for the displacement of the surface, h_s , at the contact perimeter. ε is a constant that depends on the geometry of the indenter. Fig. 3.2 is a schematic of an indenter loaded into an elasto–plastic material. Various parameters used in the preceding equations are highlighted in the schematic.

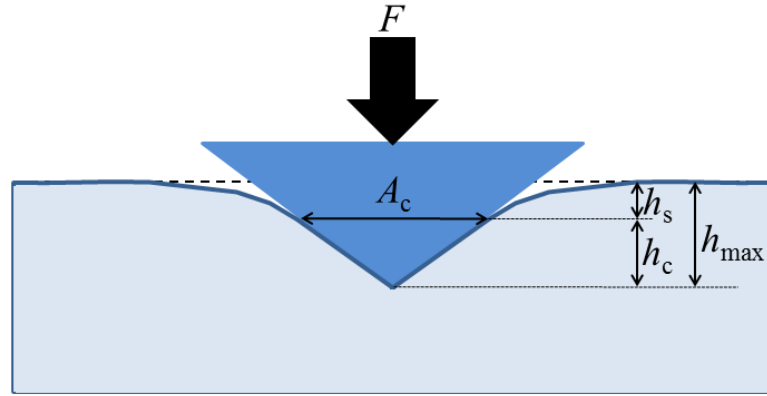


Fig. 3.2: Schematic illustration of an elasto–plastic material under the influence of a conical indenter.

A recently developed nanoindentation method [87] also allows for the determination of strain rate sensitivity parameter, m . The method is analogous to the strain jump tests performed in tensile experiments since the applied indentation strain rates can be changed to different values of interest within a single indentation test. The strain rate sensitivity parameter, m , is defined as the ratio of the variation of the log of nanoindentation hardness to the associated variation in the log of indentation strain rate, $\dot{\varepsilon}$, [87]:

$$m = \frac{\log \left(H_1/H_2 \right)}{\log \left(\dot{\epsilon}_1/\dot{\epsilon}_2 \right)}. \quad (3.7)$$

The indentation strain rate, $\dot{\epsilon}$, is the ratio of the displacement rate and displacement (\dot{h}/h). This ratio, (\dot{h}/h), approximately equals $0.5(\dot{P}/P)$, where \dot{P} is the loading rate.

The nanoindentation experiments in this work were carried out with a Nanoindenter[®] XP (Agilent, GmbH) equipped with a Berkovich indenter. A schematic representation of the main setup of the instrument is shown in Fig. 3.3. The Nanoindenter[®] XP performs indentation tests by driving a diamond indenter into the specimen surface and dynamically collecting the applied force and displacement data. The force is applied using an electromagnetic actuator, and a capacitive sensor is used to measure the displacement [88]. The load and displacement capacities of this instrument are 10 N and 50 μm , respectively, while the resolutions are 50 nN for the load and 0.01 nm for the measured displacement. Two different loading profiles, including constant strain rate and strain rate jump protocols, were used in the tests. The constant strain rate tests were performed at a strain rate of $5 \times 10^{-3} \text{ s}^{-1}$, while the strain rate jump tests were performed at three different indentation strain rates ranging from 0.01 to 0.0005 s^{-1} with a base strain rate of 0.05 s^{-1} .

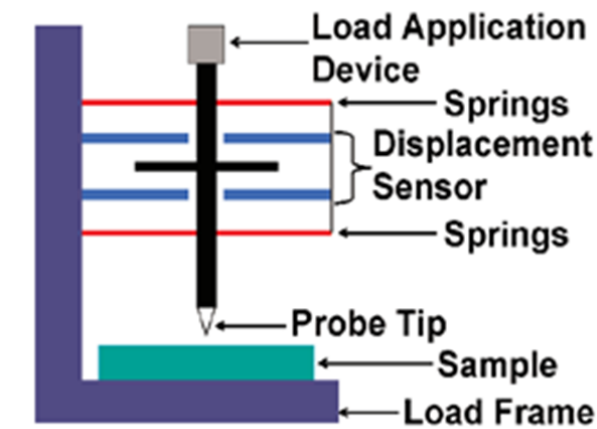


Fig. 3.3: Schematic illustration of the Nanoindenter XP (Taken from [88])

Samples used for the nanoindentation tests were prepared with conventional metallographic sample preparation techniques involving grinding and polishing operations. Coarse and fine grinding were carried out with 500 – 1200 grits grinding papers and with a 3 μm diamond disc, respectively. A final polishing step was carried out on a polishing cloth wetted with a colloidal silica oxide polishing suspension, OP–S.

3.5 Electron microscopy

The investigation carried out in this work requires careful characterization of the microstructural constituents of the different tempers. The dearth of microstructural information about AA2198 in literature further strengthens the need for detailed characterization. A number of electron microscopy based methods were employed to achieve this goal. Only a brief review of the working principles of these methods is given here, as there is an abundance of literature in this regard. A brief description of the sample preparation methods used to prepare samples for each of the microscopy methods is also discussed.

3.5.1 Scanning Electron microscope and Focused Ion Beam Milling

A Nova–200 dual–beam Scanning Electron/Focused Ion Beam (SEM/FIB) microscope, manufactured by FEI, Oregon, USA, was used in this investigation to prepare lamellae for transmission electron microscopy (TEM) and micro–tips for atom probe tomography (APT) investigation. The dual–beam microscope combines a high resolution field emission SEM column, with a high current gallium (Ga) liquid metal ion FIB column, thus allowing users to switch between the two beams for quick and accurate navigation and milling. The microscope is also equipped with an *in situ* platinum (Pt) injection system and an Omniprobe micromanipulator for lift–out of cross sections or micro–tips milled by the FIB. Careful control of the energy and intensity of the Ga ions produced by the FIB column makes it possible to perform site specific and very precise sputtering or nano–milling of various shapes in a bulk sample.

The SEM column produces an electron beam that is focused into a fine spot, $\sim 10\text{nm}$ on the specimen surface and made to scan the surface in a rectangular raster. The focussed electrons interact with atoms on the sample surface, producing information about its topography and composition [39]. Specifically, crystallographic and chemical characterization of the sample can be achieved in the SEM using electron backscatter diffraction

(EBSD) and energy dispersion x-ray spectroscopy (EDS) methods, respectively. These methods were however not employed in this work because most of the precipitates in the alloy are unresolvable in the SEM.

A review of the different FIB methods used to fabricate samples for TEM investigation can be found in the literature [89,90]. The lift-out technique was used in this work to prepare most of the lamellae used for subsequent TEM analysis. A major advantage of this technique is that it results in minimal ion damage of the lamella in comparison to other method. Additionally, it is not critical to have a well-polished surface prior to milling [89]. The following is a list of the main steps used in the fabrication process:

- a) Deposition of a 500 nm thick Pt layer over the area of interest to minimize ion damage to the sample, Fig. 3.4(a). The deposition was done with a current of 1 nA.
- b) Coarse cross section milling of two staircase-like trenches on either side of the Pt deposited layer to produce a thin lamella as shown in Fig. 3.4(b). Typical dimension of the trench was 20 μm x 16 μm x 20 μm . Further cleaning cross section milling was afterwards carried out to remove the rough surfaces produced by the coarse milling step, to reduce taper at the base of the lamella and to thin down the lamella to a thickness of ~ 2 μm . The coarse and cleaning cross section milling steps were conducted with 3 nA and 1 nA currents, respectively.
- c) The lamella is then tilted to an angle of 7 degrees and partially cut-free as shown in Fig. 3.4(c) using a current of 0.5 nA. The free edge of the lamella is afterwards attached to the Omniprobe with a 500 nm thick layer of Pt.
- d) The lamella is thereafter cut-free, lifted out of the trench and attached to one of the fingers of a TEM Cu grid as shown in Fig. 3.4(d) and further thinned down, using a current of 0.3 nA, to between 100 – 200 nm to make it electron transparent.
- e) The final step involves low voltage and current (5 kV and 70 pA, respectively) cleaning at a glancing angle of 5 degrees to remove the ion-damaged surface layer on the lamella.

An electron transparent lamella ready for TEM investigation is shown in Fig. 3.4(f). The thickness of the lamella was measured in the SEM prior to the TEM investigation. This thickness was used in estimating the volume fraction of the precipitates.

Table 3.3: Typical annular milling dimensions and corresponding currents used for sharpening the tips used for the atom probe analysis.

Outer diameter (μm)	Inner diameter (μm)	Current (nA)
4.5	2.00	0.30
4.5	1.00	0.30
2.5	0.70	0.10
2.5	0.50	0.10
2.0	0.25	0.05
2.0	0.10	0.05

The lift-out method was also used in fabricating micro-tips for the APT experiments. The exact approach and parameters are however different from that used in preparing the TEM lamella. The main steps used in this case are listed below:

- a) Two rectangular trenches, about 2 μm apart, are milled at the area of interest to intersect at a depth of ~ 4 μm , Fig. 3.5(a). Each trench was milled at a glancing angle of 22 degrees using a current of 3 nA.
- b) One edge of the lamella is then cut free at the side where the Omniprobe will be inserted, Fig. 3.5(a). The other edge is cut free after the loose edge of the lamella has been attached to the Omniprobe with a thin layer of Pt. A current of 0.5 nA was used to attach the lamella to the Omniprobe and to cut it free from the bulk sample.
- c) A small wedge is then cut out from the lamella and glued to the top of a micro-tip post in the coupon with a layer of Pt, as shown in Fig. 3.5(b,c).
- d) Each wedge is subsequently sharpened to form a needle-like tip using annular milling techniques, as shown in Fig. 3.5(d). Typical dimensions and milling currents used for sharpening the tips are given in Table 3.3. The final diameter of the micro-tip is usually between 50 to 100 nm. The final step in the annular milling stage is also done with low voltage and low current as in the case of TEM sample fabrication.

3.5.2 Transmission electron microscopy

Transmission electron microscopy (TEM) was carried out in a JEOL 3010 microscope operated at 300 kV and a Philips CM200 microscope operated at 200 kV, at the National Centre for Electron Microscopy (NCEM), Berkeley, California and at Helmholtz Zentrum Geesthacht, respectively. Additional TEM samples, besides the FIB-prepared TEM lamellae, were prepared using more traditional methods. Specifically, the bulk sam-

ples were grounded down to thicknesses of approximately 120 μm using 1200 grits emery paper. 3 mm discs were subsequently cut out of the thin foils with a 3 mm punch. Electropolishing of the 3 mm discs to produce electron transparent foils was done in a twin-jet device with a solution of 67% methanol and 33% nitric acid at a temperature of $-20\text{ }^{\circ}\text{C}$ and current of 12 V.

The principles of operation of the TEM are now briefly given. When an electron beam strikes an electron transparent crystalline sample in the TEM, the transmitted electrons are either scattered, i.e. diffracted, in different directions or they travel through the sample without suffering any angular deviation. The scattered electrons may be inelastic or elastic, i.e. the electrons may or may not suffer a measurable loss of energy. The elastically scattered electrons can be further classified as either coherent or incoherent depending on whether they are in phase with one another or out of phase. Different types of contrasts are associated with these different forms of scattering that occur in the TEM [91]. Of particular interest to us in this work is diffraction contrast which arises because the intensity of the scattered beams in crystalline materials is a function of the crystal structure of the sample. The diffraction patterns associated with the diffraction contrast are essential for identifying the phases that are present in a sample. A number of diffraction patterns derived from well-known precipitate phases in Al-Li based systems are found in literature [35,76,81,92,93]. Systematics of the $\langle 100 \rangle_{\alpha}$ and $\langle 112 \rangle_{\alpha}$ zone axis diffraction patterns consisting of the spots and streaks expected for most of the phases in Al-Li-Cu-Mg-Ag alloys are shown in Fig. 3.6.

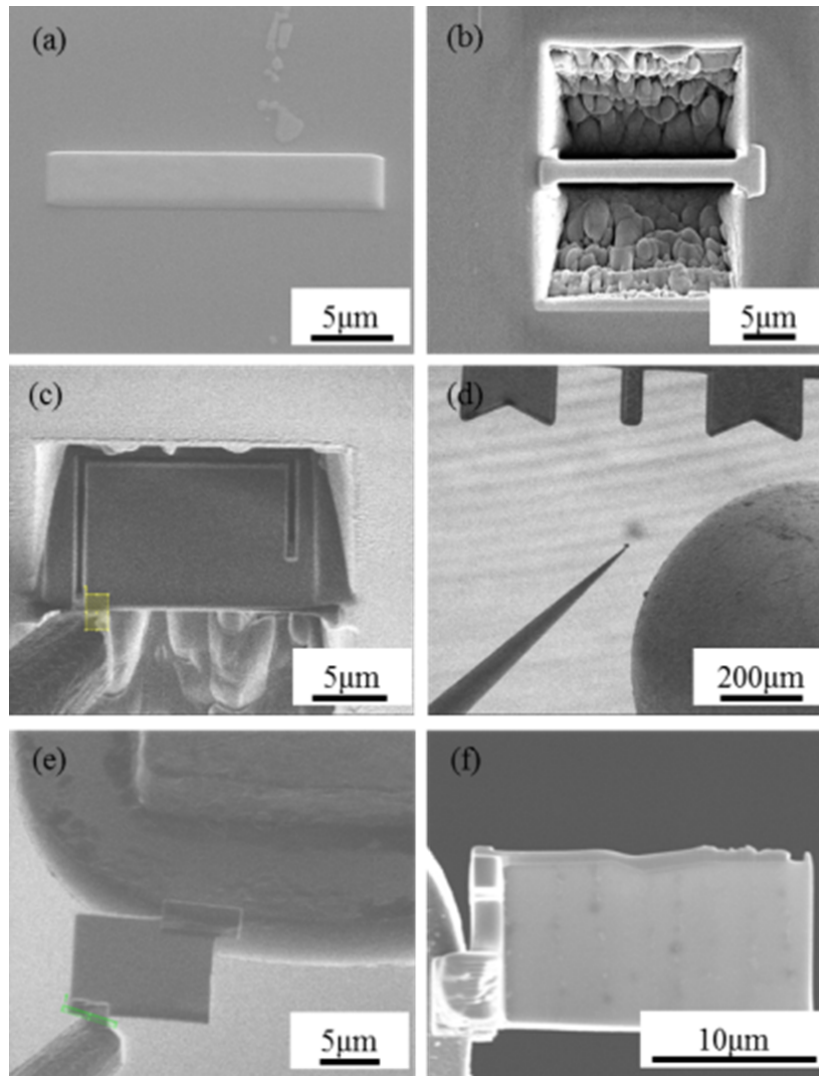


Fig. 3.4: Micrographs showing the main steps in TEM sample preparation with FIB. (a) Platinum (Pt) layer on sample surface. (b) Staircase-like trenches with lamella at the middle. (c) A lamella partially cut-free from the bulk sample. The region where the lamella is attached to the Omniprobe is also indicated. (d) Three fingers of a Cu grid, an Omniprobe containing a lamella and a section of the Pt deposition gun are shown in this micrograph. (e) A lamella being attached to one of the fingers of the Cu grid. (f) An electron transparent lamella attached to the Cu grid.

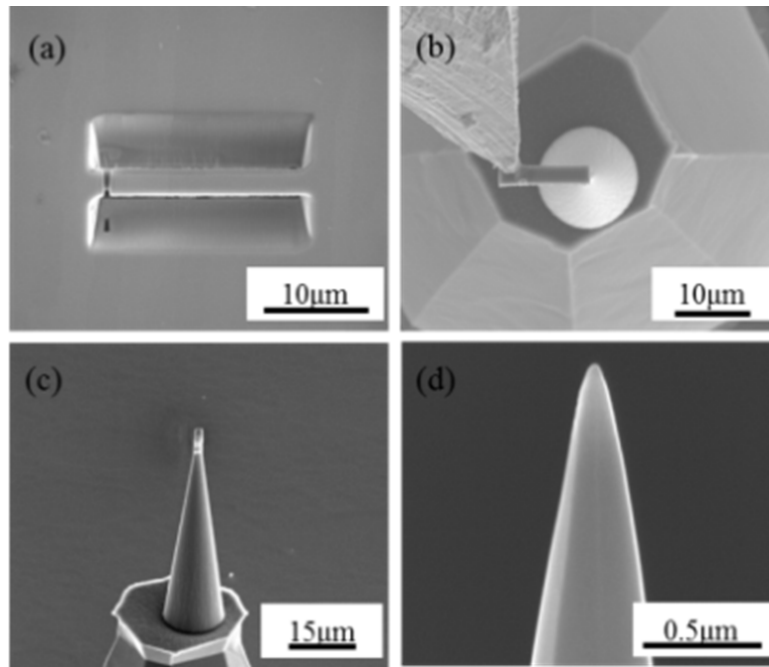


Fig. 3.5: Micrographs showing the main steps in APT sample preparation with FIB. (a) Lamella with one edge already cut free. (b) A wedge being attached to the top of a micro-tip post. (c) A wedge sitting on top of a post. (d) A finished APT tip after low kV cleaning.

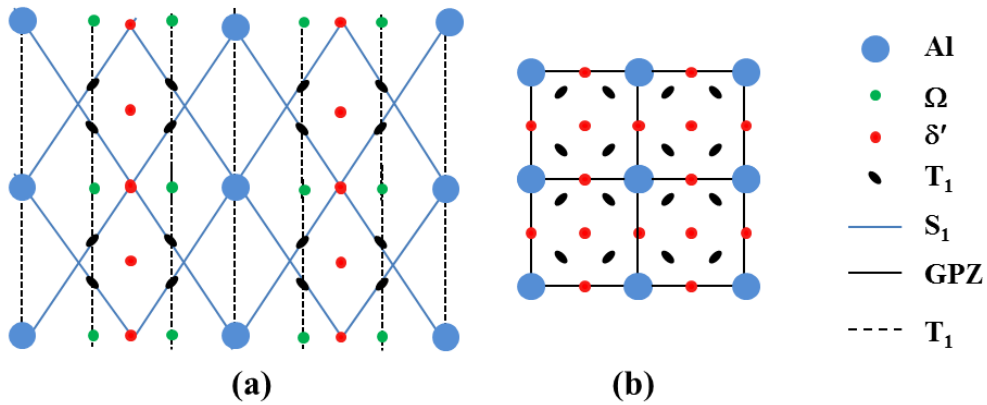


Fig. 3.6: Schematic illustration of the diffraction patterns observed in a typical Al-Li-Cu-Mg-Ag alloy after artificial aging. (a) $\langle 112 \rangle_\alpha$ (b) $\langle 100 \rangle_\alpha$ zone axes respectively.

3.5.3 *In situ* TEM straining

In situ straining in the TEM was carried out at NCEM, Berkeley, California in order to gain better insight into the dislocation–precipitation interactions. The *in situ* straining tests were conducted inside a JEOL 3010 microscope using a displacement controlled single tilt, straining specimen holder. The portion of the holder where the sample is fixed is shown in Fig. 3.7(a). The test samples were in the form of rectangular shaped thin foils, with dimensions: 12.5 mm x 2.5 mm x 120 μm . The foils were prepared from the short transverse direction of the bulk samples. The central region of these samples was electropolished in a twin jet polishing device using the same electrolyte and parameters described in the previous section. A schematic representation of the thin foil is shown in Fig. 3.7(b). The microscope is equipped with a Gatan Orius CCD camera that allows the recording of the experiments at a video rate of 33 frames per second.

The setup used in this experiment does not allow for an estimation of the applied stress, while the strain rate and strain can only be determined through indirect methods which usually result in large statistical variations. Dislocation analysis is also difficult during these experiments because the straining stage is single tilt. Furthermore, because of the high velocity of the dislocations encountered during these tests, typically about 10 nm/s [94], the dislocations of interest move rapidly until held up by obstacles such as precipitates or until they move outside the viewing screen. Thus, we have employed this technique only as a qualitative assessment of the dislocation behaviour.

3.6 High resolution x-ray diffraction

Complementary microstructural characterization using high-energy x-ray diffraction (HEXRD) was carried out at the HZG beamline HEMS at the Deutsches Elektronen-Synchrotron (DESY) in Hamburg, Germany. Samples with thickness of 4 mm were measured in transmission using a beam cross section of 1 mm x 1 mm. The samples were penetrated with high-energy x-rays with a photon energy of 100 KeV, which corresponds to a wavelength of 0.124 \AA . The resulting Debye–Scherrer diffraction rings were recorded on a 2-dimensional Perkin Elmer XRD 1622 detector with an exposure time of 0.1 secs. In order to reduce background noise, 40 images were summed for each sample, thus even weak peaks from phases with minor phase fractions were made visible. Conventional diffraction patterns were generated from the rings by azimuthal integration of the rings. Qual-

itative phase analysis was achieved by means of simulated diffraction patterns. The crystallographic data used for the analysis can be found in the appendix. The lattice parameter of the aluminium phase was determined by the Gaussian fitting method.

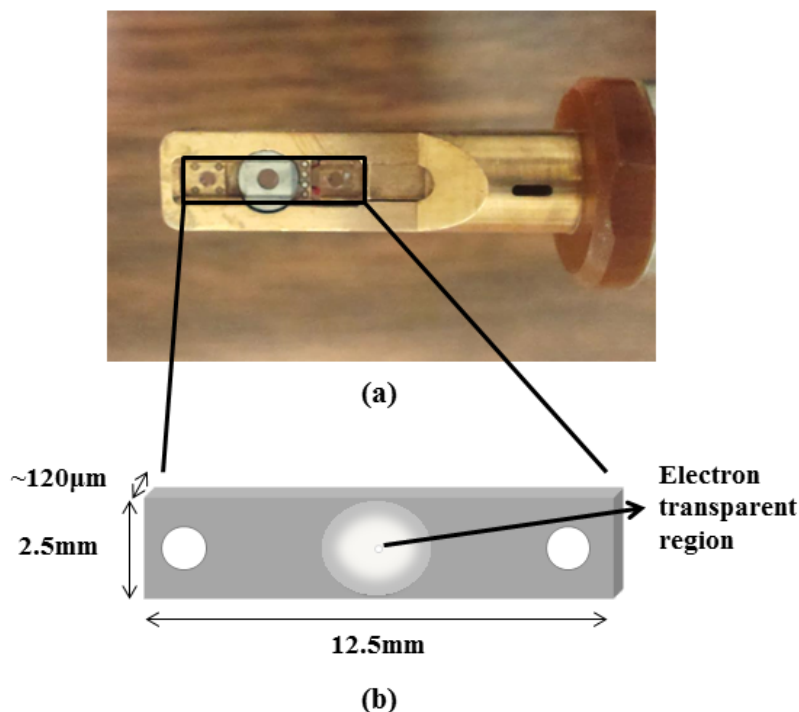


Fig. 3.7: Set up for the *in situ* TEM straining experiments. (a) The single tilt tensile holder. (b) Schematic of the shape and dimensions of the foil.

3.7 Atom probe tomography

Quantitative elemental analysis of both matrix and precipitate phases was carried out with a three-dimensional atom probe (3DAP), LEAP (Local Electron Atom Probe) 3000X HR, at the Max Planck Institute for Iron Research (MPIE) in Düsseldorf. 3DAP allows for the identification and quantification of individual elemental species in three dimensions, with a spatial resolution higher than that obtainable in other microscopy techniques. This unique capability of the 3DAP makes it an indispensable tool in the study of nanoscale precipitates found in precipitation strengthened metallic alloys such, as AA2198. Recent reviews of atom probe tomography can be found in the literature [95–97].

Atom probes typically combine a time-of-flight mass spectrometer with a position sensitive, sub-nanometer resolution detector, the operation of which permits full three-

dimensional reconstruction of a given volume of a sharp probe (specimen). The 3DAP used in this investigation is additionally equipped with a novel local electrode, which enhances the electric field at the sharp probe and allows fast pulsing (max. 200 kHz) at low voltage, and a wide-angle reflectron, which substantially enhances the mass resolution of the instrument. The system also incorporates an ultrafast laser with a pulse width of 10 ps and wavelength of 510 nm. A high voltage applied between the sharp probe, i.e., the sample, held at cryogenic temperatures and the local electrode creates a high electric field at the tip of the probe that allows the atoms to be stripped as ions from the probe tip. These ions are accelerated by the electric field toward the position sensitive detector. The use of sub-nanosecond laser or high voltage (HV) pulses enables the ions to be field evaporated in a controlled manner, i.e., one at a time. The original position of an ion in X and Y is determined from its hit position on the detector while the sequence of evaporation events is used to provide information about its Z position, i.e., its depth in the sample. The chemical identity of an ion is determined from its mass over charge ratio, M , which is given as [98]:

$$M = 2eV \left(\frac{t_{\text{flight}} - t_0}{L_{\text{flight}}} \right), \quad (3.8)$$

where e is the elementary charge of an electron, V is the total voltage, t_{flight} is the measured time of flight, i.e., the time it takes the ion to travel the distance from the probe tip to the detector, t_0 is a characteristic time shift which accounts for the time difference between the instant at which measurement is started and the actual application of the laser or HV pulse and L_{flight} is the flight distance. M is usually represented in the form of a histogram called a mass spectrum. The combination of the atom position and identity allows three-dimensional images of the elemental distributions to be reconstructed with near-atomic resolution. A schematic of the main working principles of an APT is shown in Fig. 3.8.

In this work, the APT was operated in the laser pulsing mode. In comparison to the HV pulsing mode, the laser pulsing mode requires lower DC fields and additionally provides a much larger field of view and higher pulse repetition rate. This makes the laser pulsing mode particularly well suited for Al alloys since it greatly minimises the preferential evaporation of Li and Mg from the Al matrix in the standing voltages. This is a com-

mon source of error in the HV pulsing mode [99]. Specifically, the laser pulse energy used was 0.6 nJ, the laser pulse repetition rate was varied between 100 and 250 kHz, the specimen temperature was set to 60 K, while the target evaporation rate was set to 1%.

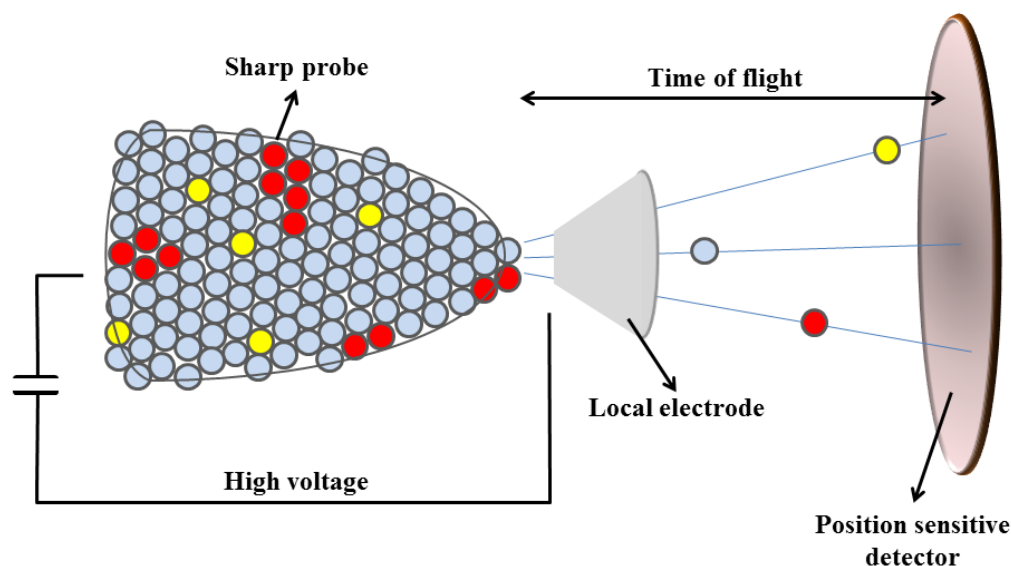


Fig. 3.8: Schematic of the working principle of an atom probe. The different coloured spheres represent different atomic species.

The APT specimens were produced by the standard lift-out procedure described in section 3.5.1. Although, the final annular milling was carried out at an accelerating voltage of 5 kV and a beam current of 70 pA, some Ga contamination was detected in the APT datasets. However, the corresponding peaks in the mass spectrum were ignored in the data analysis. There were also unusually intense peaks corresponding to AlH^+ and AlH_2^+ in the mass spectrum. This impedes the correct determination of the Si concentration, because both AlH^+ and $^{28}\text{Si}^+$ and $^{29}\text{Si}^+$ and AlH_2^+ have mass-to-charge ratios of 28 and 29 respectively. In this study, the peak at 28 Da was assigned to Si while that at 29 Da was assigned to AlH_2 . 3D reconstruction was performed in the software IVAS (version 3.6.8) by Cameca using the initial tip apex radii and shank angles measured in the SEM before the APT experiments.

Aside from facilitating the quantitative elemental analysis of both matrix phase and precipitates at the atomic scale, APT is also unique in its ability to provide information about atomic distributions, i.e., the so called clustering phenomena, in metallic alloy. A

number of cluster identification techniques are presently available to discern and characterize atomic-scale clusters from reconstructed APT data. A description of these techniques can be found in literature [98].

The most fundamental, albeit qualitative, method of discerning clustering is the k -order nearest neighbour distance distribution, k NN. This technique is based on the statistics of distributions of the interatomic distances within the immediate vicinity of each atom, with k referring to the number of nearest neighbour(s) used in the analysis. The analysis can include atoms of the same species, e.g. Cu–Cu or different species, e.g. Cu–Mg. Evidence for clustering is established by comparing the experimental distributions generated from distances separating each atom and its k th nearest neighbour with distributions generated from randomized simulations of the experimental data. A broadening of the experimental distribution and a shifting of the distribution maximum to smaller distances is indicative of the presence of clustering [98,100,101]. It should be noted that there is an intrinsic limitation of the APT technique, namely, its limited detection efficiency, which is about $\sim 37\%$ in the microscope used in this investigation. Although this limited detection efficiency increases the possibility of non-detection of clusters, its effect is largely circumvented by normalisation, which entails comparing the experimental and randomized distributions [101]. In this work, the random data was generated from the experimental data, with fixed atomic positions but with randomized chemical identities, while preserving the concentration of all the atomic species.

Accurate quantitative characterization of clusters, in terms of size, chemistry, morphology and volume fraction, is non-trivial, particularly when the detection limit of the APT technique is taken into consideration. There is presently no universally accepted method for identifying and characterizing solute clusters. Furthermore, the results generated by the cluster identification algorithms presently in use are very sensitive to the choice of parameters that define the algorithms [98,101]. In this work, cluster analysis was performed in the software 3Depict (version 0.0.17) using the core-linkage (CL) algorithm. This technique is amenable to alloy systems containing fine scaled clusters as well as large precipitates. The CL technique is a variation of the Density Based Clustering technique, in which clusters are defined as areas having a density higher than the remainder of the matrix. The density criterion is defined by a minimum number of atoms, N , within a

given distance. The first step in the CL technique involves determining so-called core atoms, i.e. solute atoms whose k th nearest neighbours (typically $k > 2$) are within the distance, d_{core} . In the next step, which is the linkage step, the atoms belonging to a particular cluster are established by grouping together atoms that are within a given distance, d_{link} , of the core atoms; $d_{\text{link}} < d_{\text{core}}$. As with other clustering techniques there are no established criteria for defining the cluster analysis parameters, namely k_{NN} , d_{link} and d_{core} . In this work these parameters were determined according to the heuristic method recently used by Marceau [102]. Specifically, d_{core} was set to the distance at which the difference between the cumulative 5th nearest neighbour distances (5NN) and its randomised counterpart was the highest while d_{link} was set to $\frac{1}{2} d_{\text{core}}$. Only core atoms consisting of a minimum of 3 atoms were considered as actual clusters.

4 Mechanical and microstructural characterization

In order to gain insight into the influence of precipitation on plastic instability in the alloy of interest, AA2198, the mechanical response of the aged samples in addition to the microstructural changes that accompany the various aging treatments were characterized with the methods introduced in the previous chapter. The results obtained from these tests are presented in this chapter.

4.1 Mechanical response

4.1.1 Microtensile tensile

Fig. 4.1 shows the true stress, σ_t , vs. true strain, ϵ_t , response of each temper. The tests were conducted at a strain rate of $5 \times 10^{-5} \text{ s}^{-1}$. The peak aged (PA) temper had the highest yield strength of 450 MPa with a correspondingly low uniform elongation. Other groups have reported a similar response for this temper [58]. The near peak aged (N-PA) temper attained a lower yield strength, 330 MPa, but displayed a uniform elongation comparable to that of the PA temper. The naturally aged (NA) temper also exhibited remarkably high yield strength, 310 MPa, and uniform elongation, in comparison to naturally aged samples of other 2xxx alloys [103]. Similar response was obtained in the underaged (UA) temper but with slightly lower yield strength. The lowest yield strength was obtained in the overaged (OA) temper. More importantly, the OA was the only temper that exhibited plastic instability. A portion of the stress-strain curve is magnified in the insert in Fig. 4.1 to more clearly reveal the stress drops in the curve, which are characteristic of plastic instability. It is noteworthy that the NA and UA tempers sustained higher plastic strain than the OA temper even though their yield strength is more than a factor of 2 higher than the latter. This observation underscores the detrimental effect of plastic instability on ductility.

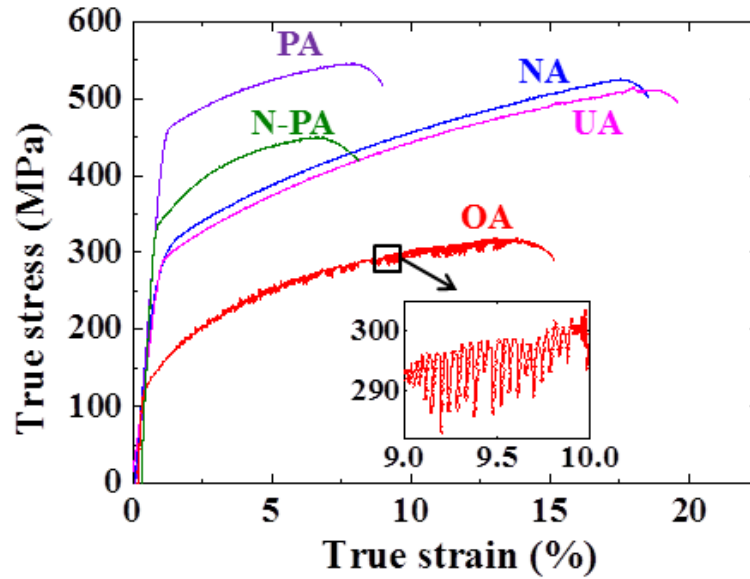


Fig. 4.1: True stress –true strain response of AA2198 for the various tempers considered: peak aged (PA) in purple, near–peak aged (N–PA) in green, naturally aged (NA) in blue, underaged (UA) in pink, and overaged (OA) in red. Plastic instabilities are only found in the overaged temper.

Fig. 4.2(a) shows a plot of local and global strains vs. measurement time for the OA temper. As earlier discussed in section 3.3, the local and global strains were calculated from the displacements between markers placed 1 mm and 10 mm apart along the gauge length of the tensile specimen, respectively. The true stress response is also superimposed on the plot. Plastic instability, as captured by the stress and global strain response, was not very obvious in the early stage of plasticity. However, the local strain response, characterized by large stepwise increases in strain, reveals that the onset of the instability occurs shortly after yielding. This observation highlights the localized and microscopic nature of plastic instability. The local strain response observed in all the samples is shown in Fig. 4.2(b) as a function of measurement time. The absence of stepwise increase in local strain in all but the OA temper additionally indicates that plastic instability only occurs in the OA temper

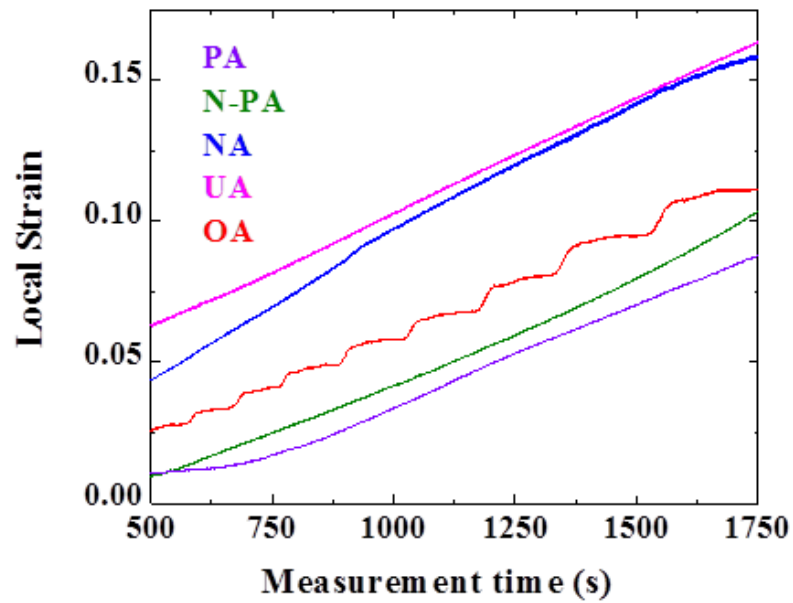
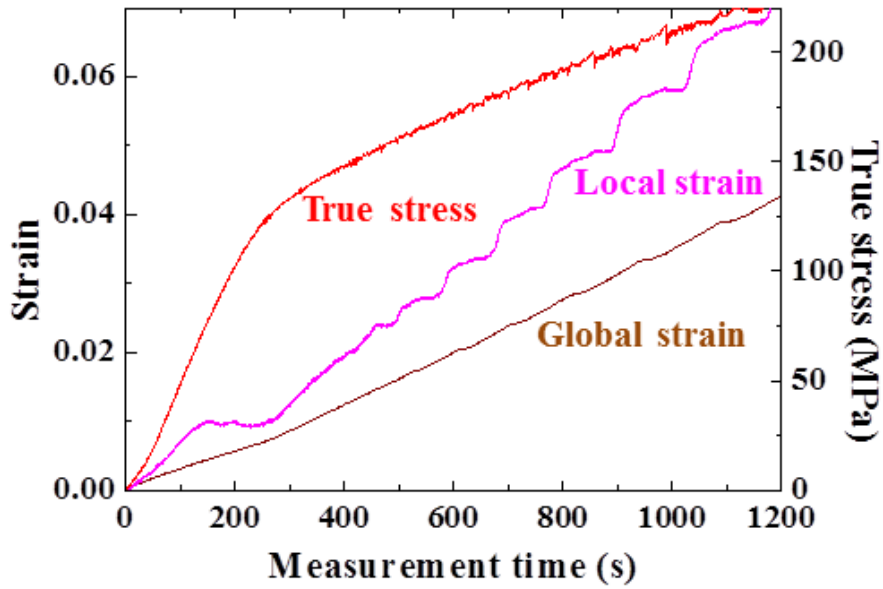


Fig. 4.2: (a) The local (in pink) and global (in brown) strain responses of the OA temper plotted as a function of time. The corresponding stress response is also shown in the plot. (b) The local strain response of all the five investigated tempers plotted as a function of time. Colour codes are as previously defined.

Fig. 4.3 is a plot of the work hardening rate ($d\sigma_t/d\varepsilon_t$) as a function of true strain. The evolution of the work hardening rate is similar in all five tempers, however the very early stage of plastic deformation in the N-PA and OA tempers showed significantly higher work hardening rates in comparison to the PA, NA and UA tempers; with the N-PA temper reaching the highest value. The high work hardening rate of the N-PA and OA tempers however decreased rapidly, after only about 2% plastic strain, to values lower than those obtained in the other tempers. This kind of response, namely the exceptionally high initial work hardening rate at the onset of plasticity followed quickly by a significant decrease, is typical of alloys containing a dispersion of incoherent, non-shearable second phase particles and is attributed to the back-stress exerted by the Orowan loops formed around the particles on subsequent mobile dislocations [104]. This mechanism is known to break-down after 2% plastic strain as a result of the plastic relaxation in the matrix and around the particles; geometrically necessary dislocations (GNDs) stored to accommodate the strain gradient between the deforming matrix and the non-deforming particle drive the plastic relaxation [104]. On the other hand, the initial work hardening rates such as those found in the NA temper have been attributed to increased strength of the dislocation junctions, owing to high solute contents [58]. It is interesting to note that the work hardening rate of the NA and UA tempers, where plastic instability was absent, surpassed that of the OA temper where plastic instability was observed after about 3% plastic strain.

4.1.2 Nanoindentation testing

In order to more carefully probe the microstructural influences on the serrated mechanical response and strain rate sensitivities, nanoindentation experiments were carried out; the high-resolution load-displacement capabilities of nanoindentation makes it an effective tool for probing nanoscale perturbations such as plastic instability or strain localization [105]. Fig. 4.4 shows the nanoindentation response of three representative tempers: PA, NA and OA. The tests were conducted at an indentation strain rate of 0.005 s^{-1} . The response observed in the micro-tensile test, specifically the absence of plastic instability in all but the OA temper, was also observed in the nanoindentation tests. As clearly shown in the magnified insert in the figure, the instability manifested here as burst of displacement; the inherently load controlled nature of the nanoindentation tests precludes the formation of load drops during deformation [17,116].

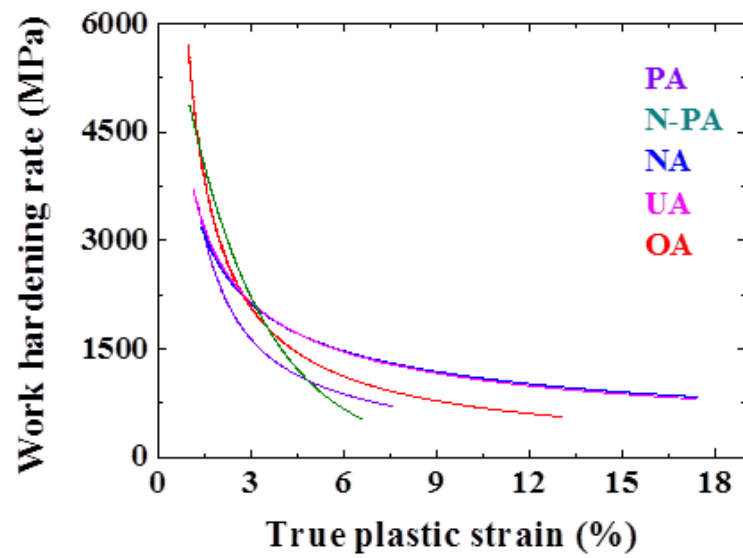


Fig. 4.3: Work hardening rates ($d\sigma_T/d\varepsilon_T$) of each temper plotted as a function of true plastic strain. Colour codes are as previously defined.

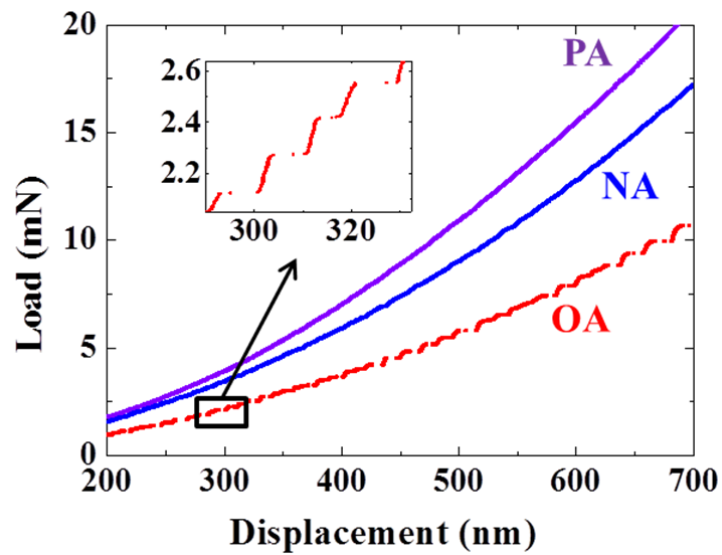


Fig. 4.4: Load–displacement curves of PA, NA and OA tempers. Colour codes are as previously defined.

In order to determine the influence of strain rate on the instability and more specifically, the strain rate sensitivity of the three tempers, nanoindentation based strain rate jump tests were carried out, as already introduced in section 3.4. Fig. 4.5 presents a section of the nanoindentation curve obtained from the strain rate jump test. It shows the load vs. displacement response accompanying the change in nanoindentation strain rate from a very low strain rate of 0.0005 s^{-1} to a high strain rate of 0.05 s^{-1} . In the case of the PA temper, the change from the low to high strain rate regime was accompanied by an upward deviation from the loading path. In contrast, a downward deviation from the loading path was observed in the OA temper upon changing the strain rate from the low to the high regime. On the other hand, the loading path was continuous in the NA temper, except for the transient response that usually accompanies a sudden change in strain rate during deformation.

These trends are more clearly shown in Fig. 4.6 where a portion of the hardness response for the PA, NA and OA tempers is shown. A significant decrease in hardness accompanied the decrease of the strain rate from 0.05 s^{-1} to 0.002 s^{-1} in the PA temper. The hardness was however constant in the case of the NA temper in the different strain rate regimes. The change in hardness of the NA temper that followed the decrease in strain rate was negligibly small, in agreement with the plot in Fig. 4.5. On the other hand, in the case of the OA temper, a similar decrease in strain rate was followed by an increase in hardness. The behaviour of the PA and OA tempers in the strain rate jump test is indicative of positive and negative strain rate sensitivity, respectively, while that of the NA temper is characteristic of a strain rate insensitive material.

The hardness of the three tempers was observed to decrease with increasing indentation depth, a phenomenon commonly referred to as indentation size effect (ISE). The observed ISE was found to be partly due to sink-in, a response associated with materials exhibiting strain hardening which leads to an overestimation of the contact area used in analysing nanoindentation data [86]. While the influence of sink-in can be corrected for by using a formulation of hardness that is independent of the contact area [86], such a correction did not fully remove the decrease in hardness with increasing displacement suggesting that there is an intrinsic ISE present. This of course complicates the analysis of the strain rate sensitivity.

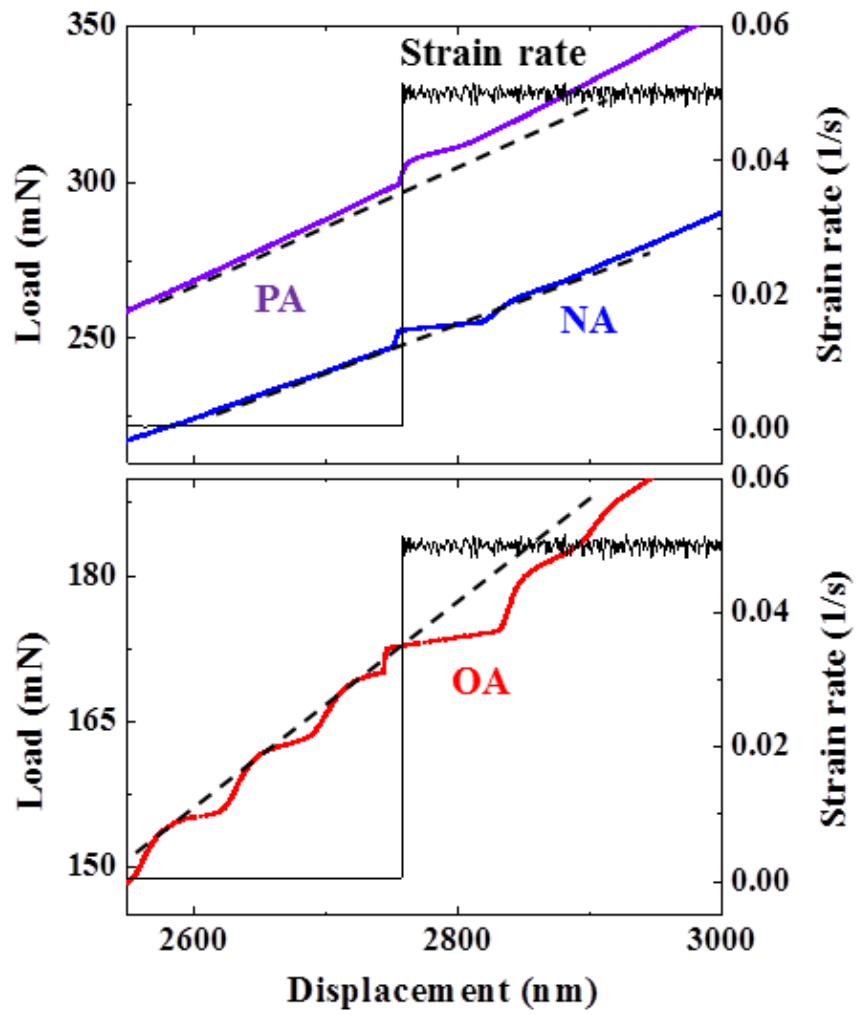


Fig. 4.5: A section of the load vs. displacement response from the strain rate jump tests. The associated imposed strain rate (black line) is included in the plot. The broken line is a guide for the eyes.

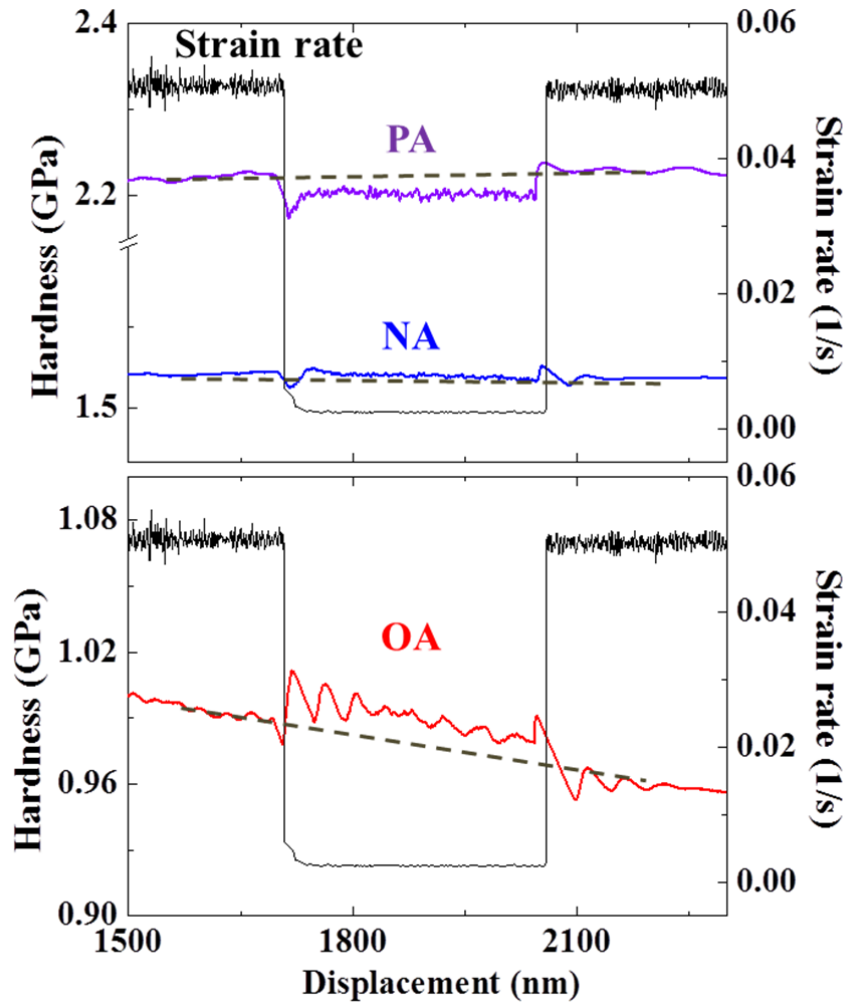


Fig. 4.6: Hardness vs. displacement response of the PA, NA and OA tempers. The imposed strain rate is also included in the plot. The broken lines as before are a guide for the eye. Colour codes are as previously defined.

However, since the load response, shown in Fig. 4.5, is consistent with the trend observed in hardness, Fig. 4.6, it can be argued that the effect of a change in strain rate on the hardness response is not influenced by the ISE.

The strain rate sensitivity parameter (SRS), m , is plotted as function of variation in log of nanoindentation strain rate in Fig. 4.7. The strain rate sensitivity parameter was calculated from the relationship given in equation (3.7). Due to the ISE, the hardness at each strain rate was estimated from the intercept of a line drawn from the steady state hardness response at the given strain rate to the hardness axis. The SRS parameter, m , for the OA temper at all imposed variations of strain rate is in the negative domain of Fig. 4.7. This clearly demonstrates that the observed displacement bursts in the load vs. displacement curve, shown in Fig. 4.4, for the OA temper are associated with plastic instability. In contrast, m is approximately zero for the NA and positive for the PA temper, in agreement with the absence of plastic instability in these tempers.

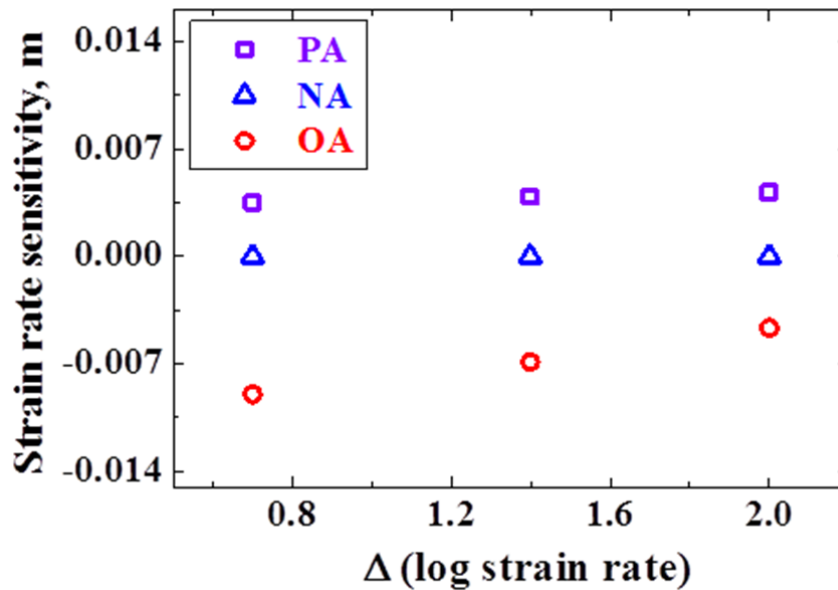


Fig. 4.7: Strain rate sensitivity, m , as a function of the change in strain rate.

4.2 Microstructural constituents

Detailed TEM characterization of the microstructural content in each temper was performed in order to deduce the influence of the precipitates on the underlying microscopic mechanisms and consequently, the observed mechanical response. Differences in interaction between the dislocations and precipitates are expected to have significant influence on the observed macroscopic mechanical response.

Fig. 4.8 shows the size distribution (diameter) of δ' phase in the OA and NA tempers. The distribution is approximately Gaussian in each case. The mean particle size of the δ' phase in each temper is the average diameter of over 180 particles. The volume fraction of the δ' phase was estimated using the relationship prescribed by Cahn and Nutting [107]. This relationship is given in equation (4.1), where f_v and f_A are the volume fraction and area fraction, respectively, d is the average particle diameter, t is the thickness of the TEM lamella and N_v is the number of particles per unit volume. N_v can be estimated from equation (4.2), where N_A is the actual number of particles in a unit area of the lamella. The reported average volume fraction, f_v , is the average of at least three different micrographs.

$$f_v = f_A + \frac{\pi}{4} d^2 N_v t, \quad (4.1)$$

$$N_v = \frac{N_A}{(t + d)}. \quad (4.2)$$

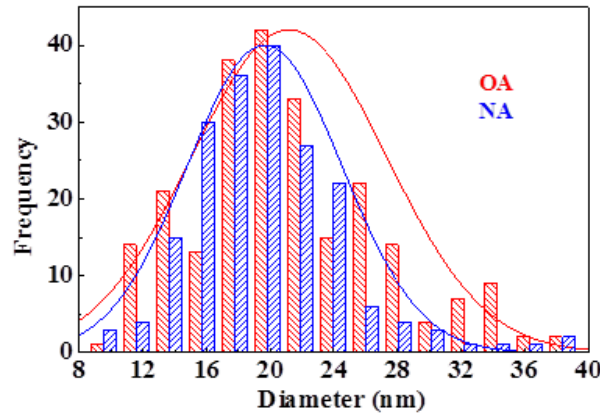


Fig. 4.8: Size distribution of δ' phase in the overaged (OA) and naturally aged (NA) tempers.

4.2.1 Peak aged (PA) temper

Several phases including Ω , δ' , θ' , S' and a high density of T_1 phase are present in the PA temper. This observation is consistent with the view that a combination of these phases leads to significantly high yield strength in this temper [71]. Fig. 4.9(a) and (b) show selected area diffraction patterns (SADP) taken from $\langle 100 \rangle_\alpha$ (Al matrix) and from $\langle 112 \rangle_\alpha$ zone axes in the PA temper. The four variants of the T_1 phase are present in both SADPs, along with superlattice spots from the δ'/β' phase. The diffuse streak-like contrast in the $\langle 100 \rangle_\alpha$ zone axis SADP probably arise from elongated spots associated with the θ' phase [74,78]. The streaks formed along the $\langle 420 \rangle_\alpha$ direction in the $\langle 112 \rangle_\alpha$ SADP confirm the presence of S' phase in the PA temper [92,93]. Also present in the $\langle 112 \rangle_\alpha$ SADP are spots indicating the presence of Ω phase [74]. A dark field image showing one of the variants of the T_1 phase and δ'/β' is shown in Fig. 4.9(c). Two variants of the T_1 phase are also shown in the two beam bright field (2BBF) image in Fig. 4.9(d). The high density of this phase is also apparent from this micrograph. Efforts to image the dislocation structure in the peak aged temper were not successful. The high density of precipitates and their associated strain fields within the matrix completely overwhelmed the dislocation contrast.

4.2.2 Naturally aged (NA) temper

A SADP of the NA temper taken from a $\langle 100 \rangle_\alpha$ zone axis is shown in Fig. 4.10(a). The SAD pattern revealed very faint superlattice spots characteristic of δ'/β' phase. The presence of δ'/β' precipitates is clearly revealed in Fig. 4.10(b), which shows a dark field image obtained from a δ'/β' superlattice spot in an orientation slightly tilted away from a $\langle 110 \rangle_\alpha$ zone axis. The arrows in the figure point to δ' precipitates that have a doughnut shape configuration, an indication that these must have nucleated on the β' phase [74]. Fig. 4.10(c) also shows the δ'/β' precipitates. This dark field image was made from a superlattice spot but with the matrix diffraction spots tilted to a two beam condition. Lines of no contrast, an indication that these precipitates are coherent with the matrix, can be seen in the precipitates in this micrograph. The average radius and volume fraction of the δ'/β' phase in this temper are 10 ± 5 nm and $0.004 \pm 6e-4$ respectively. The low volume fraction of the δ'/β' phase apparently led to the very faint superlattice spots seen in the SAD pattern. Since the superlattice δ'/β' reflections are very faint, it was very difficult to

locate and carry out analysis of them. This may explain why Decreus and co-workers [69] did not observe this phase in the naturally aged temper of the same alloy. Streaks associated with GP zones are absent in the SADP for the NA temper, as indicated in Fig. 4.10(a). The absence of GP zones in the early stages of aging in similar alloys has been attributed to dislocations generated during the stretching treatment prior to natural aging [81,92,108]. It is argued that dislocations act as vacancy sinks, and thus discourage the diffusion of Cu atoms to form GP zones. Kumar and Heubaum [81] also showed that the precipitation of δ' discourages GP zone formation. There was evidence of precipitates in some of the grain boundaries of the NA temper. These are likely equilibrium precipitates or dispersoids that were undissolved during the solution treatment. The absence of reflections arising from such precipitates however suggests that their volume fraction is very low. A two-beam dark field image showing the typical dislocation structure found in the NA temper is shown in Fig. 4.10(d). The dislocations are typically wavy, unevenly arranged, tangled and appear pinned by precipitates at several points along their line length. No evidence of dislocation pairs could be found.

4.2.3 Overaged temper

Fig. 4.11(a) is a $\langle 112 \rangle_\alpha$ zone axis SADP taken from the OA temper. Most of the key microstructural features observed within the grain interior in the OA temper are revealed in the bright field image shown in Fig. 4.11(b). Some of these phases were also observed along the grain boundaries. It was not possible to unambiguously identify all the precipitates seen in this temper. One such example is the precipitate marked “X” in Fig. 4.11(b). A large spherical precipitate with radius in excess of 200 nm identified as T_2 phase is highlighted in the micrograph. SADP taken only from this precipitate (not shown) revealed the icosahedral symmetry that is associated with the T_2 phase. However, the T_2 phase was mostly found along the grain boundaries. A rod-like T_B phase is also highlighted in the matrix. T_B precipitates, equally large in size, were also seen in the grain boundaries. The absence of streaks and reflections associated with the T_1 , θ' and Ω phases in the $\langle 112 \rangle_\alpha$ SAD pattern inserted in Figure 2(e) indicate that these phases, which are likely to have formed during the early stages of aging at 370 °C have dissolved, facilitating the precipitation of more equilibrium phases such as T_B phase. Time–Temperature–Transformation (TTT) diagrams proposed for a similar alloy AA2195 [84] strongly suggest that the T_1 and

θ' phases precipitate in less than 60s at temperatures around 204 °C and 370 °C, respectively. Faint superlattice spots indicative of the presence of the δ'/β' phase are still evident in the SADP. A dark field image made with one of these spots is shown in Fig. 4.11(c).

The average radius and average volume fraction of the δ' precipitates in this phase are 11 ± 6 nm and 0.006 ± 0.002 respectively; these values are only slightly higher than those found in the naturally aged temper. Fig. 4.11(d) shows the typical dislocation configuration found in the overaged temper. The dislocations are mostly arranged in planar arrays and uniformly distributed on individual planes. It is also evident from the micrograph that the dislocations are pinned at several points around their line lengths by the δ'/β' precipitates as well as by the large precipitates. Evidence of coherent δ' precipitates showing lines of no contrast perpendicular to the g -vector can also be seen in the matrix. In addition, long single dislocations extending from one large precipitate to another were often seen in the micrographs.

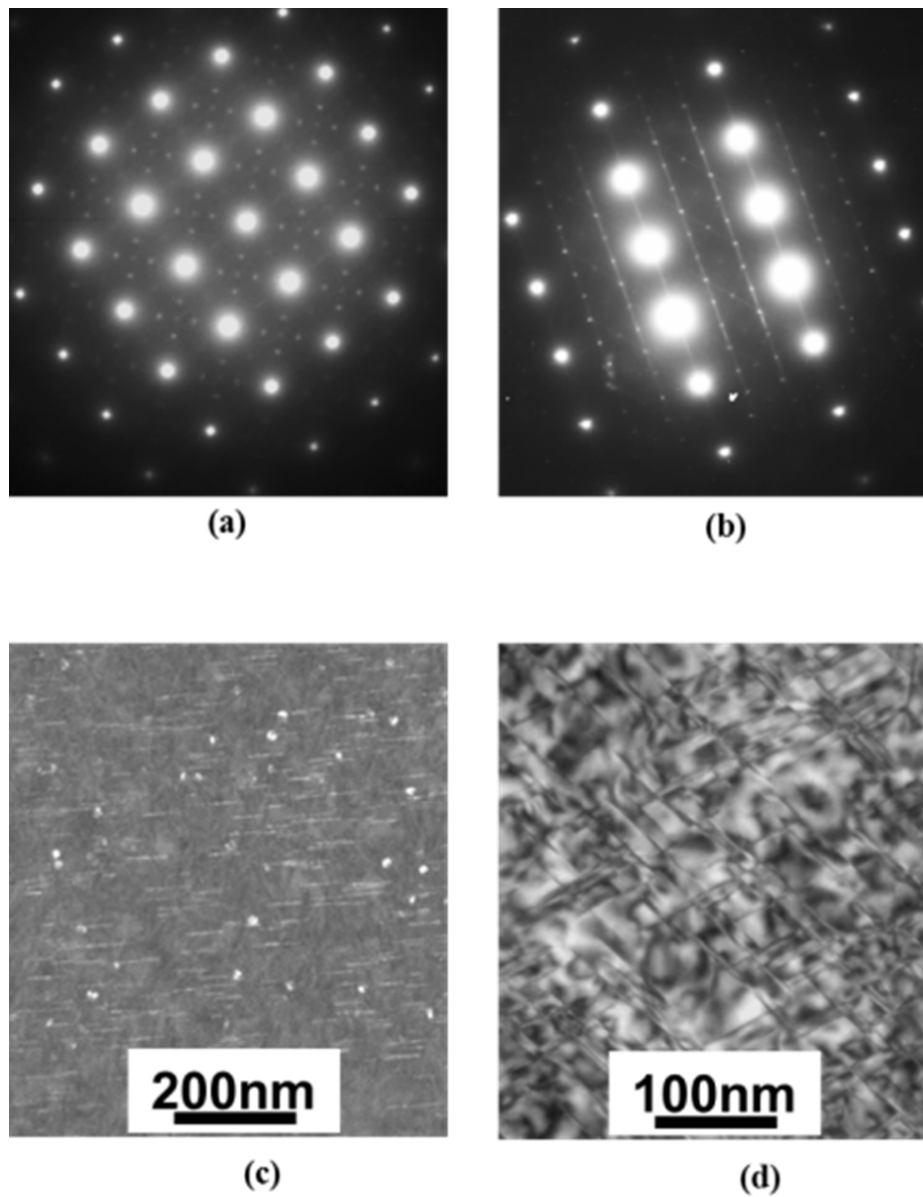


Fig. 4.9: Selected area diffraction patterns (SADP) of the PA temper taken along (a) $\langle 100 \rangle_\alpha$ zone axis and (b) $\langle 112 \rangle_\alpha$ zone axis. Schematics of these SADPs and the phases represented by the spots and streaks are shown in Fig. 3.6. A dark field image showing one variant of T_1 phase and δ'/β' is shown in (c). The micrograph in (d) is a two beam bright field image (2BBF) image showing two variants of the T_1 phase.

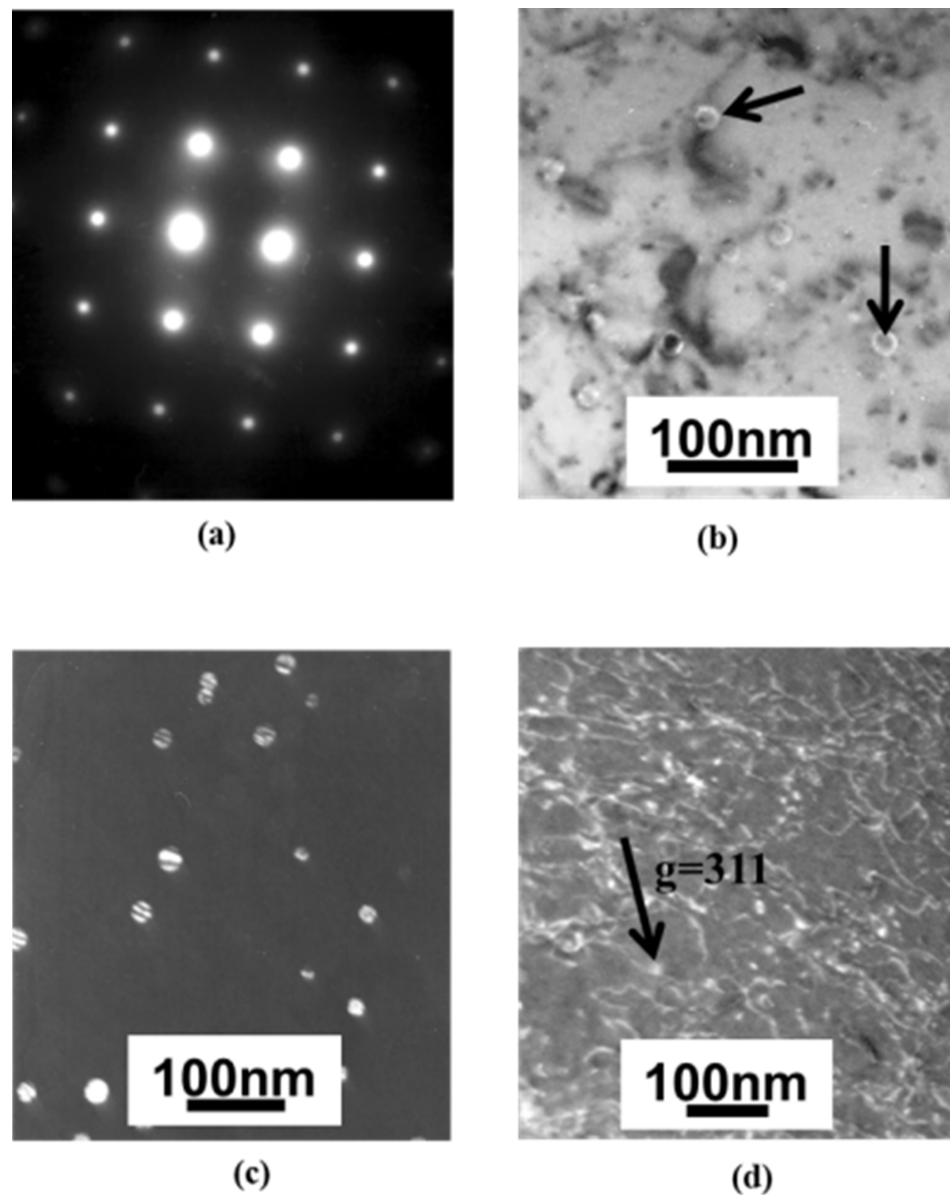


Fig. 4.10: TEM micrographs from the naturally aged (NA) temper. (a) $\langle 100 \rangle_{\alpha}$ zone axis SADP showing superlattice spots from δ'/β' precipitates. (b) A dark field (DF) image showing the δ'/β' composite phase. The donut morphology of these precipitates is indicative of the precipitation of δ' on the β' phase. (c) Another dark field image of the δ'/β' phase made from a superlattice spot but with the matrix diffraction spots tilted to a two beam condition. (d) Typical dislocation structure in this temper.

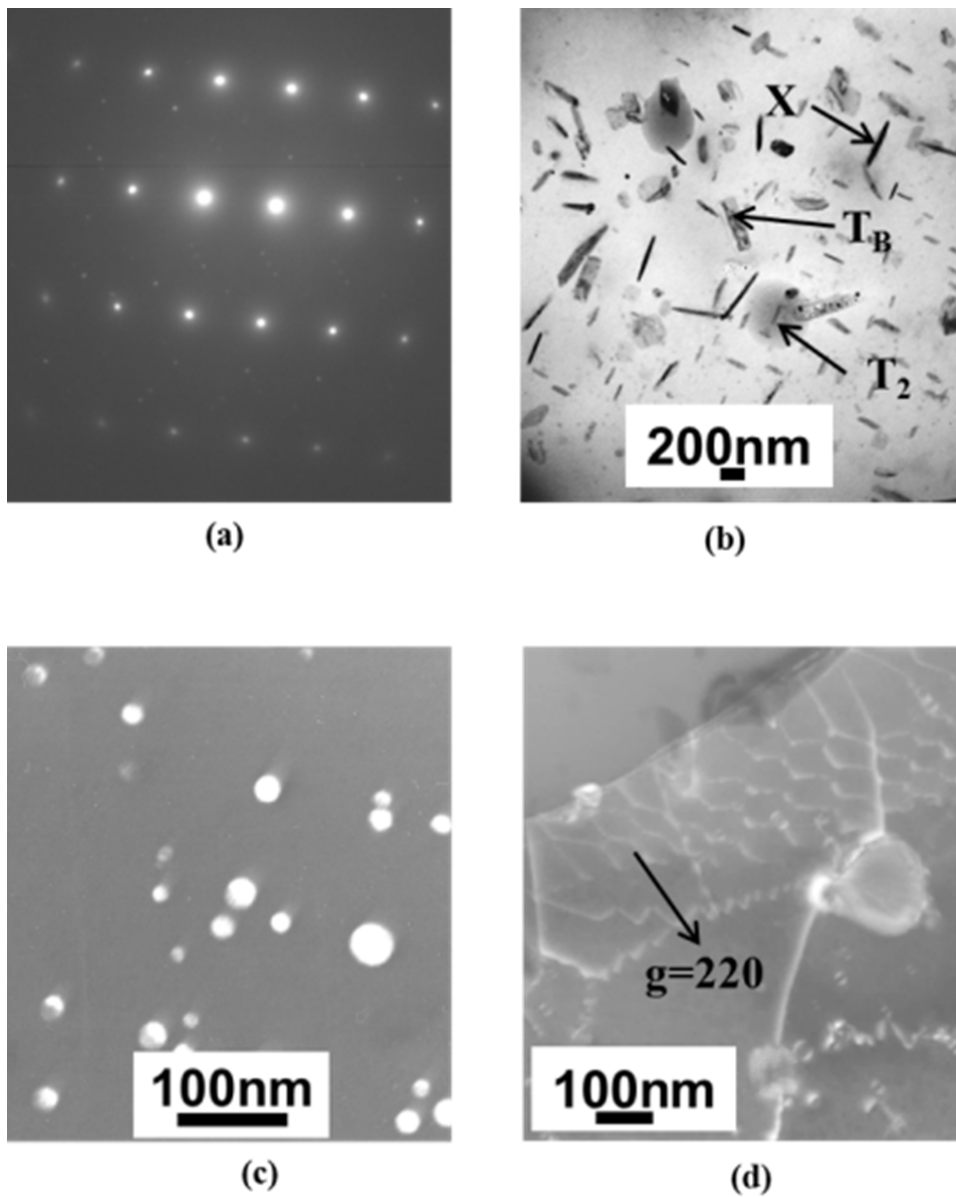


Fig. 4.11: TEM micrographs from the overaged (OA) temper. (a) $\langle 112 \rangle_\alpha$ zone axis SAD pattern, showing no evidence of S' , T_1 or Ω phases. Spots arising from δ'/β' and T_B phase are present. (b) A bright field image clearly shows the T_B and T_2 precipitates, as indicated by the arrows. (c) A dark field image shows δ'/β' precipitates. (d) A typical dislocation structure in this temper.

4.3 High energy x-ray diffraction (HEXRD)

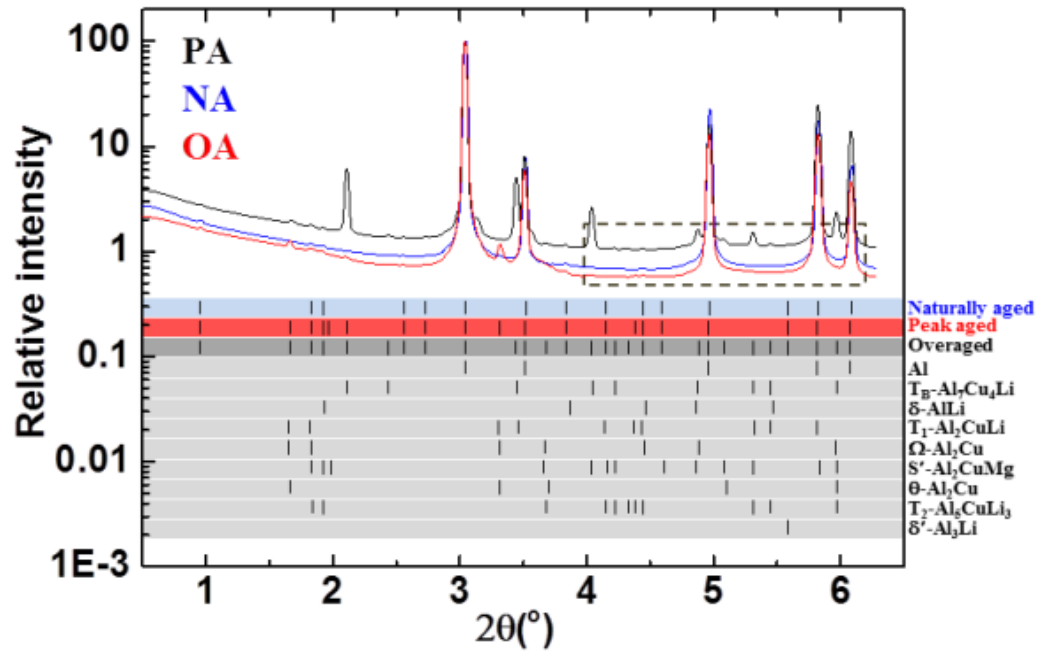
Complimentary characterization of the precipitates present in each of the tempers was carried out with high energy x-ray diffraction (HEXRD). The difficulty in identifying some of the precipitates observed in the TEM analysis, particularly in the OA temper, partly necessitated the use of this method.

The full ranges of the recorded HEXRD spectra for the PA, NA and OA tempers are shown in Fig. 4.12(a). Simulated 2θ positions of peaks present in the different phases known to occur in this alloy are also included in the figure. An enlarged image of the highlighted region of the diagram is given in Fig. 4.12(b). In order to reduce the amount of plotted data, only simulated peak positions that are within ± 0.02 degrees of the experimental peaks are shown. Simulated peak positions of phases that coincide with the Al peak positions were also excluded. Examination of the data shows that there is a lot of overlap between the different phases because of their closely related crystallographic parameters, indexing a phase correctly therefore required comparison with the TEM results. Some weak peaks which were present in all three tempers at $2\theta = 0.95, 1.83, 2.56$ and 2.73 could not be indexed with the simulated patterns of the known phases used in this study.

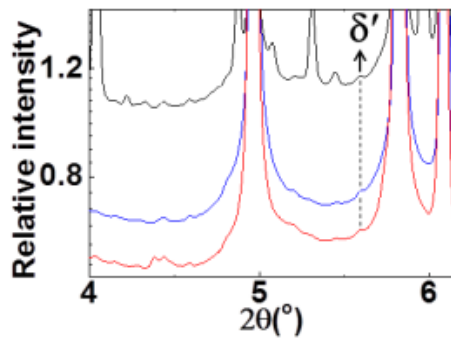
The prominent peaks at $2\theta \approx 3.04, 3.51, 4.96, 5.82,$ and 6.08 degrees for the three tempers were indexed as the Al phase. All the 2θ positions of the Al peaks in the NA sample are however shifted to slightly larger 2θ values in comparison to the peak positions in the PA, OA and simulated Al patterns. The Al phase of the simulated diffraction pattern and that of the OA and PA tempers all have a lattice parameter of 4.05\AA , while that of the NA is 4.04\AA . The uniform shifts in 2θ peak positions of the NA temper, and the corresponding decrease in lattice parameter, relative to those of the OA and PA, are likely associated with the higher Li and Cu solute content in the NA temper. The APT analysis (see section Fig. 4.5) shows that the matrix solute content of Li and Cu is higher in the NA temper, while the Mg content is the same in both NA and OA tempers. It has been shown that the lattice parameter of Al decreases with increasing Li, Cu, Si and Zn content, while it increases with increasing Mg content [109]. Macroscopic residual stresses arising from the 2% pre-stretch given to the NA temper prior to aging may additionally contribute to the observed decrease in lattice parameter [110]. The decrease in matrix solute concentra-

tion due to precipitation of new phases in addition to the relief of residual stresses during aging at high temperature will lead to an increase in the lattice parameter of the artificially aged tempers, i.e. the OA and PA. Enlarged portions of two of the Al peak positions are shown for all three tempers in Fig. 4.12(c).

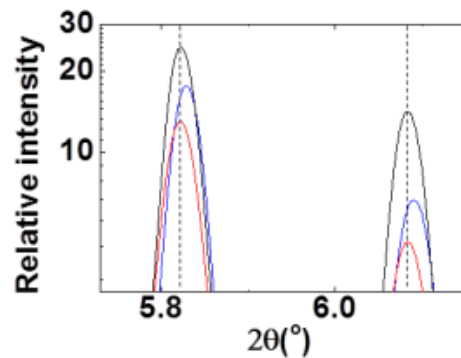
The weak peak intensities shown by an arrow in Fig. 4.12(b) at $2\theta \approx 5.58$ corresponds to the δ' phase. This result further confirms that the δ' phase is present in all the examined tempers. The other simulated δ' 2θ positions coincide with the five Al peak positions and were therefore excluded from the analysis. Only two of the simulated β' 2θ positions coincide with the experimental data, and since they too coincided with the Al peaks were not analysed. Consequently, the presence of β' could neither be confirmed nor excluded. Weak peak intensities corresponding to the T_2 phase are present in all three tempers even though TEM analysis could only confirm its presence for the OA temper. Peaks belonging to the T_B phase are present in both the PA and OA tempers, though the peak intensities are significantly higher in the latter. This implies that the volume fraction of this phase is significantly higher in the OA temper in comparison to the PA temper. Peaks arising from the equilibrium δ and θ phases were also detected in the OA temper. It is likely that some of the unidentified precipitates in the TEM micrograph of the OA temper are these equilibrium phases. Peaks associated with θ , S' , Ω and T_1 phases can be found in the spectra of the PA temper, consistent with the TEM analysis. Since these peaks largely overlap each other, it is difficult to unambiguously distinguish between them with this method. No other phases seem to be present in the NA temper.



(a)



(b)



(c)

Fig. 4.12: HEXRD spectra for the three temps. (a) The full spectra, including the 2θ positions of the experimental and simulated phases. (b) An enlarged section of the spectra showing some of the weak peaks. A 2θ position of δ' phase that did not coincide with the Al peak positions is shown by an arrow in the figure (c) Two prominent experimental Al peaks showing slight shift of the Al peak associated with the NA.

4.4 *In situ* tensile straining in the TEM

In order to more directly correlate the mechanical response to microstructural influences, *in situ* tensile testing within the TEM was carried out. More details about the test were presented in section 3.5.3. A series of still images taken from individual video frames that were recorded during the *in situ* TEM straining of the OA temper are shown in Fig. 4.13. The corresponding video is included as supplementary material, see appendix. Close examination of the video frame taken at 0s shows strong similarities to that observed in the TEM micrograph shown in Fig. 4.11(d). Large rod-like precipitates can be seen lying in the mid-upper region of this still image in addition to several white spots arising from the presence of the δ' precipitates. The large precipitates, which are typically T_2 and T_B , have Orowan loops around them. Dislocation activity occurred in bursts, in part due to the incremental loading protocol associated with the straining holder. Most remarkably, the dislocations appeared in pairs in almost all instances of observed dislocation activity in the OA temper. The dislocations belonging to each pair tended to glide simultaneously until they were held up by obstacles along their path. 7 such pairs of dislocations are shown in Fig. 4.13.

With the exception of pairs 3 and 5, the dislocations belonging to each pair were approximately 200 nm apart, an indication of weak coupling between the dislocations that form a pair. It can be argued that the dislocation pairs are not Shockley partial dislocations, but rather pairs of perfect dislocations since the high stacking fault energy of Al prohibits the formation of partial dislocations with pair spacing as wide as observed in this temper [43,49]. Rosner [111] also observed a similar trend in Al–Li binary alloys during *in situ* straining in the TEM. They attributed the weak coupling to a low volume fraction of the δ' phase; a higher volume fraction of the δ' phase would lead to stronger coupling of dislocation pairs.

Cross slipping of some of the dislocations belonging to a pair was evident in the OA temper. Typical examples are the trailing dislocation in pairs 1, 3 and 5. In the case of pair 1, cross slip of the trailing dislocation occurred at about 18 secs. Careful evaluation of the video at this point shows that this dislocation cross slipped in the direction indicated by the red arrow. In the case of pairs 3 and 5, the two trailing dislocations belonging to each

of these pairs clearly lie on different slip planes, as indicated by the difference in the glide directions of the leading and the trailing dislocations. It is not clear if these dislocations later return to the same glide plane. It is also evident from Fig. 4.13 that the dislocations are relatively straight and that both dislocations that form a pair are pinned at several points along their line length by precipitates.

The typical dislocation configuration around the equilibrium precipitates in the OA temper in the undeformed state is shown in the BF image in Fig. 4.14(a). Little or no Orowan loops can be seen around the precipitates in the state. In contrast, several loopings and dislocation debris were formed around these precipitates after *in situ* TEM straining in the TEM. These are clearly revealed in the BF image and corresponding DF image shown in Fig. 4.14(b) and (c). The observed increase in Orowan loopings and dislocation debris around these precipitates after deformation strongly supports the assumption made in section 4.1 that the high work hardening rate observed in the OA temper is associated with the back-stress exerted by the Orowan loops.

It was not possible to record very distinct dislocation activity during the *in situ* TEM tensile straining of the NA temper due to the high density of dislocations initially present. The dislocations only moved very short distances before stopping as a consequence of the high dislocation density. The movements were however not localized as in the case of the OA temper. The post-strain micrographs of the OA and NA tempers are shown in Fig. 4.15(a) and (b). It is evident from these micrographs that slip is planar and localized in the OA, while it appears to be homogeneous in the NA temper. The difference in the dislocation structure indicates the operation of a dislocation-obstacle interaction mechanism different from that operating in the OA temper. *In situ* TEM straining was also not carried out on the PA temper since the image contrast associated with the dislocation structure was overwhelmed by the stress fields of precipitates.

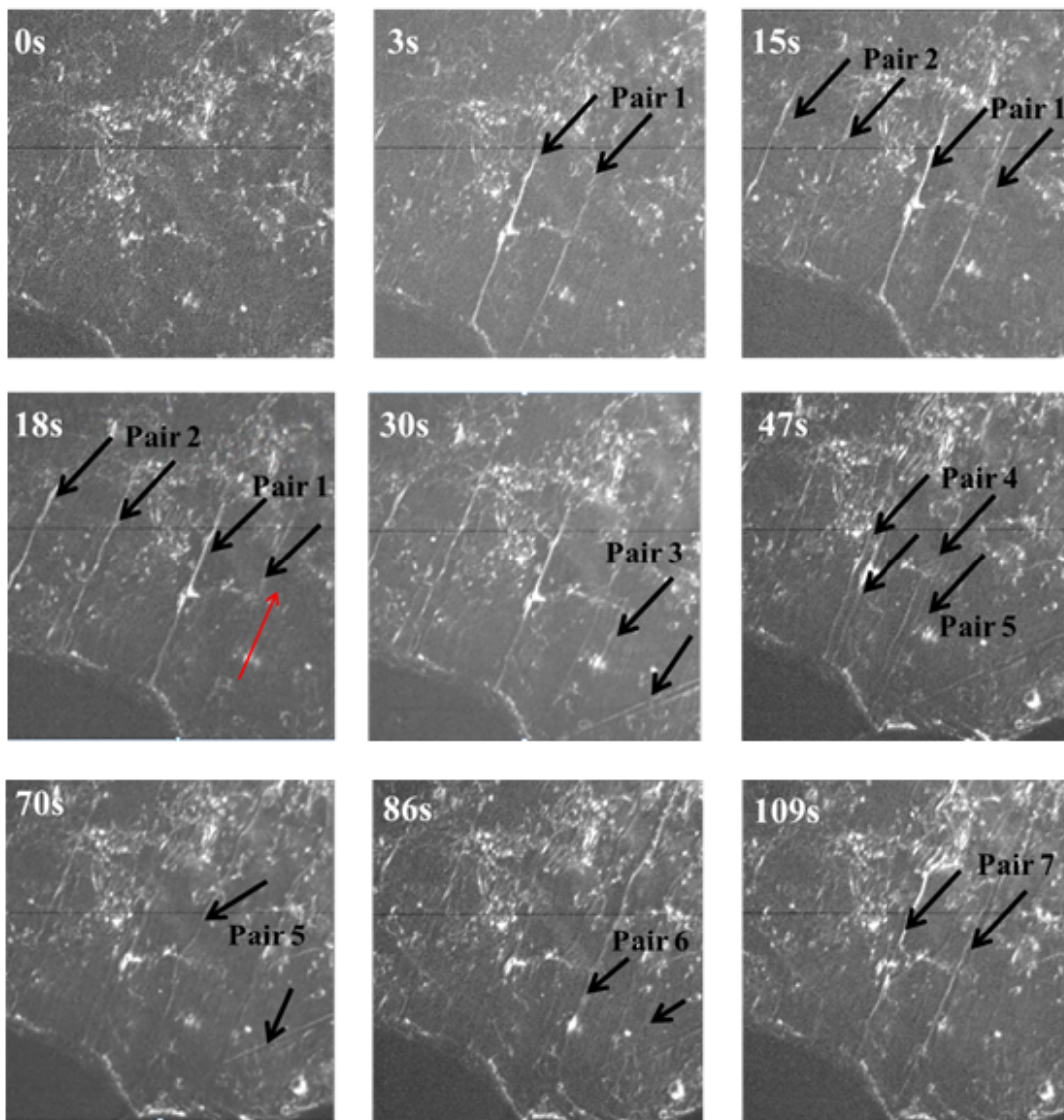


Fig. 4.13: Series of still images taken from video frames recorded during *in situ* TEM tensile straining of the overaged sample. The black arrows show dislocations that glide concurrently. The red arrow shows the glide direction of the trailing dislocation in pair 1.

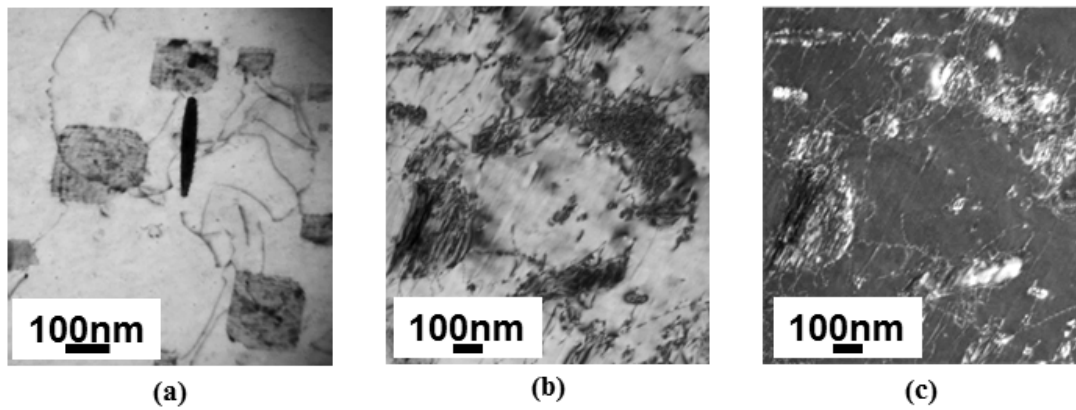


Fig. 4.14: TEM micrographs of the OA temper showing, (a) a BF image of the equilibrium precipitates in an undeformed sample (b) BF image of equilibrium precipitates after *in situ* TEM straining of a lamella. (c) Corresponding DF image of (b). The pre- and post-deformation images were not taken from the same sample.

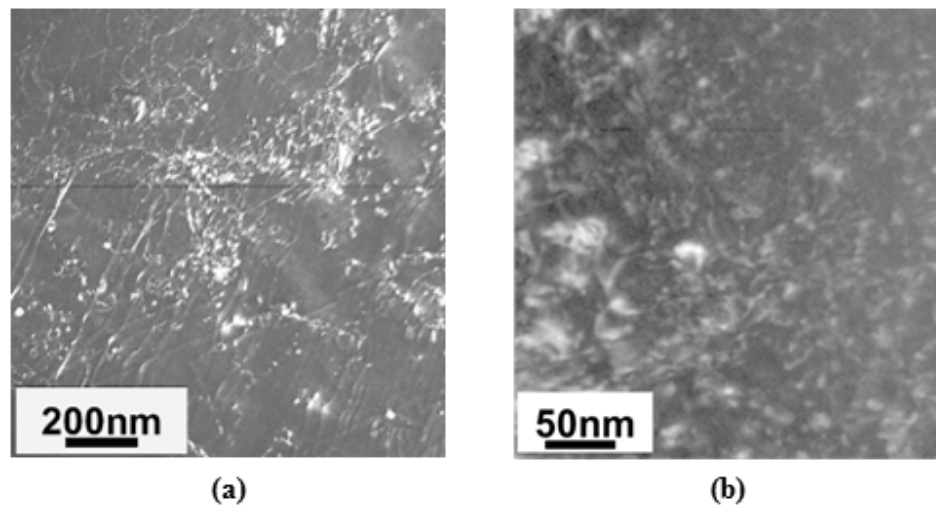


Fig. 4.15: TEM micrograph taken with the straining holder after the *in situ* TEM tensile straining test of (a) The overaged temper (OA). Slip is mostly planar after deformation, as was the case in the pre-deformed sample. (b) The Naturally aged temper (NA).

4.5 Atom probe tomography of the PA, NA and OA tempers

Quantitative elemental analysis of the matrix phase and the clustering therein was achieved with atom probe tomography (APT). A brief description of the method, including the cluster identification technique employed in this work was presented in section 3.7.

The overall concentration of the major alloying elements in the PA, NA and OA tempers obtained from the APT measurements is given in Table 4.1. Over 4 million atoms were captured in each test. Atoms of Zr were not detected in the measurements, probably because the presence of Zr^{2+} peaks in the “thermal tail” of the main Al peak complicates the accurate detection of the Zr atoms. Si was overestimated in all three samples, as explained in section 3.7. Regardless, the experimental concentrations of the main alloying elements, i.e. Li, Cu and Mg, are comparable with the nominal concentration and can therefore be taken as a good indication of the global matrix concentration of this temper after ageing. The concentrations of Li, Cu and Mg in the PA temper are nevertheless lower than those of the other investigated tempers. In particular, the Li, Cu and Mg concentrations in the PA temper show a decrease of ~48%, ~65%, and ~54%, respectively, in comparison to the concentration of these elements in the NA temper; the concentration of the latter being the point of reference. This remarkable decrease in concentration is largely associated with the high density of T_1 precipitate in the PA temper. The micrographs in Fig. 4.9 qualitatively indicate that there is a high density of this phase in this temper. Other precipitates including Ω , θ' and the S_1 phase, which has Mg as one of its constituents, are also present in the PA temper and will additionally lead to a reduction in the matrix concentration. Similarly, a significant decrease in the Cu concentration in the OA temper relative to that of the NA temper was recorded. This large decrease, of about 64%, is associated with the formation of the high volume fraction of large equilibrium Cu-rich phases, such as T_B , in the overaged state. The high peak intensity of the T_B phase as seen in the HEXRD spectra shown in Fig. 4.12, is a clear indication that its volume fraction is high in the OA temper. In contrast to the large decrease in Li concentration (~48%) observed in the PA temper, the concentration of Li in the OA decreased by only ~3% relative to the NA temper. A larger decrease in the Li concentration in the OA temper in comparison to that in the NA temper was expected given the large T_B peaks observed in the HEXRD spectra (Fig. 4.12) of the former. Although the T_B phase is clearly present in reasonable amounts,

it is not expected to lead to a significant depletion of Li considering that the percentage of Li in T_B (Al_7Cu_4Li) is only 1.54%. It can therefore be argued that the results are very reasonable. The Mg concentration in the OA temper in comparison to that in the NA temper remained unchanged, suggesting that all the Mg containing precipitates, S_1 in particular, dissolved into the matrix. This observation is consistent with the TEM and HEXRD results which show that the S_1 phase is absent from the OA temper.

Table 4.1: Overall matrix concentration of the PA, NA and OA tempers as measured from APT experiments. The concentration range given by the manufacturer is also shown.

Element at.%	Li	Cu	Mg	Ag	Si
Nominal	3.11 – 4.27	1.23 – 1.48	0.29 – 0.80	0.03 – 0.12	0.08
PA	1.67	0.38	0.12	0.05	0.20
NA	3.24	1.10	0.26	0.15	0.28
OA	3.14	0.40	0.26	0.04	0.18

Fig. 4.16 shows 10 nm thick slices through reconstructed APT dataset measured from the PA, NA and OA tempers. Data obtained for the main solute elements, Li, Cu and Mg are shown separately. There are large grain boundaries as well as compositional variations in the tip made from the PA temper. Consequently, further analysis was not conducted on the PA temper since these microstructural variations complicate the analysis. Except for a Cu-rich precipitate at the very top of the NA specimen, no other precipitates were captured in the tips examined. The inability to capture the main precipitate phase, i.e. δ'/β' phase, which was observed in both the TEM and HEXRD investigation can be attributed to the relatively low volume fraction and large inter-particle spacing (≈ 78 nm) of this phase in the investigated tempers, relative to the typical size of an APT dataset. A proxigram, i.e., a concentration profile created using the interface of the Cu-rich phase (Fig. 4.17) at the top of the NA specimen, indicate that it is most likely an equilibrium θ precipitate. This precipitate, like the T_2 , must have been undissolved in the solution treating step.

The elemental distribution of atoms in both NA and OA tempers, as shown in Fig. 4.16, seems to be homogenous and there is no visible evidence of clustering of any of the elements. However as earlier stated in section 3.7, a good indication of solute clustering is nevertheless obtained by the use of cluster identification algorithms [98]. In preparation for the clustering analysis employed in this work, regions not belonging to the matrix phase were removed from the datasets. This included the Cu-rich precipitate from the NA temper sample and a crystallographic pole (an APT measurement artefact) to which Cu

atoms segregated slightly from the OA temper sample. Cluster analysis was not carried out for the PA temper. 5th nearest neighbour distribution (5NN) frequency histograms of the main alloying elements, namely, Li–Li, Cu–Cu, Mg–Mg and Cu–Mg in the NA and OA tempers and their respective randomised distributions are presented in Fig. 4.18. Evidence of clustering, indicated by the broadening and shifting of the distribution maxima of the experimental 5NN histogram, relative to the randomized 5NN histogram, to smaller distances [98,100,101], can mainly be seen between the Cu–Cu atoms in the NA and OA tempers. A slight shift of the distribution maxima can also be observed between the experimental and random 5NN histograms of the Li–Li atoms in both tempers. Further cluster analyses were achieved with the core–linkage (CL) cluster algorithm, which is a more accurate and efficient cluster identification technique. The main features of the CL technique were presented in section 3.7. Following the approach of Marceau [102], d_{core} , which is one of the parameters that define the CL algorithm, was set to the distance at which the difference between the cumulative 5NN distance and its randomized counterpart was the highest. The analysis yields $d_{\text{core}}=1.58$ nm and 2.35 nm for Cu–Cu atoms in the NA and OA tempers, respectively, and $d_{\text{core}}=1.1$ nm for Li–Li atoms in both the NA and OA tempers. The second parameter for the CL algorithm, d_{link} , was set to $\frac{1}{2} d_{\text{core}}$ in each case. Only clusters consisting of at least 3 atoms were considered. The random data was generated from the experimental data; only the chemical identities of the atoms were randomized, their spatial positions were unchanged.

The size distribution of the Cu–Cu clusters and the Li–Li clusters determined by the CL technique is plotted as a function of cluster size in Fig. 4.19 for both the NA and the OA tempers. Significant shift between the experimental and the randomized datasets is only observed in the Cu–Cu cluster size distributions of the NA temper. Very little shift can be observed between these datasets in the case of the OA temper, while there is no shift between the Li–Li experimental and randomized datasets of the NA temper.

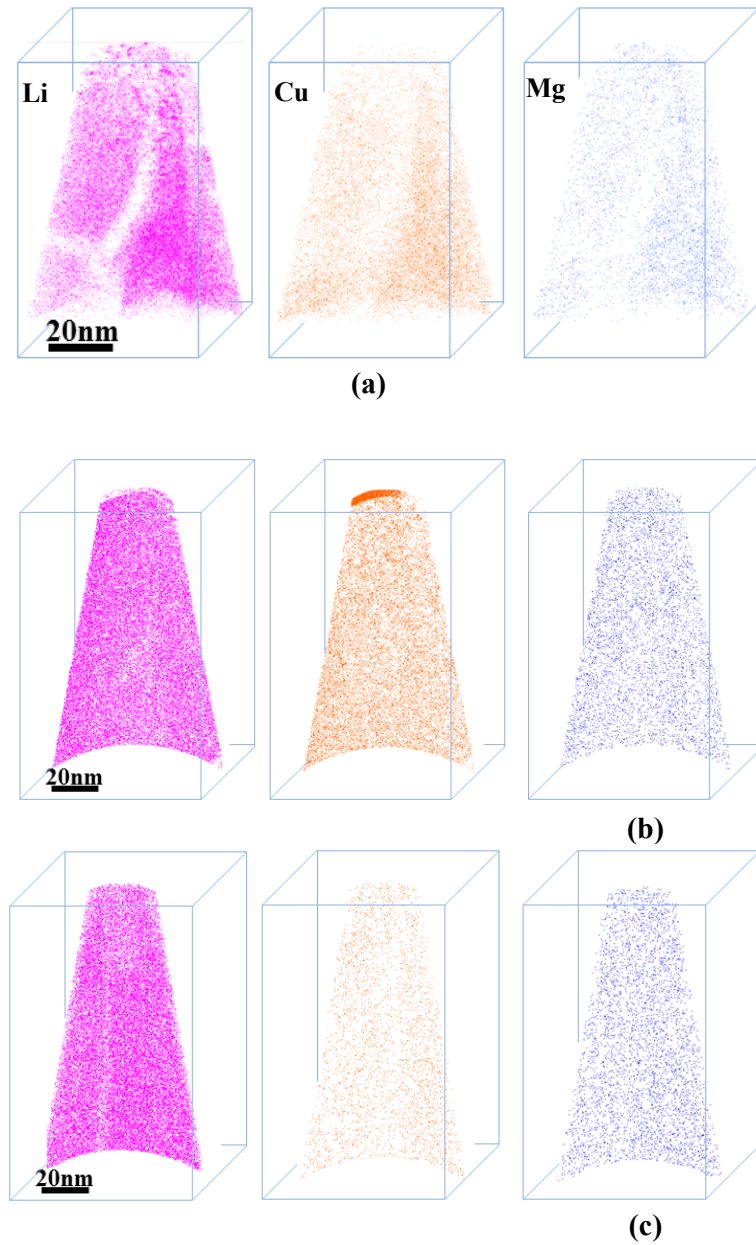


Fig. 4.16: Three dimensional atom probe tomography maps of Li (pink), Cu (orange), and Mg (blue) atoms in the (a) peak aged (PA), (b) naturally aged (NA) and (c) overaged (OA) tempers. With the exception of a Cu-rich phase at the tip of the NA temper, no precipitate was visible in all the measurements. More so, all the atoms in the NA and OA tempers appear to be homogeneously distributed, with no indication of clustering.

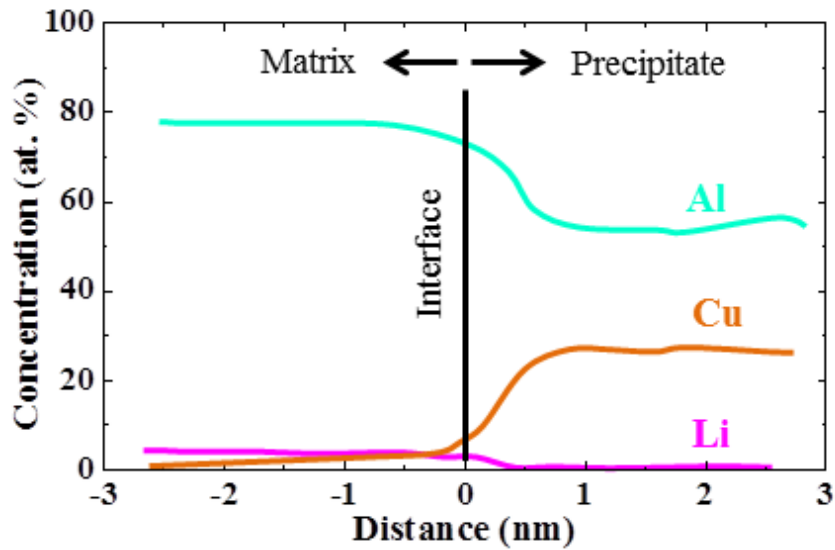


Fig. 4.17: A proxigram created using the interface of the Cu-rich precipitate at the top of the NA specimen. Concentration profiles of the Al (in teal), Cu (in orange) and Li (in pink) atoms are shown.

The Li-Li dataset of the OA temper is similar to that of the NA temper. Further analysis of this plot shows that the “effective” clustering of Cu-Cu atoms, i.e. clustering in the experimental data less than in the random data, in the OA temper is over six times less than that of the NA temper. This is a strong indication that the contribution of these clusters to strength in the OA temper will be significantly less than provided by the clusters in the NA temper. Together these results are a strong indication that the contribution of the clusters to strength will only be significant in the NA temper.

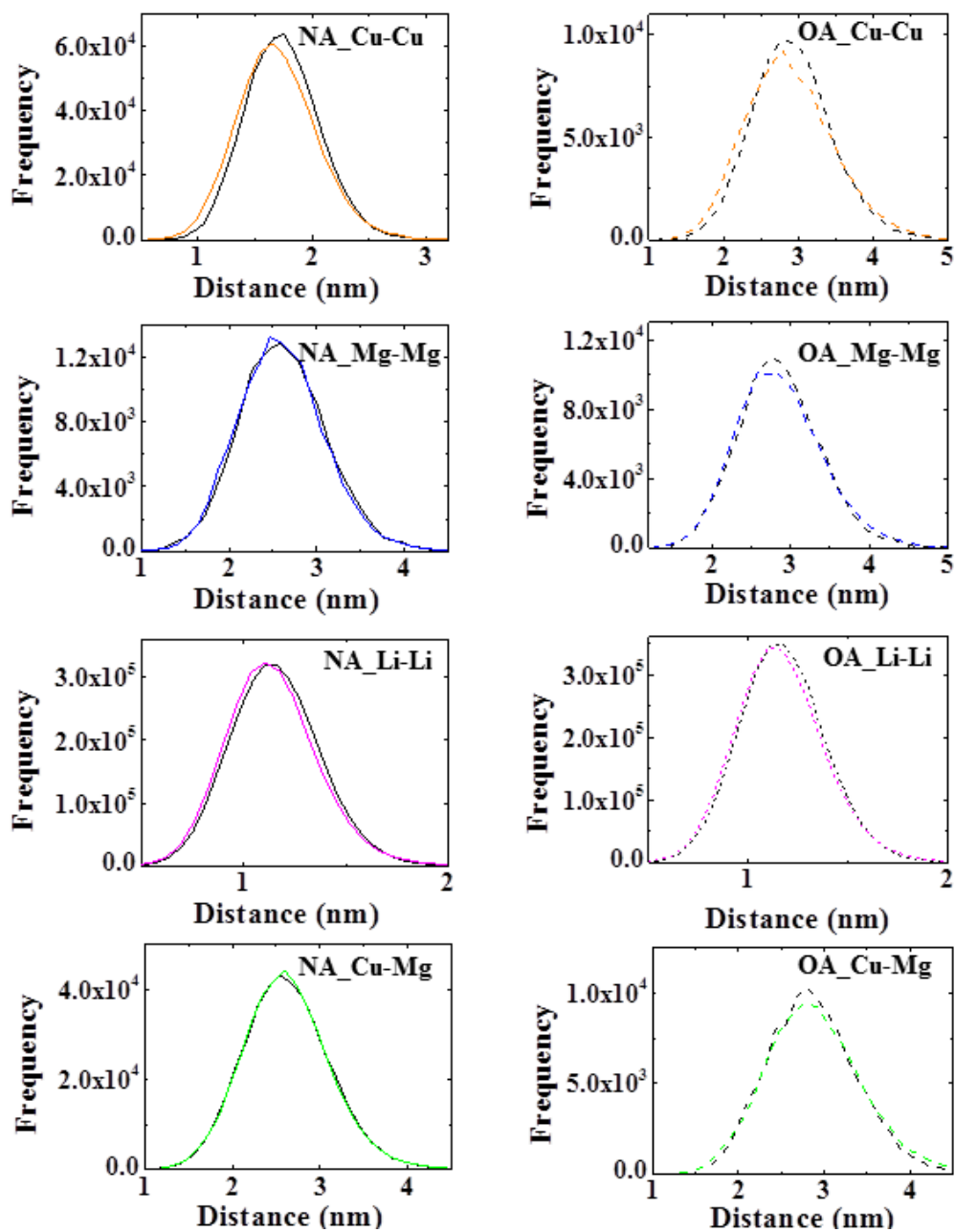
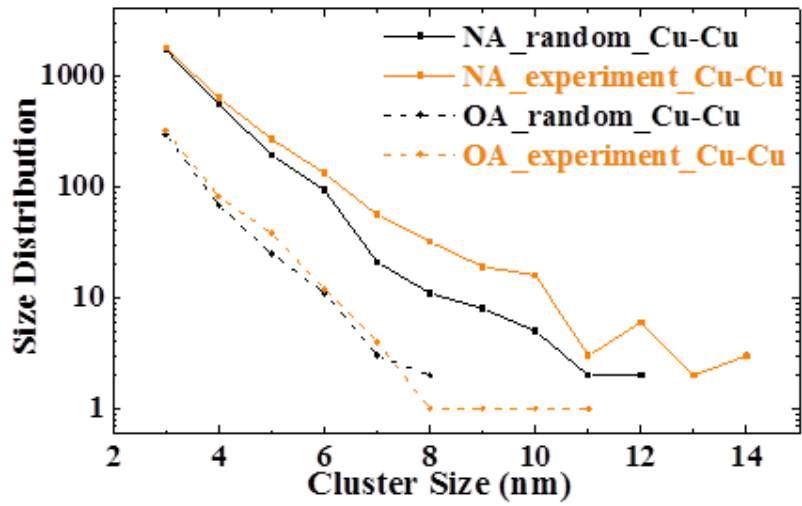
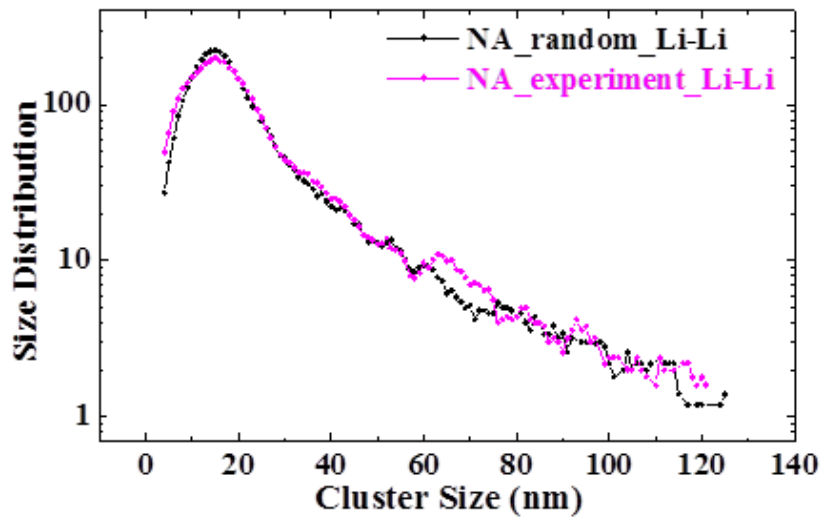


Fig. 4.18: Frequency histograms of 5th nearest neighbour distances (5NN) between atoms of the naturally aged, NA, (straight lines) and overaged, OA, (broken lines) temper. The distribution of the main atomic species, Li-Li (pink), Cu-Cu (orange), Mg-Mg (blue), Cu-Mg (green) and their respective randomised distribution (black) are presented.



(a)



(b)

Fig. 4.19: The experimental size distribution of the (a) Cu–Cu clusters in the naturally aged temper, NA, (orange line), and the overaged temper, OA, (broken orange line). (b) Li–Li clusters in the NA temper (pink line). The respective randomized distribution for the NA temper (black line) and the OA temper (broken black line) is also included in the plot.

5 Microstructural influences on strengthening mechanisms in AA2198

The results presented in the last chapter highlight the wide range of precipitates that form in AA2198 and the mechanical properties of different tempers of this alloy and, more specifically in the case of *in situ* tests, dislocation activity under load. Here, the observed microstructural constituents are correlated to the observed mechanical behaviour. The main focus is on the mechanisms that govern strength in the PA, NA and OA tempers.

5.1 Strengthening mechanisms in the peak aged temper

The high density of the T_1 phase in the PA temper, in addition to the presence of other strengthening precipitates including S' , Ω and δ'/β' phases, supports the view that a combination of these phases leads to significantly high yield strength in this temper. The bulk of the strength in the peak age state is however associated with the T_1 phase. This phase is known to additionally reduce the tendency for strain localization, which is a major problem in these alloys [58,69,78]. Although efforts to reveal the dislocation configuration in this temper were not successful, it has been recently shown that the shearing of the T_1 phase occurs by single shearing events [58,115] and so does not lead to strain localization. Dorin et al. [115] in their work on AA2198 show high resolution high angle annular dark field scanning transmission electron microscope (HAADF-STEM) images of sheared T_1 precipitates with single steps. One such image is shown in Fig. 5.1. It is argued that strengthening by the T_1 phase mainly arises from the energy required to create new interfaces at the boundary between the T_1 phase and the matrix [116]. The energy associated with the creation of the new interfaces, i.e. the precipitate-matrix interfacial energy, is known to be particularly high in the presence of semi-coherent precipitates such as the T_1 phase because of the high lattice strains at the precipitate-matrix interface [43]. More so,

unlike in coherent precipitates which are susceptible to multiple shearing along active glide planes, multiple shearing along an already sheared plane is prohibited in semi-coherent precipitates like the T_1 phase because the interfacial energy required for the creation of new interfaces increases with multiple shearing events [116].

A theoretical calculation of the strengthening in this temper was not carried out because of the complex nature of the precipitate phases, such as T_1 , S' and Ω , present in it. These phases consist of several variants which lie non-uniformly in different crystal planes [74]. This complicates an estimation of their volume fraction, an important parameter in precipitation strengthening models.

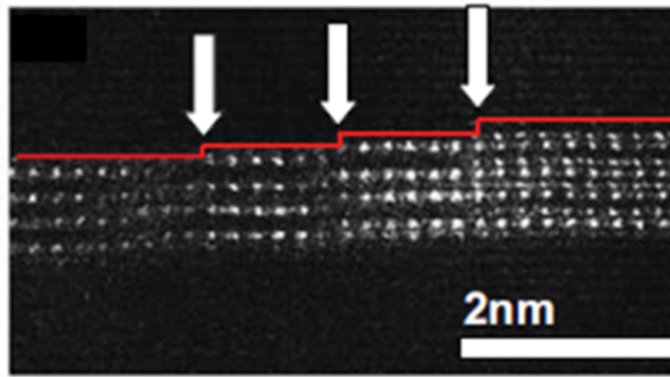


Fig. 5.1: High angle annular dark field – scanning transmission electron microscope (HAADF–STEM) image of a sheared T_1 phase in a 2% plastically deformed AA2198 sample. (Taken from [115]).

5.2 Strengthening mechanisms in the naturally aged temper

The only visible matrix precipitate present in the naturally aged (NA) temper as revealed by TEM investigation is the δ'/β' phase. This phase is clearly revealed in the bright– and dark–field– micrographs shown in Fig. 4.10. Both the δ' phase and the β' phase are long–range ordered [117], and should contribute to order hardening in this temper. The critical resolved shear stress (CRSS) due to order hardening, τ^{OH} , can be estimated from equation (2.18). Since it was not possible in this work to clearly distinguish between the δ'/β' precipitates, τ^{OH} was estimated with the well–known order hardening parameters for δ' . This approach is considered to be reasonable even in the case of δ'/β' core–shell precipitates since the core–shell interface has been shown to be coherent, with

the atomic planes bending only slightly across the interface [117]. Using the Taylor factor of 2.95 [77], $G = 30 \text{ GNm}^{-2}$ [44], $b = 0.2864 \text{ nm}$ [44], $\gamma_{apb} = 0.15 \text{ Jm}^{-2}$ [44], and the experimentally determined values of $r_o = 10 \text{ nm}$ and $f = 0.004$ (cf. section 4.2.2), yields a theoretical predicted yield strength due to order hardening, σ_y^{OH} , of 55 MPa for the NA temper. The experimental yield strength, σ_y^{exp} , for this temper is however 310 MPa. This result strongly suggests that order hardening is not the main strengthening mechanism in this temper.

The contribution to strength due to the presence of each of the main alloying elements, Li, Cu and Mg, in the matrix of the NA temper can be estimated from equations (2.1) and (2.3), i.e. the contribution to solution strengthening from the elastic interaction component, τ^{EI} , and the contribution from the modulus interaction component, τ^{MI} . The sum of equations (2.1) and (2.3) for each solute element gives the contribution of that element to the CRSS due to solution strengthening, τ^{SS}_x . The matrix concentration, c_x , of these elements, as measured in the APT tests, is given in Table 4.1. Values of the modulus misfit parameter, ϵ_G , and the size misfit parameter, ϵ_a , as reported by Gomiero [34], are presented in Table 5.1. The effective matrix concentration of Cu in the NA temper decreased to 0.89 at.% after the Cu atoms in the Cu–Cu solute clusters were deducted from the global matrix Cu concentration. Mg and Li did not form any cluster or co–cluster and so their matrix concentration is effectively equal to the values given in Table 4.1. The total contribution to strength due to Cu in solution, τ^{SS}_{Cu} , is 18.72 MPa, while the strength due to Mg, τ^{SS}_{Mg} , and Li, τ^{SS}_{Li} , in solution is 9.45 MPa and 3.06 MPa, respectively. After Marceau [102], the total CRSS due to solution strengthening, τ^{SS} , was computed from a Pythagorean addition law of the form:

$$\tau^{SS} = \sqrt{\tau^{SS}_{Li}{}^2 + \tau^{SS}_{Cu}{}^2 + \tau^{SS}_{Mg}{}^2}. \quad (5.1)$$

Using the Taylor factor of 2.95 [77] yields a theoretical yield strength due to solution strengthening, σ_y^{SS} , of 63 MPa. This value is also significantly less than the experimental yield strength, which is a strong indication that strengthening in this temper is largely governed by the Cu–Cu clusters revealed in the APT cluster analysis [cf. Fig. 4.18 and Fig. 4.19]. Solute clusters are particularly known to confer significant amount of strength in nat-

urally aged Al–Cu–Mg–(Li) alloy systems [58,118]. The anomalous decrease in strength that occurs in these alloys during early stage of artificial aging of these alloys is associated with the dissolution of these solute clusters at high aging temperatures. Starink [118] recently proposed that strengthening due to clustering is governed by short–range order hardening. They argue that the atomic order in the clusters is extremely short ranged, typically 1–2 atoms thick, and as such obviates the glide of dislocation pairs since restoration of order is not possible upon shearing. This behaviour is in contrast with that observed for long–range ordered precipitates such as δ' , where the dislocations usually glide in pairs. Strengthening from order hardening arising from the glide of single dislocations results in strengths that are more than two times higher than in the cases where the dislocations glide in pairs [43]. Whether it is this short–range order hardening mechanism or it is another other mechanism, associated with the Cu–Cu clusters, that governs strengthening in the NA temper is still an open question. Regardless, the above analysis strongly indicates that the strength derived from the constituent obstacles other than the solute clusters is substantial and may constitute up to half of the total experimental yield strength of the NA temper. Specifically, these obstacles include the δ'/β' precipitates, solute atoms, grain boundaries and the dislocations introduced in the pre–straining step. Additional strengthening may arise from compressive residual stresses if they contribute to the uniform shifts in 2 θ peak positions observed in the HEXRD analysis (see section 4.3), and the corresponding change in lattice parameter.

Table 5.1: Size and modulus misfit parameters for the main alloying elements [34].

Element	Size misfit, ϵ_a , (at ⁻¹)	Modulus misfit, ϵ_G , (at ⁻¹)	Matrix conc., c (at%)
Li	10^{-2}	4	2.52
Cu	~ -0.35	~ 0.48	1.16
Mg	~ 0.37	~ 0.87	0.26

5.3 Strengthening mechanisms in the overaged temper

The TEM micrographs in Fig. 4.11(b) and (c) clearly reveal the presence of several different precipitates, including T_B , T_2 and δ'/β' in the OA temper. This result is consistent with observations made in the HEXRD investigation shown in Fig. 4.12, which also shows peaks associated with these phases. The HEXRD spectrum also show that equilib-

rium phases such as δ and θ , which were undetected in the TEM, are present in this temper. As noted earlier in section 4.3, the peaks associated with the T_B phase are particularly prominent, an indication that the volume fraction of this phase is significantly higher than that of the other phases present in this temper. The relatively larger peak intensity of the T_B phase in comparison to the other phases is also an indication that most of the precipitates which are likely to have formed during the early stages of the overaging treatment have dissolved, facilitating the precipitation of more equilibrium phases such as T_B phase. Although the presence of the δ' phase in this temper is somewhat surprising, its continued presence can be partly attributed to its relative stability, which is a consequence of its coherency with the matrix [74]. Additionally, the work of Lee [76] shows that the coarsening rate of δ' in Al–Li binary alloys is significantly reduced by the addition of small amounts of Ag. Similarly, Radmilovic [119] argued that $L1_2$ core/shell precipitates, such as δ'/β' , exhibit extremely low coarsening rates. The APT cluster analysis also indicates that a small amount of Cu–Cu clusters will be present in this temper. It follows from the preceding discussion that, as was the case for the PA and NA tempers, there are a number of possible sources of strength in the OA temper.

However, contributions to strength from equilibrium phase precipitates such as δ , θ , T_B and T_2 are known to be very small [120] and can therefore be neglected when computing the strength of the overaged alloys. The main strengthening precipitate present in this temper is the δ'/β' phase. As stated earlier in the case of the NA temper, i.e. in section 5.2, the δ'/β' phase is associated with order hardening and its contribution to the CRSS of the OA temper can be estimated from equation (2.18). Using the same parameters presented above for the NA temper and substituting values of r_o and f estimated from the TEM analysis of the OA temper (section 4.2.2) into equation (2.18) yields $\sigma_y^{OH} = 71$ MPa. As was the case for the NA temper, the effective matrix concentration of Cu in the OA temper decreased to 0.25 at.% after the Cu atoms in the Cu–Cu solute clusters were deducted from the global matrix Cu concentration. Likewise, Mg and Li did not form any cluster or co-cluster and so their matrix concentrations are effectively equal to the values given in Table 4.1. The theoretically predicted yield strength, σ_y^{SS} , for this temper computed using equation (5.1) a value of 38 MPa. The experimental yield strength of the OA temper is 133 MPa. Although additional contribution to strength can be expected from the Cu–Cu clus-

ters, grain boundaries and dislocations still present in the matrix, it can be argued that order hardening governs strength in the OA temper rather than Orowan hardening, as is the case for overaged tempers of most precipitation strengthened alloys. It can be further argued that the strengthening from the Cu–Cu clusters in the OA temper in comparison to the NA temper is negligibly small because of the significantly lower number density of clusters.

The fairly high value of σ_y^{OH} obtained for the OA temper indicates that order hardening is the dominant strengthening mechanism in the OA temper. This position is also supported by observations made in the conventional TEM and *in situ* TEM straining experiments. The largely planar nature of slip in this temper as shown in Fig. 4.11(d), and the dislocation pairs observed in the *in situ* TEM tensile straining experiments, as shown in Fig. 4.13, are well-known signatures of the order hardening mechanism [42–48,111].

6 Mechanism of plastic instability in Al–Li based alloys

Understanding the influence of the different microstructural constituents present in the investigated tempers of interest on the occurrence of plastic instability is critical for the identification of the microscopic mechanism(s) that govern plastic instability in the investigated alloy, AA2198. In this chapter, the observations made in the preceding chapters are examined in the light of existing models for plastic instability. It is shown that these models are unable to account for the phenomenon of plastic instability in the investigated alloy. Consequently, a more realistic mechanistic model that effectively explains the origin of the phenomenon is presented. The universality of the model, with regards to the occurrence of plastic instability in Al–Li binary and multicomponent alloys, is discussed in the last section of this chapter.

6.1 Dynamic strain aging

As previously discussed in section 2.2.3, it is widely accepted that the origin of negative strain rate sensitivity (nSRS) and, consequently, plastic instability in Al–Li based alloy systems is dynamic strain aging (DSA), i.e., the strain aging of temporarily trapped mobile dislocations by Li atoms [21–25]. A critical requirement for DSA is that there should be sufficient amount of the aging species, in this case Li, in solution. Depletion of Li atoms from the matrix of these alloy systems, as a result of the precipitation of Li bearing phases such as δ' (Al_3Li), is typically cited as the reason for the disappearance of plastic instability during aging of these alloys.

Quantitative characterization of the post–temper solute content in the matrix of the NA and OA tempers, as obtained as from the APT measurements, show that the Li concentration of the NA temper is $\sim 3\%$ more than that of the OA temper. The APT measure-

ments are consistent with the TEM and HEXRD results presented in sections 4.2 and 4.3. Both TEM and HEXRD analysis clearly show that there are more Li containing precipitates in the OA temper than in the NA temper. The APT measurements also indicate that the concentration of Mg, a known dynamic solute aging species, is the same in both tempers.

The preceding microstructural analyses suggest that if DSA by Li exclusively governs the occurrence of plastic instability in Al–Li based alloys, then the phenomenon should also occur in the NA temper since it has a higher concentration of Li than the OA temper, which displays plastic instability. The absence of plastic instability in the NA temper therefore strongly suggests that DSA is not the underlying microscopic mechanism for plastic instability in this alloy. This proposition is consistent with the view, expressed by other researchers on the basis of theoretical models [18–20], that DSA cannot independently lead to plastic instability. More so, as earlier mentioned in section 2.2.3, it has been suggested that dislocation pinning by Li atoms is unlikely in Al–Li alloys because of the weak binding energy of Li to dislocation cores [68]. This suggestion is further supported by the analysis presented in section 5.2; the contribution of Li in solution to solid solution strengthening, $\Delta\tau^{\text{SS}}$, is shown to be very small.

DSA by Mg, which is a well-known dynamic ageing species, is also unlikely to occur in this alloy as the nominal and experimentally measured concentrations of Mg in the investigated alloy are less than the critical concentration of Mg for plastic instability presented by Chinh [121]. In that work, it was shown, on the basis of room temperature tests carried out on Al–Mg alloys, that the minimum composition of Mg necessary for the occurrence of plastic instability in Al–Mg alloys is 0.95 at.%. The matrix Mg concentration in both the NA and OA tempers is 0.26 at.%, i.e., about 73% less than the proposed critical concentration. Furthermore, it can be argued that since both tempers have similar concentrations of Mg, they would have both displayed plastic instability if DSA by Mg governs the phenomenon.

It is also highly unlikely that forest aging, which was recently proposed as an additional mechanism that must occur concurrently with DSA for plastic instability to occur, can independently govern plastic instability since its rate sensitivity is known to be very

small [20]. It is thus concluded that neither DSA nor forest aging governs plastic instability in AA2198.

6.2 Precipitate shearing

As mentioned earlier in section 2.2.3, a number of authors have argued that plastic instability can be independently caused by the shearing of δ' phase in Al–Li alloys [26,27,29]. In the model proposed by Pink [26], it is argued that the collective glide of dislocations piled up at the matrix/ δ' interface would lead to plastic instability. However, the TEM investigation conducted in this work, as presented in section 4.2.3, indicate that the dislocations do not pile up at the matrix/ δ' interface of the OA temper (cf. Fig. 4.11d), rather they are planar in nature and they glide in pairs. Pink's model [26] is therefore inconsistent with experimental observations. More so, the model does not account for nSRS, which is well known fingerprint of plastic instability. Brechet [29] proposed that the shearing of precipitates accompanied by their dissolution and subsequent rapid re-precipitation during deformation can independently lead to nSRS. However, the time and temperature requirements for the complete dissolution and re-precipitation of δ' after shearing precludes the operation of such a mechanism at ambient temperatures [25,26]. In Behnood's model [27], it was envisaged that Li atoms may jump from within a sheared precipitate and pin down a section of a dislocation partly lying in the matrix. They argued that nSRS and subsequently plastic instability will occur under these conditions since higher stresses will be required to continue plastic deformation. Although this model, unlike that proposed by Pink [26], takes nSRS into account, it is unlikely that there will be sufficient driving force for the Li atoms to jump across the α/δ' interface. Besides, the proposition that the interaction between Li atoms and dislocations is very weak, and do not develop significant hardening [68], in addition to the observation in this work that very little strengthening arises from Li in solution, cast doubts on the viability of this model.

Furthermore, as mentioned in section 5.1, it has been shown through HAADF–STEM investigation [115] that the T_1 phase is sheared by dislocations, albeit by single shearing events. Yet plastic instability was not observed in the PA temper, the strength of which was largely governed by T_1 precipitates. This indicates that precipitate shearing that

occur by single shearing events do not lead to plastic instability. In other words, precipitate shearing by itself is not a sufficient condition for plastic instability.

6.3 Pseudo–locking: a new mechanism for plastic instability

The TEM analyses carried out in this work clearly show that although the δ'/β' phase is present in all three of the investigated tempers, the mechanical response in terms of the occurrence of plastic instability and the dislocation structure in these tempers are significantly different. Specifically, slip is planar and homogenous in the OA temper in contrast to the wavy, heterogeneous slip found in the NA temper. Since strain localization, which is one of the negative effects of plastic instability, is associated with planar and homogeneous slip [43,122], it is surmisable that the occurrence of plastic instability would be strongly influenced by the predominant strengthening mechanism.

It was established in section 5.3 that the dominant strengthening mechanism in the OA temper is order hardening. This conclusion is consistent with the widely accepted view that slip in Al–Li alloys containing δ' phase, which is a coherent and ordered phase, occurs by the glide of pairs of perfect dislocations. It is well established that the leading dislocations of the pairs destroys the order in the δ' precipitate, which has an $L1_2$ structure and creates an antiphase boundary (APB) within the precipitates upon shearing them while the trailing dislocations, loosely paired with the leading dislocation restores order. The energy of the APB represents the resistance that must be overcome by the matrix dislocations for slip to occur. Since the area of the antiphase boundary decreases with shearing, further deformation is favoured in the already sheared planes. Slip is therefore localized and planar in alloys where this mechanism is dominant [44,46,47]. Under the ideal conditions, i.e. when the APB formed by the leading dislocation (D_1) of the pair is perfectly restored by the trailing dislocation (D_2), the force equilibrium for the dislocation pair, D_1 and D_2 , at the critical configuration (see Fig. 6.1) is given in equations (6.1) and (6.2) [43]:

$$D_1: \tau b + \left(\frac{Gb^2}{2\pi(1-\nu)\Lambda} \right) - \gamma_{apb} \frac{d_1}{l_1} = 0, \quad (6.1)$$

$$D_2: \tau b - \left(Gb^2 / 2\pi(1 - \nu)\Lambda \right) + \gamma_{apb} d_2 / l_2 = 0, \quad (6.2)$$

where τ is the applied shear stress, G is the shear modulus, b is the Burgers vector of the dislocations, d_i is the average length of D_i lying in a precipitate, l_i is the mean distance between the precipitates sampled by D_i , Λ is the separation distance between the dislocation pair, ν is the Poisson's ratio of the matrix and γ_{apb} is the energy of the antiphase boundary per unit area in the δ' phase. Summation of equations (6.1) and (6.2) and rearranging terms leads to the elimination of the middle term, i.e. the force of interaction between the dislocations, and results in equation (6.3):

$$\tau^{OH} = \gamma_{apb} \frac{d_1}{2bl_1} - \gamma_{apb} \frac{d_2}{2bl_2}, \quad (6.3)$$

where τ^{OH} is the critical resolved shear stress predicted by order hardening. For an alloy system dominated by order hardening, $\tau^{OH} \approx \tau$. Following the work of Argon [43], equation (6.3) can be rewritten as equation (2.18). In sections 5.2 and 5.3, τ^{OH} for the NA and OA tempers was estimated from equation (2.18) and the results clearly indicated that order hardening governs strength in the OA temper but not in the NA temper.

We propose that the nSRS associated with plastic instability is induced by a diffusional reordering in the precipitates, resulting in a pseudo-locking mechanism analogous to that proposed by Morris [123] and Cuniberti [124] for discontinuous yield point phenomena in bulk long range-ordered alloys. In those models, the diffusional rearrangement of the APBs and its resultant decrease in energy in order-disorder alloys is proposed to account for the observed increase in the dissociation distance between the super partial dislocations. Now such a diffusional rearrangement of the APB in the δ' precipitates is proposed as the explanation for the plastic instability, and its associated nSRS, in the OA temper.

The first key point to note in the development of the pseudo-locking mechanism is the realization that the assumption that precipitation hardening is rate independent applies

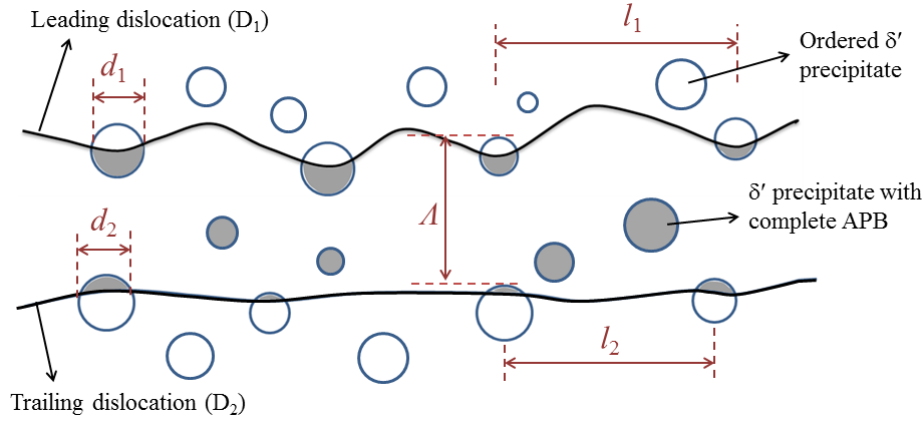


Fig. 6.1: Critical configuration of a dislocation pair cutting through a group of ordered coherent δ' precipitates. The shaded spheres represent precipitates with perfect APBs while the open spheres represent ordered precipitates. Spheres with both open and shaded areas represent precipitates with partial APBs. d_i is the average length of the dislocation, D_i lying in a precipitate, l_i is the mean distance between the precipitates sampled by D_i and A is the average distance between D_1 and D_2 .

mostly to the peak– or over–aged states where the ratio of the obstacle peak resistance force (\hat{k}) and line tension of the dislocation (2ξ) is greater than one. The glide of dislocations through an array of precipitates can be rate dependent in the underaged states where $\hat{k}/2\xi < 1$ [43,125]. Argon [43] contends that the effective (applied) stress on the dislocation at the point of contact with the obstacles is resisted by a force, k , which is slightly less than \hat{k} but is at a stable equilibrium position. It is further argued that the energy barrier between this initial equilibrium position and a so–called saddle–point position, which is almost at the exit point of the dislocation from the precipitate, is overcome by thermal activation. A simplified form of the theoretical CRSS predicted by order hardening for such a thermally assisted shearing process, $\tau^{OH}(T, \dot{\gamma})$, can be written as [43]:

$$\tau^{OH}(T, \dot{\gamma}) = \tau^{OH} \left[1 - \left(\frac{Tk_B \ln(\dot{\gamma}^*/\dot{\gamma})}{\Delta G_o^*} \right)^{\frac{1}{q}} \right]^{\frac{1}{p}}, \quad (6.4)$$

where T is the temperature, $\dot{\gamma}$ is the shear strain rate, respectively, p and q are constants in the range: 0.5 – 1.0 and 1.0 – 2.0 respectively, ΔG_o^* is a reference Gibbs free energy of thermal activation for the dislocation to move from the initial equilibrium position to the saddle–point. ΔG_o^* is usually taken at temperature, $T = 0\text{K}$ as a first approximation. k_B is the Boltzmann constant. The term $\dot{\gamma}^*$, can be expressed as:

$$\dot{\gamma}^* = b\rho_m\lambda v_G, \quad (6.5)$$

where ρ_m is the mobile dislocation density, λ is the Friedel spacing and v_G is the attempt frequency of a dislocation overcoming a thermally penetrable obstacle. Although the difference in strength arising from the thermal component is expected to be very small, it may nevertheless provide sufficient waiting time for the diffusion mechanism proposed now to occur.

As previously mentioned, a major characteristic of the order hardening mechanism is that the ordered precipitates form APBs in their active glide planes when they are sheared. The APB will be highly energetically unstable because of the many like bonds across it. There may therefore be sufficient time at low strain rates for thermal activation to modify this unstable interface by atomic rearrangement, i.e., reducing the number of like bonds across the APB. This atomic rearrangement will partially relax the APB, and consequently reduce the attractive pull of the APB on the trailing dislocation (D_2). τ^{OH} will thus become rate dependent since the second term in equation (6.3) will decrease with time. Assuming that the energy of the relaxed APBs ahead of the trailing dislocation is γ'_{apb} , equation (6.3) can be re-written as:

$$\tau^{OH} = \gamma_{apb} \frac{d_1}{2bl_1} - \gamma'_{apb} \frac{d_2}{2bl_2}. \quad (6.6)$$

Since γ'_{apb} is diffusion rate controlled it can be related to γ_{apb} by an Arrhenius type equation of the form:

$$\gamma'_{apb} = \gamma_{apb} * e^{-(Kt_w)}, \quad (6.7)$$

where K is an exponential factor and t_w is the waiting time during which the atomic rearrangements occurs when a dislocation is pinned in the precipitate. $t_w = 0$ is associated with the time at which the lead dislocation enters the precipitate and the APB is initiated. Following the usual approach in DSA models [10,18], t_w can be defined in terms of the strain rate as: $t_w = \Omega/\dot{\gamma}$, where Ω in this case will be related to the interparticle distance. Incorpor-

ration of equation (6.7) into equation (6.4) after appropriate substitution for t_w and γ'_{apb} leads to:

$$\tau^{OH}(T, \dot{\gamma}) = \left[\gamma_{apb} \left(\frac{d_1}{2bl_1} - e^{-\left(\frac{K\Omega}{\dot{\gamma}}\right)} \frac{d_2}{2bl_2} \right) \right] \left[1 - \left(\frac{Tk_B \ln(\dot{\gamma}^*/\dot{\gamma})}{\Delta G_o^*} \right)^{\frac{1}{q}} \right]^{\frac{1}{p}} \quad (6.8)$$

Equation (6.8) is the theoretical CRSS predicted by order hardening for a thermally assisted shearing process combined with the effect of a diffusional rearrangement of the APB. Although the exact form of the terms K and Ω in equation (6.8) is not yet clear, it is apparent on inspection that $\tau^{OH}(T, \dot{\gamma})$ increases with decreasing strain rate, $\dot{\gamma}$. In other words, higher shear stresses are required at low strain rates where atomic rearrangement occurs relative to high strain rates where these rearrangements will not occur because of insufficient time for diffusion. The mechanism of locking is such that at very low strain rates, atomic rearrangement will occur in precipitates sheared by D_1 , while D_2 becomes locked because the APB ahead of it has been partly reordered. This requires an increase in applied shear stress, $\Delta\tau$, for D_2 to glide. D_1 will also be locked because D_2 provides part of the energy required by D_1 at the current applied stress to continue deformation; the extra “push” supplied by the Peach–Köhler force decreases with increase in the separation distance between the dislocations. A pseudo-locking situation is therefore created under the condition of coupled dislocation glide. This APB locking effectively gives rise to a lowering of the SRS since an increase in τ will be required for deformation at low strain rates. Fig. 6.2 schematically illustrates both (a) edge-on and (b) in-plane views of the mechanism just described, in terms of the time dependent reordering of the slip plane from the perfect APB to a more re-ordered slip plane. At high strain rate the order hardening mechanism proceeds normally, with no rearrangement of the slip plane composition. With decreasing strain rate, diffusion is allowed to bring the entire precipitate to a more equilibrium (i.e., more uniform) composition, thus lowering the APB energy ahead of the trailing dislocations.

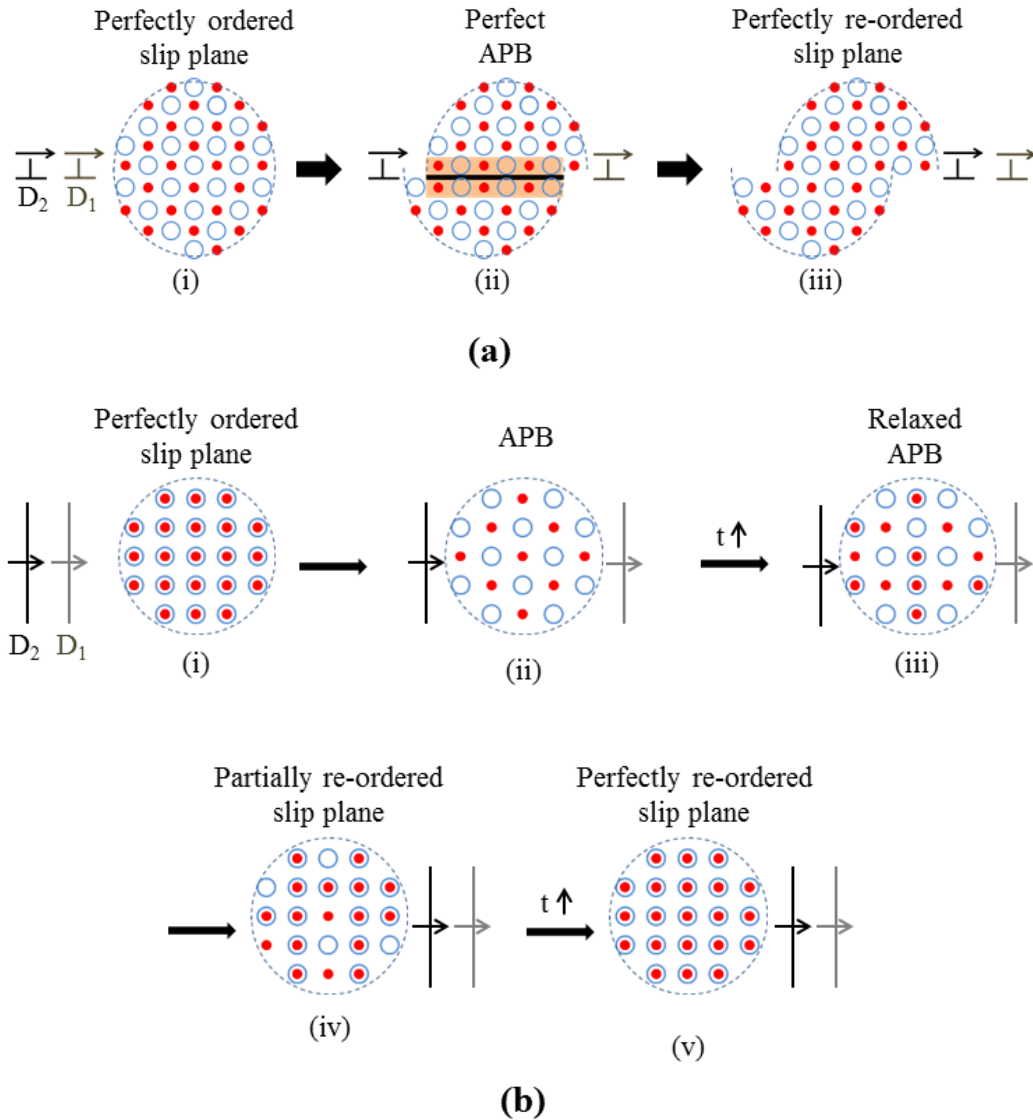


Fig. 6.2: Simplified illustration of (a) an edge-on view of the mechanism proposed here-in. At high strain rates the passage of the of leading dislocation, D_1 , through the δ' phase leaves an anti-phase boundary (APB) in its wake (i.e., ii), while the passage of the trailing dislocation, D_2 , recovers the perfect ordering of the precipitate (i.e., iii). At slow strain rates, a diffusion-controlled re-ordering of the APB between steps (ii) and (iii) leads to a higher critical stress for the second dislocation to pass through the precipitate. (b) an in-plane view of the slip plane through the δ' phase, showing the perfectly ordered state (i), the full APB (ii), the (relaxed) APB after a time, t , prior to the passage of D_2 (iii), the partially re-ordered slip plane formed after the passage of D_2 (iv) and the perfectly re-ordered slip plane.

6.4 Application of the proposed model to Al–Li based alloy systems

The mechanistic description of the origin of plastic instability in AA2198 given above effectively explains the occurrence of plastic instability in other Al–Li alloy systems. In the case of the AA2198 alloy studied here, it can be argued that plastic instability did not occur in the NA temper, in spite of sufficient amount of Li in its matrix, because strengthening in this temper is not governed by order hardening. This conclusion was reached in section 5.2 after estimating the contribution of order hardening to strength in the NA temper. The influence of the pseudo–locking mechanism in the NA temper is therefore insignificant since its strength is governed by another mechanism(s), consequently plastic instability is inhibited. As observed in this work (section 4.2.1) and consistent with other reports [73,74,126], subsequent aging to the PA temper leads to the precipitation of more potent strengthening precipitates such as S' , Ω and T_1 phases which clearly govern its strength. The precipitation of these phases additionally reduces the contribution of δ' phase to strengthening. Under these conditions, the diffusion–controlled pseudo–locking mechanism and by extension plastic instability will be suppressed. The dissolution of potent metastable phases such as Cu–Cu clusters, S' , Ω and T_1 and the formation of equilibrium phases as such T_2 and T_B at high aging temperatures/time effectively increases the contribution of the δ' phase, i.e. order hardening to the total CRSS in the OA temper. With order hardening dominating strengthening in this temper, the pseudo–locking mechanism becomes more active at low strain rates and thus provides the nSRS for plastic instability to occur. Order hardening has already been shown to be the main strengthening mechanism in the OA temper in section 5.3.

A critical review of literature shows that in binary Al–Li systems, plastic instability occurs from the quenched state until the peak aged state, where the instability sometimes disappear [21,25,27,127]. This observation explains why several authors [21–25] argue for DSA as the origin of plastic instability in Al–Li alloys. Proponents of this view associate the disappearance of instabilities in these alloys to the depletion of Li from the matrix as a result of the precipitation of δ' (Al_3Li) phase. For instance, Kumar [21] in their work on Al–1.47 wt% Li and Al–2.8 wt% Li binary alloys, observed that plastic instabilities were present in both alloys in both solution treated and quenched, and underaged states when

the alloy where tested at a strain rate of $6.45e^{-5} s^{-1}$. The magnitude of the stress drops associated with the plastic instabilities however decreased on ageing such that at the peak aged state, no stress drops were observed. Chmelik [25] also observed plastic instabilities in the solution treated and quenched state of Al–1.06 wt% Li and Al–2.35 wt% Li binary alloys tested at a strain rate of $4.4e^{-6} s^{-1}$. The underaged and peak aged tempers of the Al–2.35 wt% Li alloy in the underaged and peak aged states also manifested plastic instabilities but with significantly diminished stress drops. In the overaged state, they observed instabilities similar to those found in the solution treated and quenched state. The experimental evidence provided in this work however shows that DSA acting alone is not sufficient to cause plastic instability. Since δ' phase is known to form rapidly at room temperature upon quenching from the solution treated state [49], it can be argued that order hardening already operates from the early stages of aging in the binary Al–Li systems and governs strengthening in binary Al–Li alloys. Conditions for plastic instability to occur, i.e., DSA and order hardening, are therefore always present in these alloys up to the peak aged state. At the peak aged state, DSA and, by extension, plastic instability may be inhibited as a result of a possible breakdown of the order hardening mechanism. It is argued that at the peak aged state in binary Al–Li alloys, the precipitate radius reaches a limiting value where precipitate shearing tends to give way to looping [42]. Order hardening will be prevented from occurring under such conditions.

In quaternary and commercial Al–Li based alloys, the instability behaviour is quite varied and largely depends on the composition of the alloy and its thermomechanical treatment. For example, Huang [67] investigated an Al–2.9 wt% Li–1wt% Cu–0.12 wt% Zr quaternary alloy in compression and observed plastic instabilities at strain rates less than $10 s^{-1}$ in the solution treated/quenched, naturally aged and underaged states. They however observed that the magnitude of the stress drops increased with increase in aging time. In contrast, the work of Shen [8] on another quaternary alloy with concentration, Al–2.05 wt% Li–2.86 wt% Cu–0.12 wt% Zr reveals a decrease in the magnitude of the stress drops with increase in aging temperature/time. Furthermore, in a recent work by Deschamps [58] on a commercial alloy, AA2196, plastic instabilities were observed in the stretched and naturally aged, i.e. T351 state, and during the early stages of artificial ageing. The instabilities completely disappeared before the peak aged state. According to the authors, the main strengthening precipitate in this alloy during the early stages of ageing is

δ' . Deschamps [58] also investigated AA2198, i.e., same alloy investigated in this work. As was the case in this work, they did not observe plastic instability in the stretched and naturally aged state (referred to as NA in this work) which they suggested consisted of Cu-rich solute clusters or in tempers where sufficient amounts of T_1 and θ' phases were present. Plastic instabilities were however observed in the early stages of artificial ageing where the solute clusters had dissolved and strength was likely governed by order hardening.

Apart from the work of Huang [67] who observed an increase in the magnitude of the stress drops with increase in ageing time, other workers [8,22,58,128,129], regardless of the composition of the multi-component Al–Li based alloy system they investigated, observed a decrease in the magnitude of the observed stress drops or a complete disappearance plastic instability with increase in ageing temperature and/or time. This trend usually occurs in the underaged states and can be attributed to the precipitation of more potent strengthening precipitates such as T_1 , θ' and S' . When strengthening from these phases become dominant, the order hardening mechanism and the pseudo-locking mechanism described above will be suppressed. It can be argued that there will still be sufficient amount of Li in the matrix in the underaged states of these alloys to facilitate DSA but the suppression of order hardening hinders the manifestation of the plastic instability.

7 Concluding remarks

Detailed experimental work carried out to unravel the microscopic origin of plastic instability in a precipitation strengthened Al–Li–Cu–Mg–Zr based alloy, AA2198, was presented in this thesis. Specifically, mechanical and microstructural characterization of three representative tempers of the investigated alloy, including the stretched and naturally aged temper (NA), the peak aged temper (PA) and the overaged temper (OA), was performed using state-of-the-art techniques. The mechanical response of the investigated temper states, with particular focus on their instability behaviour, was assessed with micro-tensile and high resolution nanoindentation tests. Microstructural characterization of precipitate phases of the three tempers was achieved with a combination of transmission electron microscopy (TEM) and high energy x-ray diffraction (HEXRD), while their respective matrix solute content was quantitatively determined with atom probe tomography (APT). Direct correlation of the mechanical response to microstructural influences was achieved with *in situ* TEM tensile tests.

Plastic instability was only observed in the OA temper of the alloy. Quantitative analysis of the APT results however showed that the matrix concentration of Li in the OA temper where plastic instability was observed is less than that of the NA temper. The results clearly indicated that dynamic straining aging (DSA) of temporarily trapped mobile dislocations by Li atoms, which is the most widely accepted model for plastic instability in Al–Li based alloy systems, cannot sufficiently account for the occurrence of the plastic instability in the investigated alloy. The results also suggest that precipitate shearing by single shearing events do not lead to plastic instability. It was thus proposed that a diffusion-controlled mechanism which involves the operation of a pseudo-locking mechanism that accompanies order hardening at low strain rates initiates negative strain rate sensitivity (nSRS) and subsequently leads to plastic instability in the OA temper. Order hardening is

the strengthening mechanism associated with δ' (Al_3Li) precipitates. It was argued that the pseudo-locking mechanism is induced by a diffusional reordering of the disordered atoms around the active shear plane in the δ' precipitates. This diffusional reordering, a strain rate dependent mechanism, relaxes the antiphase boundary energy (APB) at low strain rates and ultimately leads to an increase in strength. At high strain rates, the order hardening mechanism proceeds normally with no rearrangement of the slip plane composition and therefore leads to lower strength relative to strengths encountered at low strain rates.

It was shown, through the *in situ* TEM tensile straining experiments and the theoretical analysis of strength contributions of different obstacles in the OA temper, that δ' precipitate is the main strengthening phase in the OA temper. It was also shown that δ' precipitates, though present in the NA and PA tempers, do not govern the strength. Specifically, the results indicate that strength in the case of the NA temper is mainly governed by Cu-Cu solute clusters, while in the case of the PA temper, strength is well known to be due to the T_1 (Al_2CuLi) phase.

The proposed mechanistic model for plastic instability in AA2198 was also shown to be applicable to other Al-Li based alloys systems, including binary and multicomponent alloys. In general, it was demonstrated by critical examination of the instability behaviour of a number of Al-Li based alloys reported in literature that plastic instability would occur in any temper of an Al-Li based alloy whose strength is governed by order hardening.

Finally, a modified order hardening model that predicts the theoretical critical resolved shear stress (CRSS) for such a diffusion controlled process combined with the effect of a diffusional rearrangement of the APB was also proposed. While the pseudo-locking mechanism proposed in this work for plastic instability in Al-Li based alloy systems is physically sound, it is noted that the mechanism strongly hinges on the energetic driving forces for two distinct processes, namely the diffusional rearrangement of atoms within the δ' precipitates and the energy difference between the perfect APB and that after diffusional rearrangement. These aspects cannot be directly experimentally addressed; ab initio calculations, which are not yet available within the literature for these alloy systems, are needed to fully establish the viability of the diffusional rearrangement and the magni-

tude of the energy difference that accompanies it. However, the occurrence of rapid and significant APB relaxation at homologous temperatures, which are comparable with that of the experiments carried out within the present work, has indeed been observed in bulk, long-range ordered alloy systems such as Cu–Zn–Al, Al₅Ti₂Fe, Al₅Ti₂Mn and Ni₃Fe [124,130]. It is interesting to note that these alloy systems also exhibited plastic instability.

Appendix

Crystallographic data for generating simulated diffraction patterns used for the HEXRD analysis

Phase Id/ Comp.	Structure	Lattice parameter	Space Grp #	Multiplicity /Wyckoff letter	Positions			Occupancy
					x	y	z	
T_B (Al ₇ Cu ₄ Li)	Cubic (CaF ₂)	a=0.583	225	4a	0	0	0	100%Cu
				8c	0.25	0.25	0.25	0.875Al+0.12Li
T₁ (Al ₂ CuLi)	Hexagonal (P6/mmm)	a=0.497 c=0.935	191	1a	0	0	0	100%Al
				1b	0	0	0.5	100%Li
				2c	0.3333	0.6667	0	100%Li
				2d	0.3333	0.6667	0.5	100%Al
				6i	0.5	0	0.25	0.5Al+0.5Li
T₂ (Al ₅ CuLi ₃)	Cubic Im-3 (cI162)	a=1.3914	204	48h	0.0969	0.3140	0.3320	0.94Al+0.06Cu
				24g	0	0.1194	0.2942	0.84Li+0.16Cu
				24g	0	0.1501	0.0908	0.94Al+0.06Cu
				24g	0	0.3007	0.1748	0.94Al+0.06Cu
				16f	0.1836	0.1836	0.1836	0.84Li+0.16Cu
				12e	0.0998	0	1/2	0.84Li+0.16Cu
				12e	0.3203	0	1/2	0.84Li+0.16Cu
				2a	0	0	0	0.94Al+0.06Cu
δ (AlLi)	Cubic (NaTl) B32 Fd3m	a=0.637	227	8a	0	0	0	100%Al
				8b	0.5	0.5	0.5	100%Li
δ' (Al ₃ Li)	Cubic (Au ₃ Cu) L1 ₂ Pm-3m	a=0.404	322 221	1a	0	0	0	100%Li
				3c	0	0.5	0.5	100%Al
θ (Al ₂ Cu)	Tetragonal (I4/mcm)	a=0.6067 c=0.4877	140	4a	0	0	0.25	100%Cu
				8h	0.1581	0.6581	0	100%Al
θ' (Al ₂ Cu)	Tetragonal (I-4m2)	a=0.404 c=0.58	140 119	2a	0	0	0	100%Al
				2b	0	0	0.5	100%Al
				2c	0	0.5	0.25	100%Cu
β' (Al ₃ Zr)	Cubic (Au ₃ Cu) L1 ₂ Pm-3m	a=0.413	322 221	1a	0	0	0	100%Zr
				3c	0	0.5	0.5	100%Al
S' (Al ₂ CuMg)	Orthorhombic (Cmcm)	a=0.404 b=0.925 c=0.715	63	4c	0	0.778	0.25	100%Cu
				4c	0	0.072	0.25	100%Mg
				8f	0	0.326	0.056	100%Al
Ω (Al ₂ Cu)	Orthorhombic (Fmmm)	a=0.496 b=0.859 c=0.848- 0.935	69	8f	0.25	0.25	0.25	100%Cu
				8h	0	0.3333	0	100%Al
				8i	0	0	0.167	100%Al

Supplementary material

The following is a link to the video recorded during the *in situ* TEM tensile straining of the overaged (OA) temper:

https://powerfolder.hzgg.de/dl/fiQUdr3Yk9q5GvHttBhdkt0B/In_situ_TEM_movie_OA.mp4

References

- [1] Picu RC, Vincze G, Ozturk F, Gracio JJ, Barlat F, Maniatty, AM. Strain rate sensitivity of the commercial Aluminium alloy AA5182–O. *Materials Science and Engineering A* 2005; 390:334.
- [2] Thevenet D, Milha–Touati M, Zeghloul A. The effect of precipitation on the Portevin–Le Chatelier effect in an Al–Zn–Mg–Cu alloy. *Materials Science and Engineering A* 1999; 266:175.
- [3] Klose FB, Weidenmüller J, Ziegenbein A, Hähner P, Neuhäuser H. Plastic instabilities with propagating deformation bands in Cu–Al alloys. *Philosophical Magazine A* 2004; 84(3–5):467.
- [4] Qiu W, Han E, Liu L. Serrated flow behaviour during compression at Elevated temperatures in Mg–3Al–1Zn–0.1RE alloy. *Journal of Material Science Technology* 2009; 25(4):441.
- [5] Corby C, Cáceres CH, Lukác P. Serrated flow in magnesium alloy AZ91. *Materials Science and Engineering A* 2004; 387:22
- [6] Canadinc D, Efstathiou C, Sehitoglu H. On the negative strain rate sensitivity of Hadfield steel. *Scripta Materialia* 2008; 59(10):1103.
- [7] Hong S–G, Lee S–B. Mechanism of dynamic strain aging and characterization of its effect on the low cycle fatigue in type 316L stainless steel. *Journal of Nuclear Materials* 2005: 340: 307.
- [8] Shen YZ, Oh KH, Lee DN. Serrated flow behaviour in 2090 Al–Li alloy influenced by texture and microstructure. *Materials Science and Engineering A* 2006; 435:343.
- [9] Yilmaz A. The Portevin–Le Chatelier effect: a review of experimental findings. *Science and Technology of Advanced Materials* 2011; 12: 063001.
- [10] Picu RC. A mechanism for the negative strain rate sensitivity of dilute solid solutions. *Acta Materialia* 2004; 52:3447.
- [11] Dierke H, Krawehl F, Graff S, Forest S, Sachl J, Neuhäuser H. Portevin–Le Chatelier effect in Al–Mg alloys: Influence of obstacles – experiments and modelling. *Computational Materials Science* 2007; 39(1):106.
- [12] Mulford RA, Kocks UF. New observations on the mechanisms of dynamic strain aging and of jerky flow. *Acta Metallurgica* 1979; 27:1125
- [13] Estrin Y, Kubin LP. Plastic instabilities: phenomenology and theory. *Materials Science and Engineering A* 1991; 137:125.

- [14] Kubin LP, Estrin Y. The critical conditions for jerky flow: Discussion and application to CuMn solid solutions. *Physica Status Solidi B* 1992; 172(1):173.
- [15] Schoeck G. The Portevin–Le Chatelier effect. A kinetic theory. *Acta Metallurgica* 1984; 32(8):1229.
- [16] Franklin SV, Mertens F, Marder M. Portevin–Le Chatelier effect. *Physical Review E* 2000; 62(6):8195.
- [17] Rizzi E, Hähner P. On the Portevin–Le Chatelier effect: Theoretical modelling and numerical results. *International Journal of Plasticity* 2004; 20:121.
- [18] Hähner P. On the physics of the Portevin–Le Chatelier effect part 1: The statistics of dynamic strain aging. *Material Science and Engineering A* 1996; 207:208.
- [19] Soare MA, Curtin WA. Single–mechanism rate theory for dynamic strain aging in fcc metals. *Acta Materialia* 2008; 56:4091.
- [20] Soare MA, Curtin WA. Solute strengthening of both mobile and forest dislocations: the origin of dynamic strain aging in FCC metals. *Acta Materialia* 2008; 56:4046.
- [21] Kumar S, Król J, Pink E. Mechanism of serrated flow in binary Al–Li alloys. *Scripta Materialia* 1996; 35(6):775.
- [22] Gregson PJ, McDermid DS, Hunt E. Post–yield deformation characteristics in Al–Li alloys. *Materials Science and Technology* 1988; 4:713.
- [23] Cieslar M, Vostrý P, Stulíková I. Phase composition and jerky flow in Al–Li–Mg–Cu alloy. *Physica Status Solidi A* 1996; 157:217.
- [24] Kubin LP, Styczynski A, Estrin Y. Discontinuous yielding in an Al–Li–Zr alloy. *Scripta Materialia* 1992; 26:1423.
- [25] Chmelík F, Pink E, Król J, Balík J, Pešička J, Lukáč. Mechanisms of serrated flow in aluminium alloys with precipitates investigated by acoustic emission. *Acta Materialia* 1998; 46(12): 4435.
- [26] Pink E, Kumar S, Baohui T. Serrated flow of aluminium alloys influenced by precipitates. *Material Science and Engineering A* 2000; 280:17.
- [27] Behnood N, Evans JT. Plastic deformation and the flow stress of Aluminium–lithium alloys. *Acta Metallurgica* 1989; 37(2): 687.
- [28] Kumar S, Pink E. Effect of δ' precipitates on serrated flow. *Scripta Metallurgica Materialia* 1995; 32(5): 749.
- [29] Brechet Y, Estrin Y. On a pseudo–Portevin–Le Chatelier effect. *Scripta Metallurgica et Materials* 1994; 31(5): 185.
- [30] Dieter GE. *Mechanical metallurgy*. McGraw–Hill, London, 1988.

-
- [31] Haasen P. Mechanical properties of solid solutions in: Physical metallurgy III, 4th ed. Cahn RW and Haasen P, eds. Elsevier Science 1996.
- [32] Ryen O, Nijs O, Sjolander E, Holmdeal B, Ekstrom, H, Nes E. Strengthening mechanisms in solid solution Aluminium alloys. Metallurgical and Materials Transactions A 2006, 37: 1999.
- [33] Courtney TH. Mechanical behavior of materials, 2nd ed. Waveland Press Inc., Illinois, 2005.
- [34] Gomiero P, Brechet Y, Louchet F, Tourabi A, Wack B. Microstructure and mechanical properties of a 2091 AlLi alloy – II. Mechanical properties: yield strength and work hardening. Acta metallurgica and materialia 1992, 40:857.
- [35] Wang SC, Zhu Z, Starink MJ. Estimation of dislocation densities in cold rolled Al–Mg–Cu–Mn alloys by combination of yield strength data, EBSD and strength models. Journal of microscopy 2005, 217(2): 174.
- [36] Soboyejo W. Mechanical properties of engineered materials. Marcel Dekker, New York, 2003.
- [37] Russell AM, Lee LK. Structure–property relations in nonferrous metals. John Wiley and sons, New Jersey, 2005.
- [38] Hull D, Bacon DJ. Introduction to dislocations, 5th ed. Elsevier, oxford, 2011.
- [39] Smallman RE, Ngan, AHW. Physical metallurgy and advanced materials, 7th ed. Elsevier, Oxford, 2007.
- [40] Kocks UF, Mecking H. Physics and phenomenology of strain hardening: the FCC case. Progress in materials science 2003, 48: 171.
- [41] Estrin Y, Toth LS, Molinari A, Brechet Y. A dislocation based model for all hardening stages in large strain deformation. Acta Materialia 1998, 46(15):5509.
- [42] Ardell AJ. Precipitation hardening. Metallurgical Transactions A 1985; 16: 2131.
- [43] Argon AS. Strengthening mechanisms in crystal plasticity. Oxford University press, Oxford, 2008.
- [44] Huang JC and Ardell AJ. Precipitation strengthening of Binary Al–Li alloys by δ' precipitates. Materials Science Engineering A 1988; 104:149.
- [45] Lendvai J. Precipitation and strengthening in aluminium alloys. Materials Science Forum 1996; 217–222: 43.
- [46] Schlesier C, Nembach E. Strengthening of aluminium–lithium alloys by long–range ordered δ' –precipitates. Acta Metallurgica et Materialia 1995; 43(11): 3983.

- [47] Noble B, Harris SJ and Dinsdale K. Yield characteristics of aluminium–lithium alloys. *Metal Science* 1982; 16: 425.
- [48] Furukawa M, Miura Y, Nemoto M. Strengthening mechanisms in Al–Li alloys containing coherent ordered particles. *Transactions of the Japan Institute of Metals* 1985; 26(4):230.
- [49] Lendvai J, Wunderlich W, Gudladt HJ. Formation of $L1_2$ ordered precipitates at room temperature and their effect on the mechanical properties in Al–Li alloys. *Philosophical Magazine A* 1993; 67(1):99.
- [50] Schwab R, Ruff V. On the nature of the yield point phenomenon. *Acta Materialia* 2013; 61(5):1798.
- [51] Ananthakrishna G. Current theoretical approaches to collective behaviour of dislocations. *Physics Reports* 2007; 440:113.
- [52] Picu RC, Zhang D. Atomistic study of pipe diffusion in Al–Mg alloys. *Acta Materialia* 2004; 52:161.
- [53] Curtin WA, Olmsted DL, Hector Jr LG. A predictive mechanism for dynamic strain ageing in aluminium–magnesium alloys. *Nature materials* 2006; 5:875.
- [54] Jiang H, Zhang Q, Chen X, Chen Z, Jiang Z, Wu X, Fan J. Three types of Portevin–Le Chaterlier effects: Experiment and modelling. *Acta Materialia* 2007; 55:2219.
- [55] Chatterjee A, Sarkar A, Barat P, Mukherjee P, Gayathri N. Character of the deformation bands in (A+B) regime of the Portevin–Le Chaterlier effect in Al–2.5%Mg alloy. *Materials Science and Engineering A* 2009; 508:156.
- [56] Klose FB, Ziegenbein A, Hagemann F, Neuhäuser H, Hähner P, Abbadi M, Zeghloul A. Analysis of Portvein–Le Chaterlier serrations of type B in Al–Mg. *Materials Science and Engineering A* 2004; 369: 74.
- [57] Fan GJ, Wang GY, Choo H, Liaw PK, Park YS, Han BQ, Lavernia EJ. Deformation behaviour of an ultrafine–grained Al–Mg alloy at different strain rates. *Scripta Materialia* 2005; 52:929.
- [58] Deschamps A, Decreus B, De Geuser F, Dorin T, Weyland M. The influence of precipitation on plastic deformation of Al–Cu–Li alloys. *Acta Materialia* 2013; 61:4010.
- [59] Horváth G, Chinh NQ, Gubicza J, Lendvai J. Plastic instabilities and dislocation densities during plastic deformation in Al–Mg alloys. *Materials Science and Engineering A* 2007; 445–446:186.
- [60] Tian B. Comparing characteristics of serrations in Al–Li and Al–Mg alloys. *Materials Science and Engineering A* 2003; 360:330.

-
- [61] Kovács Z, Fátay D, Nyilas K, Lendvai J. Effect of grain boundaries on PLC plastic instabilities. *Journal of Engineering Materials and Technology* 2002; 124:23.
- [62] Cheng X–M, Morris JG. The anisotropy of the Portevin–Le Chatelier effect in aluminium alloys. *Scripta Materialia* 2000; 43:651.
- [63] Robinson JM. Serrated flow in aluminium based alloys. *International Materials Review* 1994; 39(6):217.
- [64] Weiss J, Richeton T, Louchet F, Chmelik F, Dobron P, Entemeyer D, Lebyodkim M, Lebedkina T, Fressengeas C, McDonald RJ. Evidence for universal intermittent crystal plasticity from acoustic emission and high–resolution extensometry experiments. *Physical Review B* 2007; 76:224110–8.
- [65] Dimiduk DM, Woodward C, Lesar R, Uchic MD. Scale free intermittent flow in crystal plasticity. *Science* 2006; 312:1188.
- [66] Hähner P. On the physics of the Portevin–Le Chatelier effect part 2: The statistics of dynamic strain aging. *Material Science and Engineering A* 1996; 207:215.
- [67] Huang JC, Gray GT. Serrated flow and negative rate sensitivity in Al–Li based alloys. *Scripta metallurgica et materialia* 1990; 24:85.
- [68] Evans JT. Interaction between lithium atoms and dislocations in Al–Li solid solutions. *Scripta Metallurgica* 1987; 21:1435.
- [69] Decreus B, Deschamps A, De Geuser F, Donnadiou P, Sigli C, Weyland M. The influence of Cu/Li ratio on precipitation in Al–Cu–Li–x alloys. *Acta Mater* 2013; 61:2207.
- [70] Lavernia EJ, Grant NJ. Aluminium–lithium alloys. *Journal of Materials Science* 1987; 22:1521
- [71] Rioja RJ, Liu J. The evolution of Al–Li base products for aerospace and space applications. *Metallurgical and Material Transactions A* 2012; 43:3325.
- [72] Martin JW. Aluminium–lithium alloys. *Annual Review of Materials Science* 1988; 18: 101.
- [73] Donnadiou P, Shao Y, De Geuser F, Botton GA, Lazar S, Cheynet M, De Boissieu M, Deschamps A. Atomic structure of T₁ precipitates in Al–Li–Cu alloys revisited with HAADF–STEM imaging and small–angle x–ray scattering. *Acta Materialia* 2011; 59:462.
- [74] Wang SC, Starink MJ. Precipitates and intermetallic phases in precipitation hardening Al–Cu–Mg–(Li) based alloys. *International Materials Reviews* 2005; 50(4):193.
- [75] Chen Z, Zhao K, Fan L. Combinative hardening effects of precipitation in a commercial aged Al–Cu–Li–X alloy. *Materials Science Engineering A* 2013; 588:59.

- [76] Lee YS. Microstructure in overaged Al–Cu–Li–Mg–Ag alloys. *Journal of Materials Science Letters* 1998; 17:1161.
- [77] Starink MJ, Wang P, Sinclair I, Gregson PJ. Microstructure and strengthening of Al–Li–Cu–Mg alloys and MMCS: II. Modelling of yield strength. *Acta Materialia* 1999; 47(14): 3855.
- [78] Yoshimura R, Konno TJ, Abe E, Hiraga K. Transmission electron microscopy study of the evolution of precipitates in aged Al–Li–Cu alloys: The θ' and T_1 phases. *Acta Materialia* 2003; 51:4251.
- [79] Vecchio KS, Williams DB. Convergent beam electron diffraction analysis of the T_1 (Al_2CuLi) phase in Al–Li–Cu alloys. *Metallurgical Transactions A* 1988; 19:2885.
- [80] De PS, Mishra RS, Baumann JA. Characterization of high cycle fatigue behaviour of a new generation aluminium lithium alloy. *Acta Materialia* 2011; 59:5946.
- [81] Kumar KS, Heubaum FH. The effect of Li content on the natural aging response of Al–Cu–Li–Mg–Ag–Zr alloy. *Acta Materialia* 1997; 45(6):2317.
- [82] Ohmori Y, Ito S, Nakai, K. Aging behaviour of an Al–Li–Cu–Mg–Zr alloy. *Metallurgical and Materials Transactions A* 1999; 30:714.
- [83] Lefebvre W, Houmada K, Decreus B, de Geuser F. Characterization of Pre-precipitation stages by atom probe tomography and small angle X-ray scattering in an Al–Li–Cu–Mg–Ag alloy. In: *Proceedings of the 11th International Conference on Aluminium alloys, Aachen, Germany, vol. 1. Weinheim: Wiley–VCH; 2008. p.801–807.*
- [84] Chen PS, Bhat BN. Time–temperature–precipitation behaviour in Al–Li alloy 2195. *NASA/TM* 2002:211548
- [85] Hay JL, Pharr GM. Instrumented indentation testing, in: *ASM handbook vol. 8, ASM International, 2000. p495 – 525.*
- [86] Oliver WC, Pharr GM. An improved technique for determining hardness and elastic modulus using load and displacement sensing indentation experiments. *Journal of Material Research* 1992; 7(6):1564.
- [87] Maier V, Durst K, Mueller J, Backes B, Höppel HW, Göken M. Nanoindentation strain–rate jump tests for determining the local strain–rate sensitivity in nanocrystalline Ni and ultrafine–grained Al. *Journal of Materials Research* 2011; 26(11):1421.
- [88] Vanlandingham MR. Review of instrumented indentation. *Journal of Research of the National Institute of Standards and Technology* 2003; 108(4):249.
- [89] Li J, Malis T, Dionne S. Recent advances in FIB–TEM specimen preparation techniques. *Materials characterization* 2006; 59:64.

-
- [90] Giannuzzi LA, Stevie FA. A review of focussed ion beam milling techniques for TEM specimen preparation. *Micron* 1999; 30:197.
- [91] Willaims DB, Carter CB. *Transmission electron microscopy*. Vol. 2., Springer Science and Business Media, New York, 2009.
- [92] Ringer SP, Muddle BC, Polmear IJ. Effects of cold work on precipitation in Al–Cu–Mg–(Ag) and Al–Cu–Li–(Mg–Ag) alloys. *Metallurgical and Materials Transactions A* 1995; 26:1659.
- [93] Pickens JR, Kumar KS, Brown SA, Gayle FW. Evaluation of microstructure of Al–Cu–Li–Ag–Mg Weldite alloys. *NASA/ STI* 1991; 19910015091:p60.
- [94] Matsukawa Y, Liu GS. *In situ* TEM study on elastic interaction between a prismatic loop and a gliding dislocation. *Journal of Nuclear Materials* 2012; 425:54.
- [95] Cerezo A, Clifton PH, Galtrey MJ, Humphreys CJ, Kelly TF, Larson DJ, Lozano–Perez S, Marquis EA, Oliver RA, Sha G, Thompson K, Zandbergen M, Avis RL. Atom probe tomography today. *Materials Today* 2007; 10(12):36.
- [96] Miller MK, Forbes RG. Atom probe tomography. *Materials Characterization Techniques* 2009; 60:461.
- [97] Miller MK, Kelly TF, Rajan K, Ringer SP. The future of atom probe tomography. *Materials Today* 2012; 15(4):158.
- [98] Gault B, Moddy MP, Cairney JM, Ringer SP. *Atom probe microscopy*. Springer, 2012, New York.
- [99] Gault B, De Geuser F, Bourgeois L, Gabbale BM, Muddle BC. Atom probe tomography and transmission electron microscopy characterisation of precipitation in an Al–Cu–Li–Mg–Ag alloy. *Ultramicroscopy* 2011; 111:683.
- [100] Philippe T, De Geuser F, Duguay S, Lefebvre W, Cojocar–Miredin O, Da Costa G, Blavette D. Clustering and nearest neighbour distances in atom probe tomography. *Ultramicroscopy* 2009; 109:1304.
- [101] Marceau RKW, Sha G, Ferragut R, Dupasquier A, Ringer SP. Solute clustering in Al–Cu–Mg alloys during the early stages of elevated temperature ageing. *Acta Materialia* 2010; 58: 4923.
- [102] Marceau RKW, De Vaucorbeil A, Sha G, Ringer SP, Poole WJ. Analysis of strengthening in AA6111 during the early stages of ageing: Atom probe tomography and yield strength modelling. *Acta Materialia* 2013; 61:7285.
- [103] Bray JW. Aluminum mill and engineered wrought products, in: *ASM handbook Vol. 2*, ASM International, 1990. p29 – 61.
- [104] Ashby MF. Work hardening of Dispersion–hardened crystals. *Philosophical Magazine*, 1966; 14(132):1157.

- [105] Schuh CA. Nanoindentation studies of materials. *Materials Today*, 2006, 9(5):32.
- [106] Chinh NQ, Gubicza J, Kovács Z, Lendvai J. Depth-sensing indentation tests in studying plastic instabilities. *Journal of Materials Research* 2004; 19(1):31.
- [107] Cahn JW, Nutting J. Transmission quantitative metallography. *Transactions of the Metallurgical Society of AIME*, 1959; 215:526.
- [108] Kumar KS, Brown SA, Picken JR. Microstructural evolution during aging of an Al–Cu–Li–Ag–Mg–Zr alloy. *Acta Materialia* 1996; 44(5):1899.
- [109] Axon HJ, Hume–Rothery W. *Proceedings of the Royal Society of London A*, 193:1032 (1948) 1–24.
- [110] Reimers W, Pyzalla AR, Schreyer A, Clemens H (Eds.), *Neutrons and synchrotron radiation in engineering materials science*, Wiley–VCH, Weinheim, 2008.
- [111] Rosner H, Liu W, Nembach E. *In situ* transmission electron microscopy observations of dislocations processes in δ' –strengthened aluminium–lithium alloys. *Philosophical Magazine A* 1999; 79(12):2935.
- [112] Phillippe T, De Geuser F, Duguay S, Lefebvre W, Cojocar–Miredin O, Da Costa G, Blavette D. Clustering and nearest neighbour distances in atom–probe tomography. *Ultramicroscopy* 2009; 109:1304.
- [113] Gault B, Cui XY, Moody MP, De Geuser F, Sigli C, Ringer SP, Deschamps A. Atom probe microscopy investigation of Mg site occupancy within δ' precipitates in an Al–Mg–Li alloy. *Scripta Materialia* 2012; 66:903.
- [114] Araullo–Peters V, Gault B, De Geuser F, Deschamps A, Cairney JM. Microstructural evolution during ageing of Al–Cu–Li–X alloys. *Acta Materialia* 2014; 66:199.
- [115] Dorin T, De Geuser F, Lefebvre W, Sigli C, Deschamps A. Strengthening mechanisms of T_1 precipitates and their influence on the plasticity of an Al–Cu–Li alloy. *Materials Science and Engineering A* 2014; 605:119.
- [116] Dorin T, Deschamps A, De Geuser F, Sigli C. Quantification and modelling of the microstructure/strength relationship by tailoring the morphological parameters of the T_1 phase in an Al–Cu–Li alloy. *Acta Materialia* 2014; 75:134.
- [117] Kim N, Howe J, Boden E. *Journal de Physique Colloques*, 1987: 48 C3–457 – C3–463.
- [118] Starink MJ, Wang SC. The thermodynamics of and strengthening due to co–clusters: General theory and application to the case of Al–Cu–Mg alloys. *Acta Materialia* 2009; 57:2376.
- [119] Radmilovic V, Tolley A, Marquis EA, Rossell MD, Lee Z, Dahmen U. Monodisperse $Al_3(LiScZr)$ core/shell precipitates in Al alloys. *Scripta Materialia* 2008; 58:529–532.

- [120] Shercliff HR, Ashby MF. A process model for age hardening of aluminium alloys – II. Applications of the model. *Acta Metallurgica et Materialia* 1990; 38(10):1789.
- [121] Chinh NQ, Csikor F, Kovács Z, Lendvai J. Critical concentration of Mg addition for plastic instabilities in Al–Mg alloys. *Journal of Materials Research* 2000; 15(5): 1037.
- [122] Gerold V, Karnthaler HP. On the origin of planar slip in FCC alloys. *Acta Metallurgica* 1989; 37(8):2177.
- [123] Morris DG, Besag FMC, Smallman RE. Discontinuous yielding and dislocations locking in Cu₃Au *Acta Metallurgica* 1974; 22:801.
- [124] Cuniberti A, Niewczas M. Effect of temperature on superdislocation dissociation in Cu–Zn–Al 18R single crystals. *Scripta Materialia* 2001; 45:853.
- [125] Nix WD, Menezes RA. Physics of strengthening mechanisms in crystalline solids. *Annual Review of Materials Science* 1971; 1:313.
- [126] Alexopoulos ND, Migklis E, Stylianos A, Myriounis DP. Fatigue behaviour of the aeronautical Al–Li (2198) aluminium alloy under constant amplitude loading. *International Journal of Fatigue* 2013; 56:95.
- [127] Sun DL, Yang DZ, Lei TQ. A study of serrated plastic flow behaviour in an aluminium–lithium binary alloy. *Materials Chemistry and Physics* 1990; 25: 307.
- [128] Wert JA, Wycliffe PA. Correlation between S' precipitation and the portevin–Le Chaterlier effect in an Al–Li–Cu–Mg–Zr alloy. *Scripta Metallurgica* 1985; 19:463.
- [129] Kumar S, McShane HB. Serrated yielding in Al–Li alloys. *Scripta Metallurgica et Materialia* 1993; 28:1149.
- [130] Morris DG. APB relaxation at superdislocations in ordered alloys and anomalous strengthening. *Scripta Metallurgica et Materialia* 1992; 26:733.

Curriculum vitae

Surname	Ovri
First name	Henry
Date of birth	2 nd May, 1974
Place of birth	Benin city, Nigeria
09. 1980 – 07. 1986	Aileru Primary School, Warri, Nigeria
09. 1986 – 07. 1992	Dom Domingos College, Warri, Nigeria
01. 1993 – 08. 1999	Federal University of Technology, Owerri, Nigeria Degree: Bachelor of Engineering
07.2000 – 06.2001	National Youth Service Corp (NYSC), Federal University of Technology, Akure, Nigeria
08. 2001 – 09. 2004	Federal University of Technology, Akure, Nigeria Degree: Master of Engineering
04. 2004 – 08. 2008	Lecturer, Delta State Polytechnic, Ogwashi-Uku, Nigeria
09. 2009 – 08. 2010	University of Aveiro, Portugal; Technical University of Harburg – Hamburg, Germany; Aalborg University, Denmark (Consortium Universities) Degree: Master of Science
03. 2011 – 11.2015	PhD student, Helmholtz Zentrum Geesthacht, Germany

